HOLOGRAPHIC SCULPTING OF ELECTRON BEAMS WITH DIFFRACTION

GRATINGS

by

JORDAN SIDNEY PIERCE

A DISSERTATION

Presented to the Department of Physics
and the Graduate School of the University of Oregon
in partial fulfillment of the requirements
for the degree of
Doctor of Philosophy

September 2018

DISSERTATION APPROVAL PAGE

Student: Jordan Sidney Pierce

Title: Holographic Sculpting of Electron Beams with Diffraction Gratings

This dissertation has been accepted and approved in partial fulfillment of the requirements for the Doctor of Philosophy degree in the Department of Physics by:

Dr. Richard Taylor	Chair
Dr. Benjamin McMorran	Advisor
Dr. David McIntyre	Core Member
Dr. George Nazin	Institutional Representative

and

Janet Woodruff-Borden	Vice Provost and Dean of the Graduate School

Original approval signatures are on file with the University of Oregon Graduate School.

Degree awarded September 2018

DISSERTATION ABSTRACT

Jordan Sidney Pierce

Doctor of Philosopy

Department of Physics

September 2018

Title: Holographic Sculpting of Electron Beams with Diffraction Gratings

Electron microscopes offer scientists an invaluable tool in probing matter at a very small scale. Rapid advancements over the past several decades has allowed electron microscopes to routinely image samples at the atomic scale. These advancements have been in all aspects of electron microscope design – such as more stable control voltages and currents, brighter and more coherent sources, beam aberration correction, and direct electron detectors, to name a few. One very recent advancement is in shaping the electron beam to provide an almost arbitrary set of possible beam profiles.

Following the demonstration of electron vortex beams in 2010, there has been a surge of interest in the potential shaping electron beams. Utilizing holographic electron diffraction gratings, an almost arbitrary set of electron beams can be generated. These diffraction gratings are challenging to create due their tiny size and the precision with which they must be fabricated.

We present a comprehensive study on the fabrication and design of electron diffraction gratings with the aim of being able to produce optimal gratings that result in bright, well separated beams which closely match a desired beam profile. We have developed and optimized fabrication of these gratings with focused ion beam milling, and have been able to use the fabricated gratings in a number of important experiments.

These electron diffraction gratings have allowed us to perform various experiments such as aberration correction, electron helical dichroism, advanced phase-contrast imaging, and multi-beam interferometric techniques. Holographic beam shaping will continue to be an important tool for electron microscopists.

This dissertation includes previously published and unpublished co-authored material.

CURRICULUM VITAE

NAME OF AUTHOR: Jordan Sidney Pierce

GRADUATE AND UNDERGRADUATE SCHOOLS ATTENDED:
    University of Oregon, Eugene
    Humboldt State University, Arcata, California

DEGREES AWARDED:
    Doctor of Philosophy, Physics, 2018, University of Oregon
    Bachelor of Science in Physics, 2011, Humboldt State University
    Bachelor of Science in Environmental Engineering, 2008, Humboldt State University

AREAS OF SPECIAL INTEREST:
    Electron Beam Shaping
    Electron Diffraction Gratings
    Propagation Simulation

PROFESSIONAL EXPERIENCE:

    Graduate Research Assistant, University of Oregon, 2013-2018

    Graduate Teaching Fellow, University of Oregon, 2011-2013

GRANTS, AWARDS AND HONORS

    Poster Award, Microscopy and Microanalysis, 2014

    Qualifying Exam Prize, UO Department of Physics, 2012

    Meritorius Winner, Mathematical Contest in Modelling (MCM), 2008

PUBLICATIONS:

Tyler R. Harvey, **Jordan S. Pierce**, Amit K. Agrawal, Peter Ercius, Martin Linck, and Benjamin J. McMorran. Efficient diffractive phase optics for electrons. *New Journal of Physics*, 16(9):093039, September 2014.

Tyler R. Harvey, **Jordan S. Pierce**, Jordan J. Chess, and Benjamin J. McMorran. Demonstration of electron helical dichroism as a local probe of chirality. *arXiv*

1507.01810, July 2015.

Martin Linck, Peter A. Ercius, **Jordan S. Pierce**, and Benjamin J. McMorran. Aberration corrected STEM by means of diffraction gratings. *Ultramicroscopy*, 182:36–43, November 2017.

Colin Ophus, Jim Ciston, **Jordan Pierce**, Tyler R. Harvey, Jordan Chess, Benjamin J. McMorran, Cory Czarnik, Harald H. Rose, and Peter Ercius. Efficient linear phase contrast in scanning transmission electron microscopy with matched illumination and detector interferometry. *Nature Communications*, 7:10719, February 2016.

Fehmi S. Yasin, Tyler R. Harvey, Jordan J. Chess, **Jordan S. Pierce**, and Benjamin J. McMorran. Path-separated electron interferometry in a scanning transmission electron microscope. *Journal of Physics D: Applied Physics*, 51(20):205104, 2018.

ACKNOWLEDGMENTS

TABLE OF CONTENTS

LIST OF FIGURES

LIST OF TABLES

CHAPTER I

INTRODUCTION

Beams of light were shown to be able to carry orbital angular momentum (OAM) in 1992 [1]. Since then, many tools and applications have been developed to exploit the OAM of light. This allowed a number of interesting applications to be developed, such as increased optical bandwidth [2, 3], exoplanet detection [4], and even particle manipulation [5, 6]. In 2010 and 2011, electron beams carrying OAM were discovered independently by three groups [7, 8, 9]. Demonstrating electron beams carrying OAM was the start of a line of research into the design and application of shaped electron beams – those with OAM or other advanced phase and amplitude structures. In optics, research into the production and application of structured beams has been receiving much work since the 90's, while shaped electron beams have only recently been examined. The constraints on beam manipulation within an electron column makes electron beam shaping much more difficult both to accomplish and to study.

There have been several methods proposed for shaping electron beams, including phase plates [7, 10], magnetic nanowires [11, 12], electric nanorods [13, 14], aberration correctors [15, 16], and diffraction gratings [9, 17, 18, 19, 20, 21, 22]. Magnetic nanowires and electric nanorods produce beams with a spectrum of OAM states instead of a single state, and they don't offer a high degree of control for producing beams other than vortex beams. Phase plates are difficult to produce due to the exacting geometry needed, and no material has been found to be completely electron transparent, resulting in unwanted intensity loss through the phase plate. Electron diffraction gratings offer the greatest degree of control over the final shape of the beam, but suffer from producing multiple unwanted beams and having limited intensity.

There are many current and proposed uses for shaped electron beams, including but

not limited to vortex beams [23, 20, 24, 25, 11, 26], aberration correction [22], dichroism [23, 20, 26], and enhanced imaging [27]. Electron diffraction gratings are well suited for many of these applications, and while the theory follows closely with its counterpart in optics, there are many unique challenges and constraints in producing electron diffraction gratings to warrant much study into their design and fabrication.

Diffraction gratings are generally of two types – transmission gratings or reflection gratings. Transmission gratings work by modulating the phase and/or amplitude of the incident beam as it passes through the grating. These modulations are intended to produce separated beams. This process relies on the beam obeying the wave equation – specifically, the incident wave should be coherent over the diffraction grating. Clearly light obeys a wave equation, and due to the wave-particle duality of nature, all particles indeed satisfy a wave equation, though not necessarily the same wave equation as light.

To model how electrons are diffracted by a grating, we assume that the electrons are classical waves. This approximation is valid for low intensity beams – beams where the interaction of multiple electrons within the beam (due to their charge) can be neglected. Even with the advent of newer brighter sources, this approximation is still quite valid.

Chapter 2 gives an overview of electron diffraction gratings. In this chapter, I performed the majority of the experiments and gathered the majority of the data, and I also made most of the figures. Tyler Harvey helped with data analysis and provided Figure 2.5. Much of the content in this chapter comes from Harvey *et al.* [19]. Shaping electron beams with diffraction gratings is a new field of study beginning in 2011 with work on creating electron vortex beams. Much of the early work focused on creating binary amplitude gratings – where either the electron beam was blocked fully by the grating, or else allowed to pass though unhindered. These types of gratings are not ideal for several reasons, such as that they take a long time to mill, have a large pitch (and therefore small angular separation between beams), and do not provide a great deal of control over the shape of the diffracted

beams. We study the production and use of electron phase gratings. These gratings work my milling small grooves partially through a thin electron transparent membrane. Because of this, they can be made to have a much smaller pitch than amplitude gratings. We show a study on the efficiency of electron phase gratings made with focused ion beam (FIB) milling.

Chapter 3 provides a theoretical treatment of electron diffraction gratings under the thin hologram approximation. This work aims at being able to better understand the underlying mechanism of how the diffraction gratings operate in order to be able to produce a more exact diffracted beam. Being that electron diffraction gratings are effectively a method to modulate the phase and amplitude of a transmitted beam, what is the most desirable phase and amplitude modulation so as to make a specific output beam? Especially when considering the limitations of the fabrication techniques, it becomes much more important to have a model that can take this into account.

Chapter 4 provides and outline of the fabrication techniques that our group has studied for making electron diffraction gratings. We have primarily focused on FIB milling, but we have also looked at other methods such as E-Beam lithography. We present techniques that help to maximize the production quality of diffraction gratings within a FIB, as well as preparatory methods for ensuring high quality gratings.

Chapter 5 gives an overview of several applications for electron diffraction gratings. This includes previously published and unpublished work that I have been part of. For all of these experiments I provided the technical expertise to design and develop the electron diffraction gratings, as well as help to form the experiments. I also provided help with the analysis and write-up of the data. I also performed that experiment with the highly twisted electron beams. This chapter provides a small glimpse into the possible applications of diffraction gratings, with much more work still being done.

Chapter 6 is a theoretical exploration on the possible use of lasers to shape atom beams (I look at atom beams because they interact more strongly with lasers). With intense

enough lasers it might be possible to use a similar concept to shape electron beams. This is preliminary work, but I show that there is a strong possibility that this can indeed make acceptable beams.

CHAPTER II

OVERVIEW OF ELECTRON DIFFRACTION GRATINGS

This chapter follows closely with work that I previously coauthored with Tyler Harvey, published as Harvey *et al.*, *New J. Phys.* **16** 093039 (2014) [19]. I made all of the diffraction gratings used for this paper and performed most of the measurements, including the atomic force microscope (AFM) surface topology scans, the diffraction efficiency tests, and the measurement of the Gaussian fit parameters. Tyler Harvey performed much of the analysis and wrote most of the manuscript.

Using diffraction gratings to shape electron beams is possible because of the wave-particle duality that exists in nature. Electrons are charged massive particles, yet they still fundamentally obey a wave equation very similar to the wave equation for electromagnetic fields. Due to the fact that electrons are both charged and massive, there are some critical differences in how electrons interact with diffraction gratings versus photons, but these differences can typically be neglected.

For instance, multiple electrons in a beam-line can interact with each other, causing decoherence and energy spread, and electrons can interact with induced phonons within the diffracting material. However, even with modern Schottky emitters and high beam currents (compared to previous generation emitters), the beam current is still small enough that the electron-electron interaction within the beam can usually be neglected. The surface charge interactions induced by the proximity of the electrons to the diffracting material can have a small but significant effect on the diffracted beams, depending on the geometry and material used. For thin phase gratings milled on silicon nitride (Si_3N_4), the effect of the surface charge is very small and we will not discuss it in detail here.

Because we can often ignore the effects of surface charge, the same principals that exist within scalar diffraction theory for EM fields transfer quite well to electrons. However, there

is a much higher degree of constraint within an electron beam column due to the high vacuum necessary, and because electrons interact strongly with materials. These constraints lead to many differences in how electron diffraction gratings are designed and produced compared to diffraction gratings for optical systems.

2.1   Electrons as Waves

This section will give a basic overview of how electron diffraction works, specifically within a Transmission Electron Microscope (TEM).

The effectiveness of scanning transmission electron microscopy (STEM) has given scientist an invaluable tool for understanding and probing many properties of atomic scale materials [28, 29]. Much effort has been given to improving the design and control of the electromagnetic lenses and control systems. These improvements allow modern STEM instruments to achieve Ångstrom sized probes from between 60 to 300 keV with nanoamperes of current [30, 31]. Probes focused in traditional STEM setups have a Gaussian like intensity profile with an ideally flat phase profile. The aberrations induced by the optical setup are well characterized and understood.

As increasing the resolution of STEM imaging yields less benefit (since a STEM probe can already be sub Ångstrom in size), there has been an increase in the development of STEM probes with non Gaussian profiles. These shaped probes offer new venues of measurement and detection that is not possible with traditional beams [16, 32, 33]. The first forays into shaped electron beams looked at the potential of electron vortex beams [7, 8, 34]

Electrons are characterized by their intrinsic properties – their charge and rest mass, which are identical for every electron. Electrons can also carry various extrinsic properties, such as Orbital Angular Momentum (OAM) and wavelength (called the de Broglie wavelength for the wavelength of massive particles). The de Broglie wavelength λ of a massive

particle is

$$\lambda = \frac{h}{p} \tag{2.1}$$

where p is the momentum of the particle and h is the Planck constant.

Electron energy within electron microscopes can vary widely, from less than 1 keV for highly surface-sensitive SEMs to more that 10^3 keV for the most powerful TEMs. Typical beam energies in a TEM are from 80 keV to 300 keV, corresponding to wavelengths from 4.18 picometers to 1.97 picometers, respectively. It is precisely this tiny wavelength that allows electrons to be useful for extremely high resolution imaging; however, this small wavelength also means that any periodically generated diffraction grating will produce beams that have only a very slight diffraction angle.

2.2 Electron Diffraction

Electron diffraction gratings can accurately generate a wide range of beam profiles with structured phase and amplitude. Typically, a traditional STEM is retrofitted with the desired diffraction grating in the beam-limiting aperture, allowing for one of the diffracted probes to be focused onto a sample, as shown in Figure 2.1. Often a diffraction grating is employed to create a single beam, which is taken to be the first diffraction order. Unless otherwise stated, we assume that a diffraction grating is utilized to create a single beam mode in the first diffraction order, and all other diffracted beams are unwanted.

Electron diffraction gratings are fabricated by milling into Si_3N_4 membranes. The resulting milled membrane can be mathematically described as $t(\vec{r})$, the mill depth at point $\vec{r}$. The general method by which to define $t(\vec{r})$ for diffraction gratings is via interference of a desired beam $\Psi(\vec{r})$ (assumed to be propagating in the positive z direction) with a reference beam $\Psi_R(\vec{r})$, which is used to define the hologram pattern [35]

$$t(\vec{r}) = |\Psi_R(\vec{r}) + \Psi(\vec{r})| . \tag{2.2}$$

Typically, the reference wave is often taken to be something simple, such as a plane-wave or spherical wave. If the reference wave is a plane wave that is not propagating solely in the z-direction, the resulting diffraction pattern is termed an "off-axis grating", and the diffracted beams all have different beamlines. If the reference wave is a spherical wave with a source on the z-axis, the resulting diffraction grating is called an "on-axis grating", which has diffracted beams all with the same beamline but separated by the point in which they come to focus.

One often-studied beam type is a vortex beam – these beams have a non-zero azimuthal winding number m which defines a phase term $e^{im\phi}$, where ϕ is the azimuth about the optical axis. Each ray of constant ϕ from the beam axis has a constant phase, but this phase is different for different ϕ values – because of this, the phase on the optical axis is not defined, and is described as a singularity in the wave-function. These beams are called vortex beams because the surface of constant phase forms a corkscrew like spiral. This phase vortex correlates to a beam carrying orbital angular momentum (OAM) about the beam axis.

To produce a grating which encodes an electron vortex beam with $m\hbar$ of orbital angular momentum separated from the zeroth-order beam by momentum k with a reference plane-wave,

$$t(\vec{r}) = A \left| e^{im\phi} + e^{i\vec{k}\cdot\vec{r}} \right| = A \left(1 + \cos\left(m\phi + \vec{k}\cdot\vec{r} \right) \right). \tag{2.3}$$

Note here that the angular separation of the beams, given by k, is determined from the reference wave. The maximum depth of the grating, given by A, determines the total intensity in the diffracted orders. Here $\vec{r}$ is the radial vector in they x-y plane, and has no component in the z direction.

There are other methods that can be utilized to create electron vortex beams, such as phase plates [7] and magnetic nanowires [36, 12]. However, these methods lack the precise control of the phase structure of the generated beam and are highly sensitive to mill defects and voltage fluctuations. Electron diffraction gratings always produce multiple beams –

8

this can be useful for experiments which require more than one electron beam, such as with dichroism [37] and interferometry [38]. However, often the extra beams produced are unwanted and must either be ignored or removed at an intermediate stage before interaction with a sample.
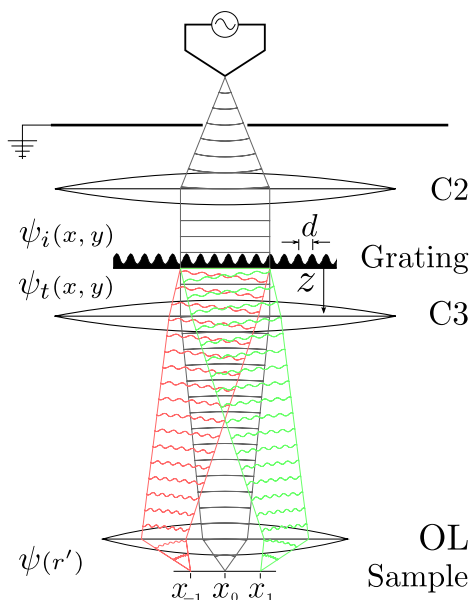
FIGURE 2.1: Basic schematic of off-axis diffraction within a TEM. Typically, the diffraction grating is placed in the beam-forming aperture, allowing one or more of the diffracted beams to be focused onto a sample. We use an FEI image-corrected Titan, which has a beam-forming aperture in the second condenser lens system, called the C2 aperture. Various methods are available to pre-select and post-select relevant beams. Reprinted with permission from [19].

In general, there are three main points of consideration when designing an electron diffraction grating: beam separation, beam intensity, and beam fidelity. The beams must be sufficiently separated such that unwanted beams can be either blocked or ignored – this typically means that diffraction grating groove spacing should be on the order of 100 nm. The beam intensity relative to the incident beam is related to the membrane thickness and the geometry of the diffracted beam. Lastly, the fidelity of the generated beams must be sufficient to be useful in the detection strategy desired. For example, several early methods

used to produce electron vortex beams consisted of milling wholly through an electron opaque membrane [8, 39, 40]. These methods do not produce widely separated beams, are limited to about 10% intensity of the incident beam into the first diffracted order, and do not produce a pure mode beam.

To generate more useful diffraction gratings, our group has put much work into the development and understanding of transparent electron phase gratings [41], an example of which is shown in Figure 2.2. These gratings are termed *phase* gratings because the primary action is to modulate the phase of the transmitted beam. In reality, no material is completely electron transparent, thus there will be some amplitude modulation associated with the diffraction gratings. Because of this, the gratings are technically *complex* type diffraction gratings. However, in the literature the term *phase* grating is ubiquitous for this type of grating, thus we will use the term phase grating throughout this manuscript.

2.3   Diffraction Efficiency

The efficiency of a diffraction grating can be defined in various ways, depending on the most important parameter of the resulting diffracted probes. Diffraction gratings are characterized by several parameters, notably the depth and groove position. If the overall depth is low, this imprints only a very slight phase modulation on the transmitted electron wave, correlating to less intensity in the diffracted beams than desired. If the groove positions are milled wrong, this correlates to a structurally deficient probe. Both of these correlate to how efficiently a diffraction grating can produce a desired beam. However, the latter cannot be quantified with a single parameter. Because of this, we reserve the term *diffraction efficiency* to represent a measure of the intensity of the desired beam to the other beams. Even with this, there are still several methods by for which to measure the diffraction efficiency. Absolute diffraction efficiency $\eta_n^{(I)}$, transmitted diffraction efficiency $\eta_n^{(T)}$, and relative diffraction efficiency $\eta_n^{n'}$ characterize the current in the nth diffracted beam relative
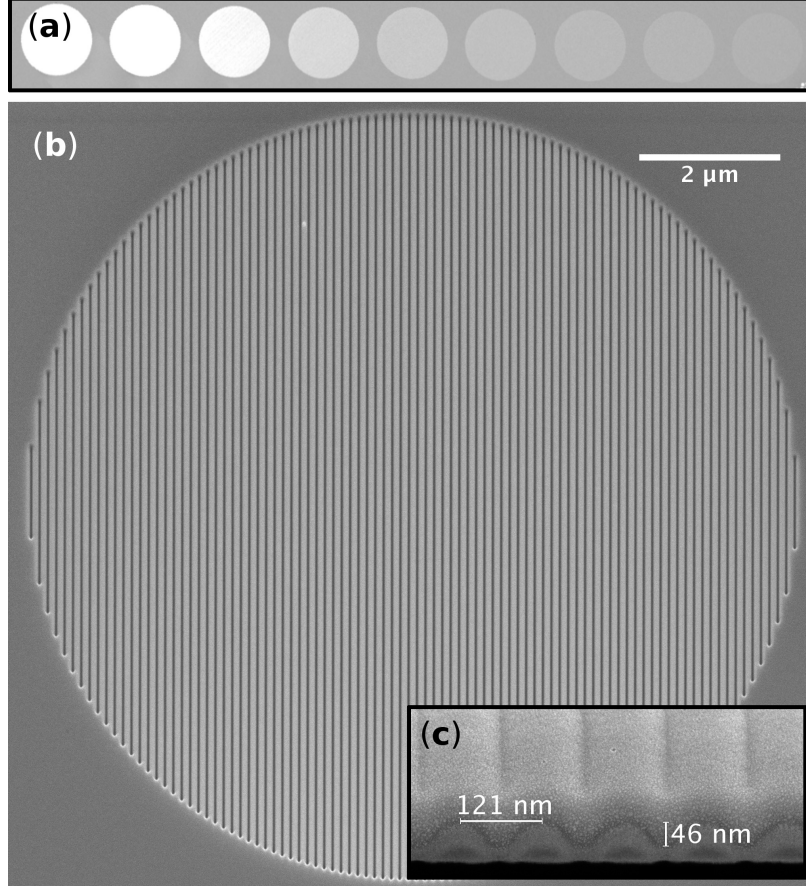
FIGURE 2.2: Uniform electron diffraction grating milled into Si_3N_4. Unstructured gratings such as that shown in (b) were used to measure the efficiency of electron diffraction gratings milled into Si_3N_4. Many gratings of the same shape were milled to differing depths (a) to generate efficiency curves. The grating shown in (b) is 10 μm in diameter with 120 nm pitch. (c) Perspective view of a FIB cross-section of a diffraction grating shows the sinusoidal shape of the milled Si_3N_4. For this FIB cross-section, approximately 50 nm of Platinum was deposited on the grating before cross-sectioning to provide a clean cross-section. Reprinted with permission from [19].

to the incident beam, the current in the nth beam relative to the total transmitted intensity, and the current in the nth beam relative to the n'^{th} beam, respectively. These are more precisely defined as

$$\eta_n^{(I)} = \frac{I_n}{I_I} \qquad\qquad \eta_n^{(T)} = \frac{I_n}{\sum I_n} \qquad\qquad \eta_n^{n'} = \frac{I_n}{I_{n'}} \qquad (2.4)$$

where I_n is the current in the nth diffracted beam, and I_I is the intensity of the incident beam.

For many applications the desired measure of efficiency is either $\eta_{+1}^{(I)}$ or η_{+1}^0. For binary amplitude gratings, the maximum incident beam current that can be diffracted into the first diffraction order, $\eta_{+1}^{(I)}$, is only 10.1%; whereas sinusoidal phase gratings can easily surpass this with a maximum absolute efficiency of above 30%. Phase gratings also allow for the potential of creating blazed gratings, which can increase η_{+1}^0 at the expense of η_{-1}^0.

It is worth noting that because no material is completely electron transparent, as stated above, the transmitted intensity of a diffraction grating is necessarily less than the incident intensity, $\sum I_n < I_I$. Because the degree to which the transmitted intensity is reduced depends on the mill depth of the grating, its groove shape, and the membrane thickness, it is convenient to use $\eta_n^{(T)}$ when speaking of the diffraction efficiency of a particular grating. Thus, unless otherwise stated, diffraction efficiency refers to $\eta_{+1}^{(T)}$.

These differences in how efficiency is reported can be easily overlooked. For instance, Grillo *et al* reported a 25% efficiency for the first order beam [18], but failed to specify the type of efficiency, which was the *transmitted* efficiency. Taking into account the thickness of the Si_3N_4 upon which their grating was fabricated, we calculate that the absolute diffraction efficiency is closer to 5%, since 120 nm of Si_3N_4 blocks roughly 80% of the beam.

2.4   Diffracted Beam Separation

The primary function of an electron diffraction grating is to create a desired beam well separated from any other beams. This is achieved by providing the diffracted beams with a lateral momentum that separates the beams from each other. While it is possible for large diffraction angles to be a problem because they move away from the optical center of the column, in general the diffraction grating should be produced with as small of pitch as possible.

For electrons with de Broglie wavelength λ passing through a diffraction grating with pitch d (with $\lambda \ll d$), the angular separation $\Delta\Theta$ between adjacent diffracted beams is

$$\Delta\Theta = \frac{\lambda}{d}. \tag{2.5}$$

For gratings placed above the specimen plane in an electron microscope, this corresponds to a physical separation Δx between diffracted probes of

$$\Delta x = \frac{z}{M}\Delta\Theta = \frac{z\lambda}{Md} = L\frac{\lambda}{d}, \tag{2.6}$$

where M is the magnification of the probe-forming optics (specifically, M is *not* the magnification of the image), z is the physical distance from the diffraction grating to the specimen, and L is the effective camera length of the probe-forming optics.

Our lab has use of the TEAM 1 instrument at the National Center for Electron Microscopy (NCEM). For this instrument, a grating with a pitch of $d = 83$ nm in the C2 aperture under 300 keV illumination produces a probe separation of $\Delta x = 43$ nm under standard STEM parameters. While this is quite a small separation, it is just a sufficient distance for isolating individual structured STEM probes for microscopic experiments.

Electron phase gratings can much more easily produce highly separated beams when compared to amplitude holograms for several reasons. Amplitude holograms must be thick enough to block a significant portion of the incident beam while not being so thick that they can't be milled through, and the feature size must be large enough for the unsupported portions to have the required rigidity to not deform. Because of this, typical amplitude gratings have a pitch on the order of a micron [8, 39, 40], while phase gratings have been made with features as small as 20 nm [42].

2.5 Basic Diffraction Model

The goal of measuring the diffraction efficiencies of various gratings is to be able to model and understand the diffraction process within an electron microscope, with the ultimate goal

of being able to design and produce optimal gratings. To do this, it is necessary to have an accurate model of how diffraction gratings work within a microscope. High-resolution atomic force microscope (AFM) scans were made of many gratings of the type shown in Figure 2.2, which are termed flat phase gratings because each groove is ideally perfectly straight (the phase structure of the resulting beams is flat). The data for each grating was then processed to determine the average groove shape and groove depth, such as shown in Figure 2.3.
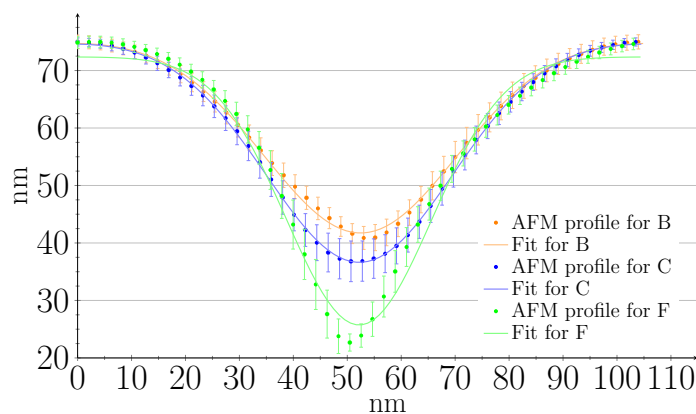
FIGURE 2.3: AFM profiles of several diffraction gratings milled into Si_3N_4 membranes of 75 nm thickness. Each diffraction grating was milled to have 100 nm pitch but differing depths. For each grating, a best-fit Gaussian curve is provided for reference. For detailed information on the numbering of the profiles, see [19]. Reprinted with permission from [?].

With a thickness profile $T(\vec{r})$ for each grating, we employed the thin hologram approximation as our model. The thin hologram approximation is valid in the regime where the effects of diffraction within the thickness of the grating are negligible. This depends on the wavelength of the beam, the pitch of the grating, and the depth of the grating grooves. However, because of the very small diffraction angles and the small depth of the milled gratings (typically 30 nm or less), the approximation is quite valid for our purposes.

With this assumption, the transfer function $\mathcal{T}(\vec{r})$, which describes the effect on the

amplitude and phase of a beam transferring through the diffraction grating, is given by

$$T(\vec{r}) = e^{i\widetilde{V}T(\vec{r})}, \tag{2.7}$$

where $\widetilde{V} = CV_0 + i\gamma$ is effectively the complex index of refraction for the material. Here V_0 is the mean-inner-potential of the grating material, γ gives the loss of intensity due to both inelastic and high energy scattering within the material, and C is a parameter depending only on the accelerating voltage of the beam V_a [43] given by

$$C = \frac{2\pi}{\lambda V_a} \frac{eV_a + m_e c^2}{eV_a + 2m_e c^2}. \tag{2.8}$$

Because the transfer function is independent of the incident wave function $\psi_i(\vec{r})$, the transmitted wave-function $\psi_t(\vec{r})$ becomes

$$\psi_t(\vec{r}) = \psi_i(\vec{r})T(\vec{r}) = \psi_i(\vec{r})e^{i\widetilde{V}T(\vec{r})}. \tag{2.9}$$

With this, we can simulate the effect of focusing the generated probes onto a sample utilizing the Fourier transform. For most purposes the incident beam is assumed to be a plane-wave, and is thus ignored. Analysis of the diffraction gratings then becomes analysis of the transfer function.

2.6 Diffraction Grating Material

There are a number of materials that can be utilized to make diffraction gratings, but we have exclusively utilized Si_3N_4 for a number of reasons. Firstly, from a material perspective, it is mostly ideal – it is amorphous, thus negating crystalline Bragg diffraction, and it is very tough and does not get easily damaged. Most importantly however is its ubiquity within TEM circles – it is a standard material used to prepare various samples for imaging within a TEM.

We have used silicon nitride membranes as thin as 15 nm and as thick as 500 nm, with the membrane freely suspended over areas from 50 μm × 50 μm up to 2 mm × 2 mm.

Low-stress silicon nitride with ideal chemistry of Si_3N_4 purchased from SPI Supplies, Inc. performed the best for our studies, both in stability and how planar the membranes are.

We concluded that, in general, membranes should be a minimum of 30 nm thicker than the desired maximum depth of the diffraction grating. This is probably due to the Gallium implantation that penetrates tens of nanometers into the material and weakens it. This implantation can be seen in Figure 2.2(c).

2.7 Optimization of Diffraction Efficiency

We performed a study measuring the shape and efficiency of various diffraction gratings. These were milled using a standard grating template 10 μm in diameter with 100 nm pitch. The depth was controlled by milling the standard template a number of times over the same area, each time increasing the depth of the mill. This procedure is called a dose-array. Diffracted beams from one such dose-array is shown in Figure 2.4

Measuring the profile and efficiency of many diffraction gratings allows us to explore the parameter space of diffraction efficiency vs groove profile and depth. For this study, we modeled each grating as a series of closely spaced Gaussian trenches – each characterized by the full width at half max w of the Gaussian fit, as shown in Figure 2.3. A figure summarizing both experimentally measured and theoretically predicted diffraction efficiencies as a function of grating characteristics is shown in Figure 2.5. The model does not line up terribly well with the data, as shown more clearly in Figure 2.6. The discrepancy of the model to the data can be attributed to a number of aspects, the most prominent of which are that the groove shapes are not terribly well approximated by a simple Gaussian, that Gallium implantation can effect the diffraction pattern while being invisible to AFM, and that the other side of the membrane (which is usually assumed to be unaffected by the milling) can have slight changes which effect the diffraction pattern. Nonetheless, the simple model is sufficiently accurate as to allow us to optimize the several physical grating characteristics
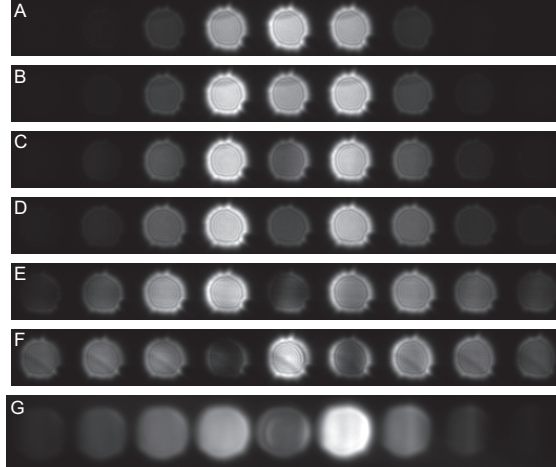
FIGURE 2.4: TEM diffraction images of several gratings from a dose array. Each grating is ideally identical in groove shape, but differing in the depth of the groove. The groove shape for gratings B, C, and F are given in Figure 2.3 showing that they have similar but not identical groove profiles. Gratings A-F are milled successively deeper into the membrane. Grating G was produced from a separate dose array but is included here because of its asymmetric diffraction pattern, which was caused by stage drift resulting in a slightly blazed profile. Reprinted with permission from [19].

necessary to maximize the current diffracted into a desired beam, such as the maximum mill depth and the grating profile.

2.8   Apodized Diffraction Gratings

There are multiple advantages to using phase gratings as opposed to binary gratings, such as having a smaller minimum pitch, having higher maximum efficiency, and having the potential for various groove profiles. In particular, however, phase gratings can be apodized – that is, they can have spatially dependent diffraction efficiency by changing the mill depth or the groove profile. This allows for diffraction gratings to more accurately recreate a desired beam, which is a critically important issue in many applications. Apodization in particular refers to varying the mill depth according to the envelope function $Z(\vec{r})$ of the desired beam.

17
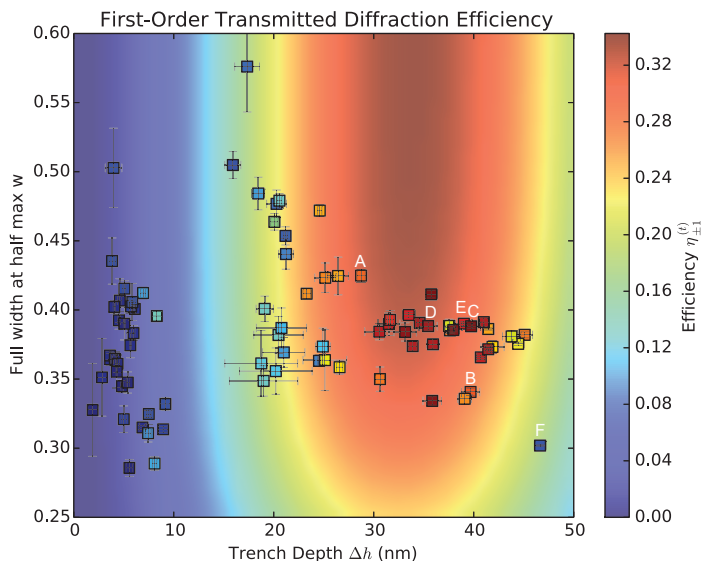
FIGURE 2.5: Parameter space giving the predicted efficiency (background color) and measured efficiency (squares) of many diffraction gratings. The efficiency shown here is the efficiency of the first order beam relative to the total transmitted intensity. The material is Si_3N_4 with various amounts of Gallium implanted due to the FIB milling process. Each square data point represents a single diffraction grating. The position of each grating was determined using AFM scans of the milled surface of the grating, while the efficiency of each grating was measured via TEM diffraction. The labeled points correspond to the respective gratings shown in Figure 2.4. The model used to generate the background map assumes symmetric grooves given by a repeating Gaussian profile. Reprinted with permission from [19].

Gratings such as those in Figure 2.2 have an abrupt edge to the milled grating. This introduces unwanted frequencies into the diffracted beam such that at focus, the probe is an Airy disk [44]. Ideally an unshaped diffracted probe would be Gaussian in profile, as an Airy disk has only about 84% of the power within the first radial node [45]. Over the past several years a number of techniques have been developed to control the wavefront of an electron beam, such as phase masks [46] and diffraction gratings [47, 18, 9]. However, these studies fail to reliably control both the phase and the amplitude of the diffracted beam. Here we show a basic method that can be employed to achieve much better reproduction of desired
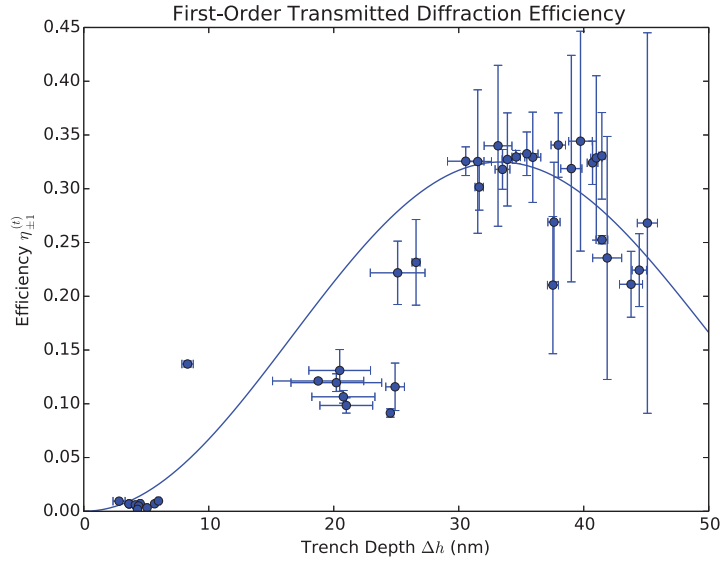
FIGURE 2.6: Diffraction efficiency of various diffraction gratings. This correlates to those gratings in Figure 2.5 which lie within $w = 0.375 \pm 0.025$. The solid line is a model assuming Gaussian-shaped groove profiles. Reprinted with permission from [19].

beam profiles.

By spatially varying the depth of the milled diffraction grating in accordance with the envelope function $Z(\vec{r})$ of the desired beam, one can achieve much better beam reproduction. Figure 2.7 shows the difference from a flat diffraction grating and an apodized grating, where the cross-sectional comparison of the focused probes are shown in Figure 2.9. The cross sectional comparison shows that indeed the apodized grating does have a closer to ideal amplitude profile than the flat grating.

The images of the diffracted beams were taken with the gratings in the sample plane using the Low-Angle-Diffraction (LAD) mode of our Titan TEM at 300 keV. This is a significantly different optical setup than when the grating is in the probe-forming aperture to use in STEM mode. Because of this, there are generally much higher aberrations in the images taken under LAD mode than would be present when the gratings are forming STEM
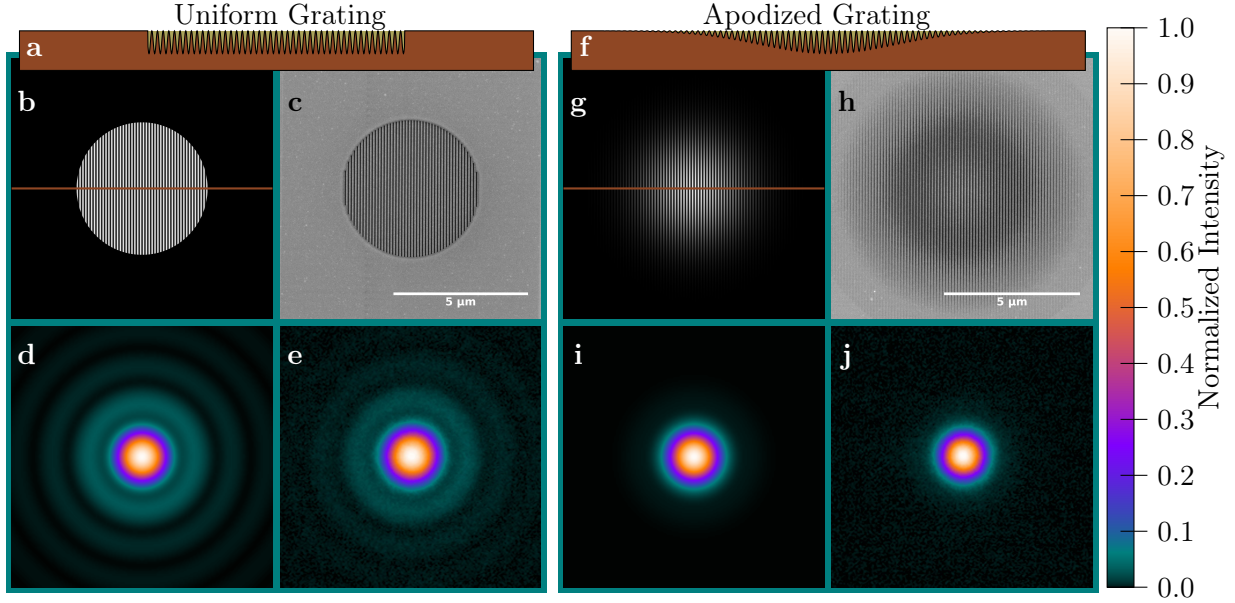
FIGURE 2.7: Comparison of uniform (left) vs. apodized (right) gratings. The upper inset on each row ((a) and (f)) gives the idealized cross-section through the center of the respective gratings (shown as the brown line through (b) and (g)). Idealized gratings are given in (b) and (g), with (c) and (h) the SEM images of the milled gratings. Images (d) and (i) give the simulated 1st order probes near focus generated by the holograms (c) and (h), respectively. The actual probes from these holograms are shown in (e) and (j). Note the lack of ringing in the apodized grating (j). Each image has been individually normalized. The quality of the probe from the apodized grating (j) is dependent on the maximum milled depth of the grating (g) – this grating had a maximum depth of approximately 20 nm, or approximately 0.6π radians phase depth. The quality of the probe from the uniform grating is unaffected by the grating depth, which only affects the intensity of the probe.

probes. These aberrations are proportional to the size of the grating, and the gratings used in this experiment were small (five to ten microns in diameter), resulting in images of the diffracted probes that have minimal aberrations.

We also ran this experiment for a forked hologram, generating beams with one unit of Orbital-Angular-Momentum (OAM) as seen in Figure 2.8. Typically, the more complicated the amplitude and phase profile of the desired beam, the less accurately the beam can be approximated either by a flat grating or a standard apodized grating. In this case, with a

20

single fork, the radial profiles comparing the flat vs. apodized gratings (Figure 2.10) shows that while the apodized grating does have smaller tails, it nonetheless does not conform to as well to the desired beam as for the case of the Gaussian in Figure 2.9, especially close to $\vec{r} = 0$.
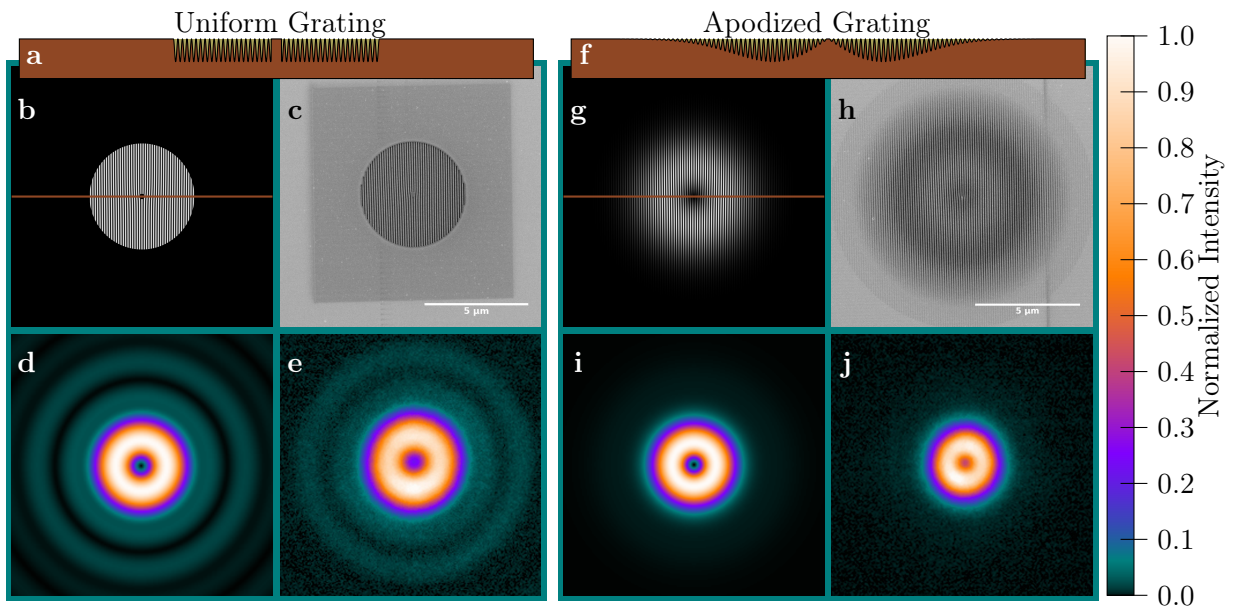
FIGURE 2.8: Comparison of uniform (left) vs. apodized (right) 1 OAM gratings. The upper inset on each row ((a) and (f)) gives the idealized cross-section through the center of the respective gratings (shown as the brown line through (b) and (g)). Idealized gratings are given in (b) and (g), with (c) and (h) the SEM images of the milled gratings. Images (d) and (i) give the simulated 1st order probes near focus generated by the holograms (c) and (h), respectively. The actual probes from these holograms are shown in (e) and (j). Note the lack of ringing in the probe from the apodized grating (j). Each image has been individually normalized. The quality of the probe from the apodized grating (j) is dependent on the maximum milled depth of the grating (g) – this grating had a maximum depth of approximately 20 nm, or approximately 0.6π radians phase depth.

To understand how this works as an approximation, we begin with the thin hologram approximation. Assuming plane wave illumination, the hologram is defined as given in

21
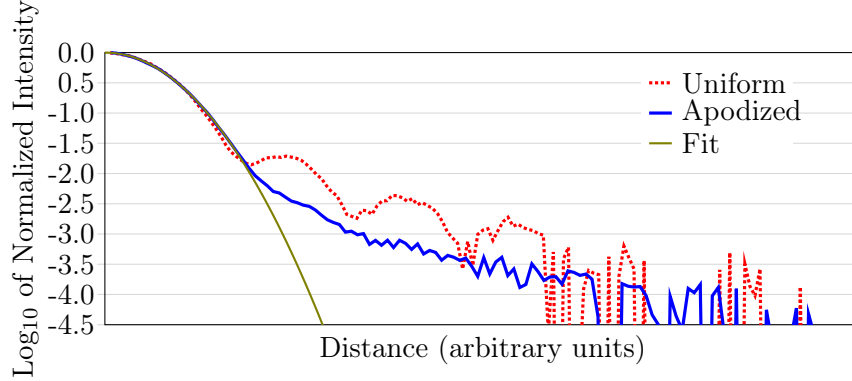
FIGURE 2.9: Azimuthally averaged radial profile plots of the intensity plots shown in Figure 2.7. The fit for the data was generated by fitting a Gaussian function to the raw intensity profile, which becomes a parabola in a log-plot. The data have been stretched such that the same Gaussian fit is the best fit for both sets.
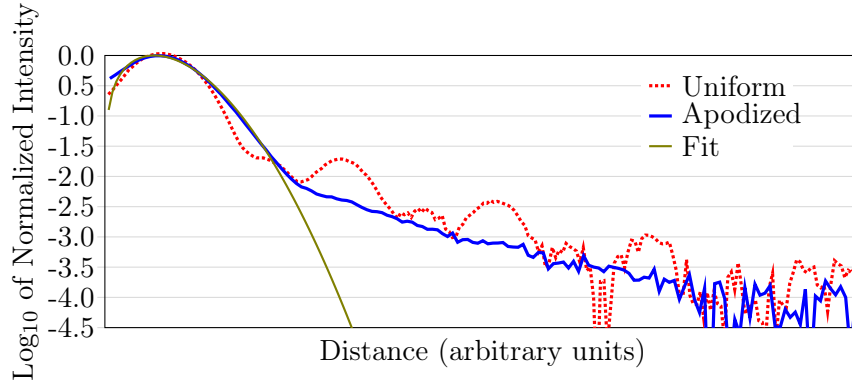
FIGURE 2.10: Azimuthally averaged radial profile plots of the 1-OAM beams shown in Figure 2.8. The fit for the data was generated by fitting a Laguerre Gaussian function to the raw intensity profile, then plotting the log of the data. The data have been stretched such that the same fit is the best fit for both sets.

Equation 2.2, the wave function just after interaction with the grating is

$$\psi(\vec{r}) = \exp\Big(i\widetilde{V}\left(d - h||\Psi_R(\vec{r}) + \Psi(\vec{r})||\right)\Big), \tag{2.10}$$

where d is the thickness of the membrane, h is the mill depth of the grating, and $||\cdot||$ represents the normed absolute-value (that is, it is the absolute value divided by the maximum value). This is simply the thin hologram transfer function with $\widetilde{V}$ the material parameters

22

and $d - h||\Psi_R(\vec{r}) + \Psi(\vec{r})||$ the thickness profile of the membrane. Note that d and h are both constant. Assuming h to be small, we can expand the exponential about $h = 0$, and drop the high order components. Assuming the reference wave to be a plane wave $\Psi_R(\vec{r}) = e^{ikx}$, this leaves

$$\psi(\vec{r}) \approx e^{i\widetilde{V}d}\left(1 - i\widetilde{V}h(\Psi_R(\vec{r}) + \Psi(\vec{r}))(\Psi_R^*(\vec{r}) + \Psi^{/}(\vec{r}))\right) \tag{2.11}$$

$$= e^{i\widetilde{V}d}\left(1 - i\widetilde{V}h(e^{ikx} + \Psi(\vec{r}))(e^{-ikx} + \Psi^*(\vec{r}))\right) \tag{2.12}$$

$$= e^{i\widetilde{V}d}\left(1 - i\widetilde{V}h\left(1 + e^{ikx}\Psi(\vec{r}) + e^{-ikx}\Psi^*(\vec{r}) + |\Psi(\vec{r})|^2\right)\right). \tag{2.13}$$

This is a set three beams, a modified copy of the incident beam plus a +1 beam proportional to e^{ikx} and a -1 beam proportional to e^{-ikx}. The first order is simply the desired beam $\Psi(\vec{r})$ with an added amount of linear momentum.

It is clear that, for small mill depths, apodized gratings can accurately generate beams. The apodized gratings shown in Figure 2.7 and Figure 2.8 were milled to a depth of about 20 nm, a little under half of the maximum invertible depth (see Section 3.4) of 41.34 nm (for $\widetilde{V} = \pi/(33 \text{ nm})(0.08i - 1)$ with 300 keV electrons).

2.9   Typical Diffracted Beams

Much of the work in electron beam shaping falls into one of two purposes – to produce an idealized, aberration-corrected beam for electron microscopy or lithography or to produce some sort of special beam mode, such as a vortex beam. For generating beam modes, much of the published literature focuses on either creating various Laguerre Gaussian beams [18, 48, 19, 9, 49] or creating Bessel Beams [50, 51]. Laguerre Gaussian beams are given by [52]

$$LG_p^m(r, \phi, z) = \left(\frac{2p!}{\pi(p + |m|)!}\right)\frac{1}{w(z)}\left(\frac{\sqrt{2}r}{w(z)}\right)^{|m|}\exp\left(-\frac{r^2}{w(z)^2}\right)L_p^{|m|}\left(\frac{2r^2}{w(z)^2}\right) \times$$
$$\exp\left(-ik\frac{r^2}{2R(z)}\right)e^{-im\phi}e^{-ikz}e^{i\psi(z)}. \tag{2.14}$$

23

Where L_p^m is the generalized Laguerre polynomial of degree p, w is the waist parameter of the beam, R is the radius of curvature of the beam, and $\psi(z)$ is the Gouy phase, given by

$$\psi(z) = (|m| + 2p + 1)\tan^{-1}\left(\frac{\lambda z}{\pi w_0^2}\right). \tag{2.15}$$

For many applications, it is the novel phase vortex term $e^{im\phi}$ that is of interest, which is why many groups work with non-apodized forked diffraction gratings, the fork being the result of combining a reference wave $e^{i\vec{k}\cdot\vec{r}}$ with a phase vortex. An example of what a typical Laguerre beam, $LG_0^1(\vec{r})$, looks like is sown in Figure 2.11, which also shows a non-apodized hologram.
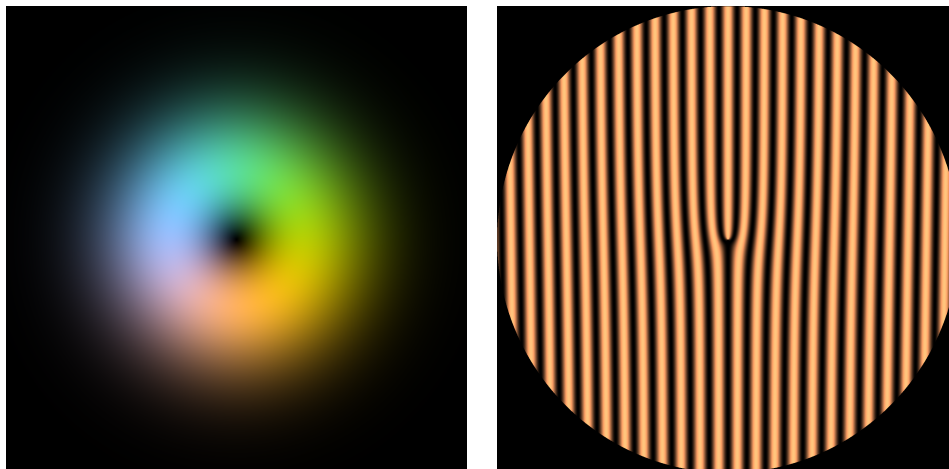
FIGURE 2.11: An example of a vortex beam given via $LG_0^1(\vec{r})$ (left), and a typical fork hologram used to generate an approximate vortex beam (right). The central feature of the vortex beam is the phase structure of the beam – that the phase changes by 2π about the azimuth, which is encoded as the fork in the hologram.

Bessel beams are solutions to the full wave equation and not limited to the paraxial approximation. Like plane-waves, they are not normalizable and can never be created. However, Bessel beams are often a good model for various purposes. Bessel beams are defined as

$$B_m^k(r, \phi, z) = A_0 J_{|m|}(k_r r)e^{im\phi}e^{ik_z z}, \tag{2.16}$$

24

where J_m is an mth order Bessel function, k_r and k_z are the radial and longitudinal wave vectors with $k = \sqrt{k_r^2 + k_z^2}$, and A_0 is the complex amplitude. As with plane-waves, Bessel beams are non-diffracting and technically have infinite energy.

2.10 Representation of Complex Amplitude

Any wave, whether acoustical, optical, or matter, has a spatially dependent amplitude and phase distribution. It is typical in literature to represent amplitude and phase distributions as a color image, where the color represents the phase and the brightness represents the amplitude. This is almost universally done using the hue-saturation-value (HSV) color map [53, 54, 55, 56]. However, HSV color maps provides a very poor representation of the complex amplitude because of the non-constant luminance [57] of the transformation.

Luminance is a measure of the perceived brightness of a light source. This perceived brightness depends on the intensity and spectral distribution of the light. The red, green, and blue receptors in our eyes are not ideal, and their response to intensity and frequency is complex and non-linear. Because of the complicated manner by which we perceive light, the International Commission on Illumination – abbreviated CIE for its French name "Commission internationale de l'éclairage" – was established in 1913 to develop an international standard on the representation of color and other related topics. Of importance here is the publication of the CIELAB color space in 1976. The CIELAB color space has three parameters 'L' for lightness and 'A' and 'B' for the red-green and yellow-blue components. As with other color spaces such as HSV, this is a three component space. CIELAB was specifically developed such that values of constant lightness have a perceptually uniform intensity with respect to normal human color vision. This makes CIELAB a particularly useful color space in applications involving color acceptability decision making [58]. Utilizing this color space, representations the complex amplitude of beams can be much more quantitative, as shown in Figure 2.12. Throughout this document we use a color map with perceptually uniform

25

luminance. Code for generating images with this color map is given in Appendix B.
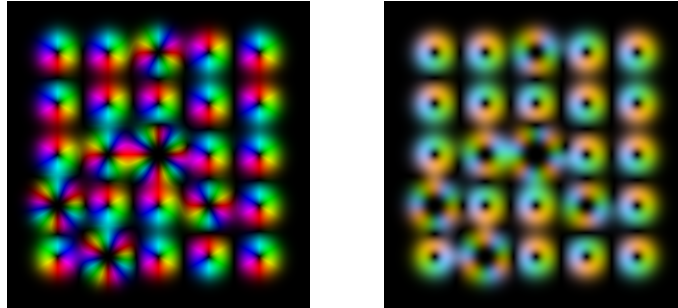
FIGURE 2.12: Comparison of HSV (left) vs. CIELAB (right) color space for representing complex amplitude. Both images are of the same array of 25 vortex beams. Notice that the vortex beams look more triangular with an HSV representation, and that there are bright bands in the yellow, violet, and teal sections. These added features hinder easy interpretation of the data. The CIELAB representation sacrifices some amount of color saturation in order to give a perceptually quantitative representation of the magnitude of the field.

CHAPTER III

ADVANCED ANALYSIS OF DIFFRACTION GRATINGS

In this chapter we will cover how to effectively and accurately analyze diffraction gratings with the thin hologram approximation. We will focus on off-axis diffraction gratings, but the process can be easily adapted to on-axis or even mixed gratings.

3.1 Grating Parameters

Off-axis diffraction gratings are characterized by four parameters:

1. the wave-function $\psi(\vec{r})$ to encode. This is a complex function that can be given as $\psi(\vec{r}) = hZ(\vec{r})\Theta(\vec{r})$, with $h > 0$ the amplitude, $0 \leq Z(\vec{r}) \leq 1$ the envelope function, and $\Theta(\vec{r})$ a complex unit phasor.

2. a groove profile (which can be constant or positionally dependent). This profile can be given in terms of its Fourier coefficients. Call these coefficients

$$c_n(\vec{r}) = |c_n(\vec{r})|\,\alpha_n(\vec{r}), \tag{3.1}$$

with $n \in \mathbb{Z}$.

3. the material parameters, which include the membrane thickness d and the complex index of refraction $\widetilde{V} = i\gamma - V$, where γ is the attenuation coefficient due to inelastic or high-angle scattering, and V is related to the mean-inner-potential of the membrane material.

4. the grating carrier vector $\vec{k}$.

27

With these parameters, the thickness profile $T(\vec{r})$ of any periodic off-axis diffraction grating milled into a thin membrane of thickness d can be given as

$$T(\vec{r}) = d - hZ(\vec{r}) \sum_{n \in \mathbb{Z}} c_n(\vec{r}) \left(\Theta(\vec{r}) e^{i\vec{k}\cdot\vec{r}} \right)^n. \tag{3.2}$$

An important detail given in Equation 3.2 is that the groove position in the diffraction grating is controlled via $\Theta(\vec{r})$. To see how this works, consider the definition of a sine function

$$\sin(x) = A \left(e^{ix} - e^{-ix} \right). \tag{3.3}$$

Here, the position of the peaks of the sine function can be controlled by changing the underlying field, say by making $x \to f(x)$, so that $\sin(x) \to \sin(f(x))$. This can be explicitly given as

$$\sin(x) = A \left(e^{ix} - e^{-ix} \right) \to A \left(e^{i(f(x)-x)} e^{ix} - e^{-i(f(x)-x)} e^{-ix} \right) = \sin(f(x)). \tag{3.4}$$

Thus the position of the grooves can be controlled by a complex unitary phasor – in this case, by $e^{i(f(x)-x)}$.

3.2 Transfer Function Expansion

Note that the wavefront immediately after interacting with the grating is a series of diffraction orders. We are interested in the mathematical form of these diffraction orders. Thus, if we consider the back plane of the diffraction grating to be at $z = 0$, we can take the wave-function $\psi(\vec{r})$ of the beam at $z = 0$ to be

$$\psi(\vec{r}) = \sum_{m \in \mathbb{Z}} \psi_m(\vec{r}), \tag{3.5}$$

where we define $\psi_m(\vec{r})$ to be the portion of $\psi(\vec{r})$ that has $m\vec{k}$ momentum added – that is, it is the mth diffraction order. It will be convenient to further expand each diffraction order

28

into an amplitude A_m, an envelope $Z_m(\vec{r})$, and a phasor $\Theta_m(\vec{r})$ via

$$\psi_m(\vec{r}) = A_m Z_m(\vec{r}) \Theta_m(\vec{r}). \tag{3.6}$$

Our goal is thus to find a periodic complex transfer function $\mathcal{T}(\vec{r})$ such that

$$\psi(\vec{r}) = \psi_i(\vec{r}) \mathcal{T}(\vec{r}) = \sum_{m \in \mathbb{Z}} A_m Z_m(\vec{r}) \Theta_m(\vec{r}), \tag{3.7}$$

where $\psi_i(\vec{r})$ is the illuminating beam, typically taken to be a plane-wave and thus ignored.

Taking equation Equation 3.2 in the thin hologram approximation, we can put this into a more useful form,

$$\mathcal{T}(\vec{r}) = \exp\left(i\widetilde{V}d\right) \exp\left(-i\widetilde{V}hZ(\vec{r}) \sum_{n \in \mathbb{Z}} c_n(\vec{r}) \left(\Theta(\vec{r}) e^{i\vec{k}\cdot\vec{r}}\right)^n\right). \tag{3.8}$$

Note that the Fourier coefficients c_n of the groove profile $f(x)$ are generated via

$$c_n = \int_{x_0}^{x_0 + \frac{2\pi}{|\vec{k}|}} f(x) e^{in|\vec{k}|x} \mathrm{d}x. \tag{3.9}$$

Because of this, $c_n = \overline{c_{-n}}$, where the overline denotes complex conjugation. This clearly gives that c_0 is real, and Equation 3.8 can be expanded into

$$\mathcal{T}(\vec{r}) = e^{i\widetilde{V}d} e^{-i\widetilde{V}c_0 hZ(\vec{r})} \prod_{n=1}^{\infty} \exp\left(-i\widetilde{V}hZ(\vec{r})|c_n| \left[\alpha_n \left(\Theta(\vec{r}) e^{i\vec{k}\cdot\vec{r}}\right)^n + \overline{\alpha_n \left(\Theta(\vec{r}) e^{i\vec{k}\cdot\vec{r}}\right)^n}\right]\right). \tag{3.10}$$

Here note that there is a relatively well known generating relation for the Bessel functions usually written as

$$e^{z(t+t^{-1})} = \sum_{n \in \mathbb{Z}} t^n I_n(2z), \tag{3.11}$$

where I_n is the modified Bessel function of the first kind. Note that in Equation 3.10, α_n, $\Theta(\vec{r})$, and $e^{i\vec{k}\cdot\vec{r}}$ are all unit-magnitude. This means that

$$\overline{\alpha_n \left(\Theta(\vec{r}) e^{i\vec{k}\cdot\vec{r}}\right)^n} = \left[\alpha_n \left(\Theta(\vec{r}) e^{i\vec{k}\cdot\vec{r}}\right)^n\right]^{-1}. \tag{3.12}$$

Thus, equation Equation 3.10 becomes

$$\mathcal{T}(\vec{r}) = e^{i\widetilde{V}d} e^{-i\widetilde{V}c_0 hZ(\vec{r})} \prod_{n=1}^{\infty} \sum_{m \in \mathbb{Z}} \alpha_n^m \left(\Theta(\vec{r}) e^{i\vec{k}\cdot\vec{r}}\right)^{nm} I_m\left(-2i\widetilde{V}|c_n|hZ(\vec{r})\right). \tag{3.13}$$

29

3.3 Product-of-Sums to Sum-of-Products

Using Equation 3.13 to determine the form of a particular diffraction order is not straight forward in the least. We wish to know the form of $Z(\vec{r})$ and $\Theta(\vec{r})$ needed to give a particular beam in, say, the first diffraction order, but it is not clear which terms contribute to the first diffraction order, nor the significance of those terms. We must put Equation 3.13 into a more useful form by rearranging the product of sums to a sum over products. To do this, lets start with something more tractable. Consider the function

$$C = \prod_{n=1}^{2} \sum_{m=-1}^{1} A(n, m) \tag{3.14}$$

As the product and sum are both small and finite, this can simply be expanded to

$$C = [A(1, -1) + A(1, 0) + A(1, 1)] [A(2, -1) + A(2, 0) + A(2, 1)] \tag{3.15}$$

$$= A(1, -1)A(2, -1) + A(1, -1)A(2, 0) + A(1, -1)A(2, 1)$$
$$+ A(1, 0)A(2, -1) + A(1, 0)A(2, 0) + A(1, 0)A(2, -1) \tag{3.16}$$
$$+ A(1, 1)A(2, -1) + A(1, 1)A(2, 0) + A(1, 1)A(2, 1).$$

Notice the pattern here – each term can be ordered by the first argument, that is, each term is of the form $A(1, x)A(2, y)$, with x and y each being either -1, 0, or 1.

This can be expressed in a more mathematical form by first making some more points clear. Note that in Equation 3.14 the product and sum are over separate domains. Call the domain of the product $\mathbb{P}$, and the domain of the sum $\mathbb{S}$. Now consider the set of all maps E from $\mathbb{P}$ to $\mathbb{S}$, that is

$$E = \{s \mid s : \mathbb{P} \to \mathbb{S}\}, \tag{3.17}$$

Clearly there are nine such maps, which can be enumerated as shown in Table 1. Notice that there is a one to one correspondence with the maps $s_m(n)$ and the terms in Equation 3.16. This is a general result when interchanging a product of sums to a sum over products. With

this, we can rewrite Equation 3.16 in the more succinct form shown in Equation 3.19. This
is a completely general result and works for any sets $\mathbb{P}$ and $\mathbb{S}$.

$$C = \prod_{n \in \mathbb{P}} \sum_{m \in \mathbb{S}} A(n, m) \tag{3.18}$$

$$= \sum_{s \in E} \prod_{n \in \mathbb{P}} A(n, s(n)). \tag{3.19}$$

TABLE 1: List of maps from $\mathbb{P} = \{1, 2\}$ to $\mathbb{S} = \{-1, 0, 1\}$. Here each $s_m(n)$ is a distinct
map, with $s_m(n) : \mathbb{P} \to \mathbb{S}$.

n	$s_1(n)$	$s_2(n)$	$s_3(n)$	$s_4(n)$	$s_5(n)$	$s_6(n)$	$s_7(n)$	$s_8(n)$	$s_9(n)$
1	-1	-1	-1	0	0	0	1	1	1
2	-1	0	1	-1	0	1	-1	0	1

Following this example, the sets in Equation 3.13 get replaced as $\mathbb{P} \to \mathbb{Z}^+$ and $\mathbb{S} \to \mathbb{Z}$,
and E becomes the set of all maps from $\mathbb{Z}^+$ to $\mathbb{Z}$ (this is an uncountably infinite set). This
allows us to put Equation 3.13 into the more usable form

$$T(\vec{r}) = e^{i\widetilde{V}d} e^{-i\widetilde{V}c_0 hZ(\vec{r})} \sum_{s \in E} \prod_{n=1}^{\infty} \alpha_n^{s(n)} \left(\Theta(\vec{r}) e^{i\vec{k}\cdot\vec{r}} \right)^{ns(n)} I_{s(n)} \left(-2i\widetilde{V}|c_n| hZ(\vec{r}) \right). \tag{3.20}$$

However, there is still one more important simplification to make – we want the form of
$T(\vec{r})$ to be a sum over diffraction orders. Note that each term carries information about
its lateral momentum via the $e^{i(ns(n))\vec{k}\cdot\vec{r}}$ term. Each diffraction order is characterized by its
lateral momentum, and thus we can pull out which terms belong to which diffraction order.
The easiest way in which to do this is to define a function g which takes a map $s \in E$ as
input and produces an integer as output ($g : s \in E \to \mathbb{Z}$). We call this function g the *order*
of s via

$$g(s) = \sum_{n \in \mathbb{P}} ns(n). \tag{3.21}$$

Then we can finally introduce $E_p \subset E$ as $E_p = \{s \in E \mid g(s) = p\}$ – that is, E_p is the subset
of E for which every $s \in E_p$ contributes only to the pth diffraction order, and every $\alpha \in E$

which contributes to the pth diffraction order is also contained in E_p. This allows us to write the transfer function as a sum over diffraction orders

$$\mathcal{T}(\vec{r}) = e^{i\widetilde{V}d}e^{-i\widetilde{V}c_0 hZ(\vec{r})} \sum_{m=-\infty}^{\infty} \left(\Theta(\vec{r})e^{i\vec{k}\cdot\vec{r}}\right)^m \sum_{s\in E_m} \prod_{n=1}^{\infty} \alpha_n^{s(n)} I_{s(n)}\left(-2i\widetilde{V}|c_n|hZ(\vec{r})\right). \quad (3.22)$$

3.4   Sinusoidal Gratings

One particularly easy case to analyze is for sinusoidal gratings. Sinusoidal gratings are defined with the Fourier coefficients $c_0 = \frac{1}{2}$, $c_1 = c_{-1} = \frac{1}{4}$, with all other $c_n = 0$. It is important to note that when milling a grating with minimal possible pitch in a FIB, the gratings will usually be quite well approximated as having a sinusoidal groove profile. With this, Equation 3.22 simplifies very nicely to

$$\mathcal{T}(\vec{r}) = e^{i\widetilde{V}d}e^{-\frac{ih}{2}\widetilde{V}Z(\vec{r})} \sum_{m=-\infty}^{\infty} \left(\Theta(\vec{r})e^{i\vec{k}\cdot\vec{r}}\right)^m I_m\left(-\frac{ih}{2}\widetilde{V}Z(\vec{r})\right). \quad (3.23)$$

Usually the desired beam is the first diffraction order, which is denoted as $\mathcal{T}_1(\vec{r})$. Taking the incident wave on the grating to be a normal plane-wave, the wave-function after interaction with the grating is simply the transfer function, thus from Equation 3.5,

$$\psi(\vec{r}) = \mathcal{T}(\vec{r}) = \sum_{m=-\infty}^{\infty} \psi_m(\vec{r}). \quad (3.24)$$

Combining this with Equation 3.6 for the first diffraction order,

$$A_1 Z_1(\vec{r})\Theta_1(\vec{r}) = e^{i\widetilde{V}d}e^{-\frac{ih}{2}\widetilde{V}Z(\vec{r})}\Theta(\vec{r})e^{i\vec{k}\cdot\vec{r}}I_1\left(-\frac{ih}{2}\widetilde{V}Z(\vec{r})\right). \quad (3.25)$$

With this, it is assumed that $Z_1(\vec{r})$ and $\Theta_1(\vec{r})$ are known, and we wish to determine $\Theta(\vec{r})$ and $Z(\vec{r})$ – this will tell us what shape of a grating will give $\psi_1(\vec{r})$. Note that we leave A_1 unspecified – this is necessary as we assume that h is specified, where h is the maximum mill depth of the grating.

When making the apodized gratings shown in Section 2.8, we set the envelope function $Z(\vec{r})$ and the phase $\Theta(\vec{r})$ equal to that of the desired beam mode, the output of which

is shown in Equation 3.25 (assuming a sinusoidal profile) – we call this an uncorrected apodized grating. To get an output beam that better matches a desired beam, we need to invert Equation 3.25 and use the resulting envelope and phase to create the diffraction grating. This results in what we call a corrected apodized grating. Equation 3.25 can only be inverted up to a maximum mill depth $h_{\max}$ (for the same reason that the sine function can only be inverted up to $\pi/2$) – we call this maximum depth the maximum invertible depth of the grating. The maximum invertible depth depends on the groove profile, the material parameters, and the energy of the electron beam, but is typically on the order of 40 nm to 70 nm for Si_3N_4 with 300 keV electrons.

The first step in solving for Z_1 and Θ_1 is to determine A_1. Since A_1 is the peak intensity in ψ_1, it is real and determined with the maximum of the Bessel function. The Bessel function of complex argument has an almost periodic structure of maxima and minima – which means that if a phase grating is milled too deep it will start to lose efficiency. Typically the maximum mill depth h is limited to be at or below the depth of the first intensity maximum for that particular diffraction order (see Figure 3.1, where the first diffraction order peaks at about 41.34 nm depth). The depth where the peak intensity occurs is the maximum depth a diffraction grating can be and still be 'invertible' – that is, at or below this depth the grating shape can be changed in order to produce exactly a desired output beam, but if it is milled deeper than this there is no guarantee that a desired output beam can still be created.

For this case, the maximum of the Bessel function occurs when $Z(\vec{r}) = 1$. If h is greater than the depth of the first maximum, the value of $Z(\vec{r})$ must be chosen such that $hZ(\vec{r})$ is the peak depth. If we let Z_m be the value of Z for which the Bessel function is maximized, we get

$$A_1 = e^{-\gamma\left(d - \frac{h}{2}Z_m\right)} \left| I_1\left(-\frac{ih}{2}\widetilde{V}Z_m\right)\right|. \tag{3.26}$$

Note that usually the designed maximum depth will be at or less than the first peak of

the Bessel function, which would then mean that $Z_m = 1$. With this, Equation 3.25 can be solved using standard numerical techniques. The standard uncorrected vs. corrected according to Equation 3.26 gratings are shown in Figure 3.2.

3.5   Binary Gratings

Another important class of gratings are binary gratings – gratings with only two height levels. Fabrication with a FIB is not well suited for creating binary gratings, but they can be produced much more accurately with E-Beam lithography. Here we analyze binary gratings using a similar procedure to the last several sections.

Binary gratings allow for a major simplification over other grating profiles in that the thickness profile $T(\vec{r})$ of the membrane has only two possible values, which we can label as T_1 and T_2, with $T_1 > T_2$. Again, utilizing the thin hologram approximation, the transfer function becomes the disjoint sum of the two zones.

Binary gratings are defined a little different than sinusoidal gratings – the envelope function is set to unity everywhere, and the Fourier coefficients become positionally depen- dent – causing the duty cycle of the diffraction grating to become positionally dependent. The Fourier coefficients are given as

$$c_n(b(\vec{r})) = \begin{cases} b(\vec{r}) & n = 0 \\ \dfrac{1}{n\pi}\sin(b(\vec{r})n\pi) & n \neq 0 \end{cases}. \tag{3.27}$$

Note here that $b(\vec{r})$ is the positionally dependent duty cycle, with $0 \leq b(\vec{r}) \leq 1$. The transfer function is the sum of each zone, giving

$$\mathcal{T}(\vec{r}) = e^{i\widetilde{V}T_1}\sum_{n\in\mathbb{Z}}c_n(b(\vec{r}))\left(\Theta(\vec{r})e^{i\vec{k}\cdot\vec{r}}\right)^n + e^{i\widetilde{V}T_2}\left(1 - \sum_{n\in\mathbb{Z}}c_n(b(\vec{r}))\left(\Theta(\vec{r})e^{i\vec{k}\cdot\vec{r}}\right)^n\right). \tag{3.28}$$

The two terms in this equation cannot be joined in this form, but the second terms transforms

as

$$1 - \sum_{n \in \mathbb{Z}} c_n(b(\vec{r})) \left(\Theta(\vec{r}) e^{i\vec{k} \cdot \vec{r}} \right)^n = \sum_{n \in \mathbb{Z}} c_n(1 - b(\vec{r})) \left(\Theta(\vec{r}) e^{i\vec{k} \cdot \vec{r}} e^{i\pi} \right)^n \qquad (3.29)$$

Since both sums in Equation 3.28 are absolutely convergent, they can be joined into a single sum

$$T(\vec{r}) = \sum_{n \in \mathbb{Z}} e^{in\vec{k} \cdot \vec{r}} \left(e^{i\widetilde{V}T_1} c_n(b(\vec{r})) + e^{i\widetilde{V}T_2} c_n(1 - b(\vec{r})) \right) \Theta^n(\vec{r}). \qquad (3.30)$$

Here each term in the sum is a single diffraction order. This can be further decomposed into two terms: the zeroth order and all others by

$$T(\vec{r}) = \left(e^{i\widetilde{V}T_1} - e^{i\widetilde{V}T_2} \right) b(\vec{r}) + e^{i\widetilde{V}T_2}$$
$$+ \sum_{\substack{n \in \mathbb{Z} \\ n \neq 0}} e^{in\vec{k} \cdot \vec{r}} \left(e^{i\widetilde{V}T_1} - e^{i\widetilde{V}T_2} \right) c_n(b(\vec{r})) \Theta^n(\vec{r}). \qquad (3.31)$$

This is because, for $n \neq 0$, $c_n(1 - b(\vec{r})) = -c_n(b(\vec{r}))$. Notice that the effect of the thickness difference of the two regions (the difference between T_1 and T_2) is to simply change the total amplitude and global phase of the resulting beams, but not their shape. For $n \neq 0$, this has the simple form

$$T_n(\vec{r}) = e^{in\vec{k} \cdot \vec{r}} \left(e^{i\widetilde{V}T_1} - e^{i\widetilde{V}T_2} \right) \frac{\sin(n\pi b(\vec{r}))}{n\pi} \Theta^n(\vec{r}). \qquad (3.32)$$

Therefore, with binary gratings, we can control the intensity distribution of a diffracted beam with the varying duty cycle $b(\vec{r})$, and we can control the phase structure with $\Theta(\vec{r})$. And as shown in Equation 3.32, the form of $b(\vec{r})$ does not depend on the sign of n, whereas the form of $\Theta(\vec{r})$ is conjugate between positive and negative orders. This means that if, say, $b(\vec{r})$ and $\Theta(\vec{r})$ are chosen to produce the beam $T_1(\vec{r}) = LG_1^0(\vec{r})$ as the first diffraction order, the same grating will give $T_{-1}(\vec{r}) = LG_{-1}^0(\vec{r})$ as the -1st diffraction order.

This can be particularly useful for dichroism experiments where beams of equal quality but opposite phase are needed. An example of a corrected binary hologram used to produce

the beam shown in Figure 2.11 is shown in Figure 3.3. Notice that unlike the corrected sinusoidal grating shown in Figure 3.2, the corrected binary grating has a plane of symmetry. This is what leads to the fact that both the positive and negative orders get corrected.

Note that this result follows closely that of Mirhosseini et. al. [59], however there are some important distinctions. Here we show that the solution given by Equation 3.32 is exact under the thin hologram approximation, whereas Mirhosseini et. al. have further assumptions that are not actually necessary. Also, we have shown this in the more general case of complex type holograms.

3.6 Blazed Gratings

Blazed gratings have an asymmetric groove profile designed to increase the intensity in the first order $\eta_1^{(T)}$. For the case of $\widetilde{V} \in \mathbb{R}$, a wave-function defined as $\Psi(\vec{r}) = A(\vec{r})e^{iP(\vec{r})}$ can be generated in the first diffraction order via [47]

$$T_1(\vec{r}) = \exp\left[iM(\vec{r})\operatorname{mod}\left(F(\vec{r}) + \vec{k}\cdot\vec{r},\ 2\pi\right)\right], \tag{3.33}$$

with

$$M(\vec{r}) = 1 + \frac{1}{\pi}\operatorname{sinc}^{-1}(A(\vec{r})), \tag{3.34}$$

$$F(\vec{r}) = P(\vec{r}) - \pi M(\vec{r}). \tag{3.35}$$

This assumes that the maximum depth h of the grating is equal to the maximum invertible depth – the first peak of the sinc function. However, when $\widetilde{V}$ has a non-zero imaginary component, this analysis no longer holds, and the more general case shown in Equation 3.22 can be utilized to determine the form necessary to produce desired diffraction orders. For the standard vortex beam, the uncorrected apodized blazed grating vs. a corrected apodized blazed grating (with the corrected depth set to the maximum invertible depth) is shown in Figure 3.4.

Blazed gratings, like sinusoidal gratings, have the disadvantage of needing a precise maximum depth and depth profile. In contrast to this, binary gratings need only the correct shape, and not a specific depth.

3.7 Arbitrary Gratings

In this section we discuss methods to solve Equation 3.22 to produce exact diffraction orders with any groove profile. One thing to note is that $e^{i\widetilde{V}d}$ is merely a global complex constant and can be ignored when not calculating the theoretical efficiency of a grating. The Fourier coefficients c_n of any groove profile will exponentially approach zero for large n, and, as seen in Figure 3.5, $|I_n(ix)| \propto x^{|n|}$. Because of this, terms in Equation 3.22 which include larger values of $s(n)$ will in general be less relevant, and those terms which do include larger values for $s(n)$ will be more relevant for smaller n.

We need some method for determining the most significant components of Equation 3.22 and of listing these terms. Each term that is included can be uniquely identified by the map $s \in E : \mathbb{Z}^+ \to \mathbb{Z}$. Focusing on the first diffraction order with $g(s) = 1$ (see Equation 3.21), one possible enumeration for each $s_n \in E_1$ can be seen in Table 2. The number of terms needed to achieve a good approximation increases dramatically as h approaches the maximum invertible depth (see Figure 3.6), with well over 10,000 terms needed when h is at the maximum invertible depth. Searching the space of all maps $s \in E$ is impractical seeing as E is uncountably infinite.

One way to generate a large number of significant s_n maps is to combine a brute force searching method over a small parameter space with various patterns that contribute to the desired diffraction order. For a brute force search over the range $1 \leq n \leq 8$ and $-6 \leq s(n) \leq 6$, there are a total of 13^8 terms to search over – more than 800 million. However, in spite of this, there are terms that can be as significant as the top 30 of all terms that are not found with this brute-search method.

TABLE 2: List of the first ten most significant terms from Equation 3.22 for a blazed grating. For this, the terms were calculated for $1 \leq n \leq 100$, with $\widetilde{V} = \pi/(33 \text{ nm})(0.08i - 1)$, which is relevant for Si_3N_4 with 300 keV electrons. The parameter h is set to the maximum invertible depth for this, which is about 70 nm. Each map $s_m(n)$ has order 1, as seen from Equation 3.21: $\sum ns(n) = 1$, thus each term is confirmed to contribute to the first diffraction order.

n	1	2	3	4	5	6	7	8	9	10	11	12	Magnitude
$s_1(n)$	1	0	0	0	0	0	0	0	0	0	0	0	1.00000000
$s_2(n)$	-1	1	0	0	0	0	0	0	0	0	0	0	0.26458093
$s_3(n)$	0	-1	1	0	0	0	0	0	0	0	0	0	0.08379359
$s_4(n)$	-2	0	1	0	0	0	0	0	0	0	0	0	0.07353857
$s_5(n)$	0	0	-1	1	0	0	0	0	0	0	0	0	0.04139040
$s_6(n)$	-1	-1	0	1	0	0	0	0	0	0	0	0	0.03457848
$s_7(n)$	3	-1	0	0	0	0	0	0	0	0	0	0	0.03374657
$s_8(n)$	0	0	0	-1	1	0	0	0	0	0	0	0	0.02471804
$s_9(n)$	2	1	-1	0	0	0	0	0	0	0	0	0	0.01945690
$s_{10}(n)$	-1	0	-1	0	1	0	0	0	0	0	0	0	0.01825010

The brute force search only reveals a small subset of the leading contributing terms. In order to see this, consider the set of terms defined by all terms zero except the nth term -1 and the $n + 1$ term $+1$ (as seen in Table 3). When listing the top 1000 contributing terms, these pairs are very prominent, with the final $+1$ term landing near $n = 50$ and still being within the first 1000. This means that these terms must be added to those found by the brute search method, as well as other patterns which can easily be identified. See Appendix A for detailed information on both the brute force method and the pattern generation method.

For a blazed hologram with $\widetilde{V} = \pi/(33 \text{ nm})(0.08i - 1)$, the maximum invertible depth is 71.89 nm. With $h = 68.5$ nm, the above method was used to find more than 375,000 terms, which were sorted into the most significant 50,000, as can be seen in Figure 3.6.

Note that when generating the contributions for each s_n, the calculation must include each zero term in the sequence, as this term will be nearly but not precisely unit magnitude, the contribution of dozens to hundreds of these nearly unit magnitude terms is significant. Each calculated term should run over the full range of n values. For the simulations shown

38

here, the range was from $1 \leq n \leq 100$.

TABLE 3: List of the first ten pairs of the form $\ldots, -1, 1, \ldots$. Each of these terms contributes to the first diffraction order. Note that the term $s_{10}(n)$ below is the 31st term by list of significance for a blazed grating with max h (see Table 2). A brute force search over $1 \leq n \leq 8$ and $-6 \leq s(n) \leq 6$ searches more than 800 million terms but would not have found $s_9(n)$ or $s_{10}(n)$ shown below.

n	1	2	3	4	5	6	7	8	9	10	11	12
$s_1(n)$	-1	1	0	0	0	0	0	0	0	0	0	0
$s_2(n)$	0	-1	1	0	0	0	0	0	0	0	0	0
$s_3(n)$	0	0	-1	1	0	0	0	0	0	0	0	0
$s_4(n)$	0	0	0	-1	1	0	0	0	0	0	0	0
$s_5(n)$	0	0	0	0	-1	1	0	0	0	0	0	0
$s_6(n)$	0	0	0	0	0	-1	1	0	0	0	0	0
$s_7(n)$	0	0	0	0	0	0	-1	1	0	0	0	0
$s_8(n)$	0	0	0	0	0	0	0	-1	1	0	0	0
$s_9(n)$	0	0	0	0	0	0	0	0	-1	1	0	0
$s_{10}(n)$	0	0	0	0	0	0	0	0	0	-1	1	0

3.8 Fourier Transform Corrections

As the maximum mill depth h approaches the maximum invertible depth, the number of terms needed to get a result of high accuracy increases drastically, which is to say that the distribution of the contributions has very a long tail as h approaches the maximum depth. A more practical but less rewarding method for determining how to shape a grating can be given numerically through the use of the Fourier transform.

Consider for convenience a sinusoidal grating that has $Z(\vec{r}) = \Theta(\vec{r}) = 1$ everywhere. This grating is infinite in size, but by taking the Fourier transform of it, one will get a series of delta functions of various amplitudes. That is,

$$\mathcal{F}\{\mathcal{T}(\vec{r})\} = \mathcal{F}\left\{\exp\left(i\widetilde{V}d\right)\exp\left(-\frac{1}{4}i\widetilde{V}h\left(2 + e^{i\vec{k}\cdot\vec{r}} + e^{-i\vec{k}\cdot\vec{r}}\right)\right)\right\}, \tag{3.36}$$

$$= \exp\left(i\widetilde{V}d\right)\exp\left(-\frac{1}{2}i\widetilde{V}h\right)\mathcal{F}\left\{\exp\left(-\frac{1}{2}i\widetilde{V}h\cos\left(\vec{k}\cdot\vec{r}\right)\right)\right\}. \tag{3.37}$$

This can be simplified using the Jacobi-Anger expansion, which states

$$e^{iz\cos\theta} \equiv \sum_{n\in\mathbb{Z}} I_n(iz)e^{in\theta}. \tag{3.38}$$

With this, and utilizing the linearity of the Fourier transform, Equation 3.37 becomes

$$\mathcal{F}\{\mathcal{T}(\vec{r})\} = \exp\left(i\widetilde{V}d\right)\exp\left(-\frac{1}{2}i\widetilde{V}h\right)\sum_{n\in\mathbb{Z}} I_n\left(-\frac{1}{2}i\widetilde{V}h\right)\delta\left(n\vec{k}-\vec{r}\right). \tag{3.39}$$

Notice the similarity between this equation and Equation 3.25 with $Z = \Theta = 1$. For a particular value of hZ in Equation 3.25, the same result will show here for the equivalent value of h.

The reason this happens is because of the constancy of the grating assumed. Fourier transforms are maximally non-local – the value of the Fourier transform at any point includes a particular sum over all points of the operand. However, because all points of the operand are the same (over a period), the global coefficient given by the Fourier transform exactly correlates to the local coefficient of corresponding diffraction order just after interaction with the diffraction grating.

This applies for all gratings, not simply sinusoidal gratings. What this means is that a raster of the basic groove profile can be generated, and this can be used to create the correction curve for a particular diffraction order by taking the Fourier transform of the profile for specific mill depths.
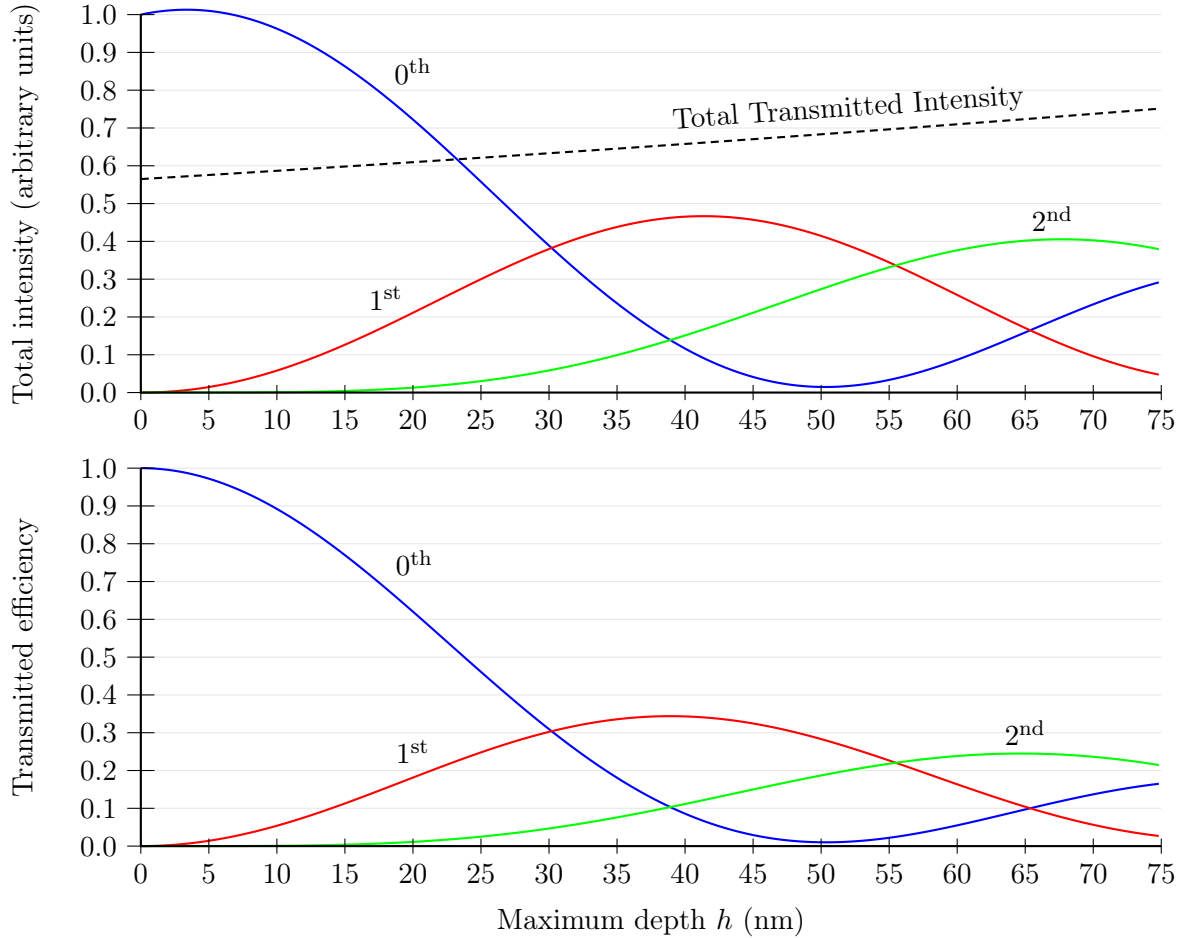
FIGURE 3.1: (Top) Beam intensity vs. depth for several diffraction orders for a sinusoidal phase grating, together with the total transmitted intensity as a fraction of the incident intensity. (Bottom) The transmitted efficiency vs. depth for the same diffraction orders – this is taken by dividing the beam intensity by the total transmitted intensity. For a sinusoidal grating, the intensity of the positive orders exactly matches the negative orders, such that the curve for the $+1$ and -1 orders are identical, as are the $+2$ and -2 orders, etc. Shown is the zeroth (blue), first (red), and second (green) diffraction orders. The parameters used for this simulation were $\widetilde{V} = \pi/(33 \text{ nm})(0.08i - 1)$ with a membrane thickness of $d = 75$ nm. Note that the peak invertible depth is taken from the intensity curve (top), where the peak occurs at 41.36 nm for the first diffraction order, and not the peak of the transmitted efficiency curve, which occurs at 41.36 nm for the first diffraction order. For the top plot, the total transmitted intensity is relative to the incident beam, and the units correlate to the y-axis.
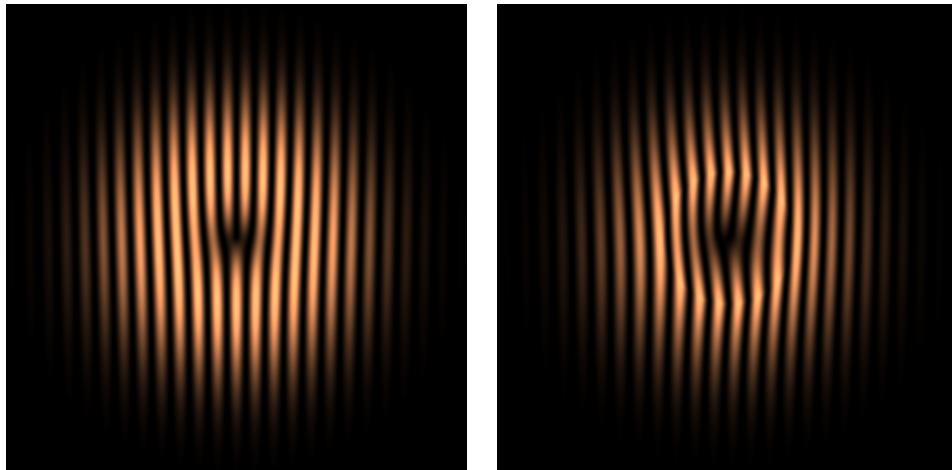
FIGURE 3.2: Standard uncorrected apodized fork hologram (left) vs. a corrected hologram (right) set to the maximum invertible depth of 41.36 nm. Equation 3.26 was used to generate the corrected hologram.
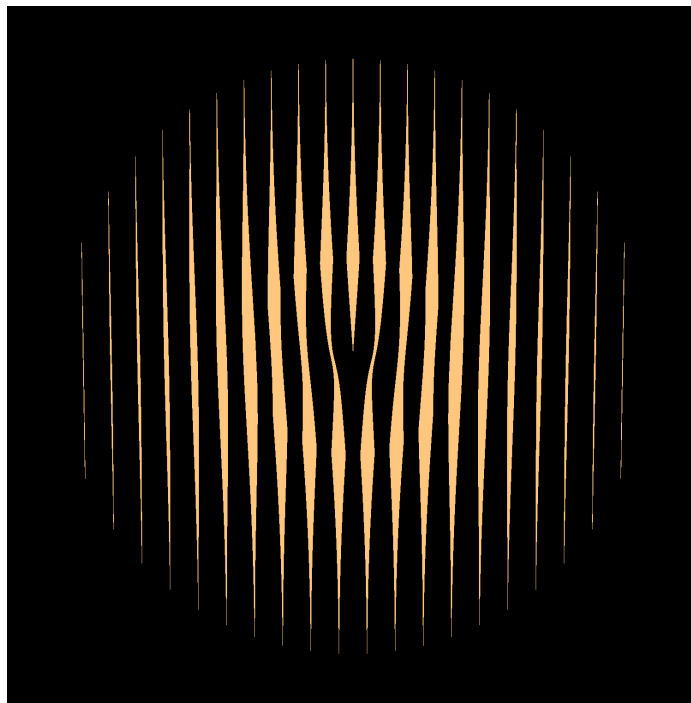
FIGURE 3.3: Corrected binary forked hologram that gives the beam shown in Figure 2.11. Binary holograms of this form give an exact diffracted beam (up to intensity and phase) regardless of the depth to which they are milled.
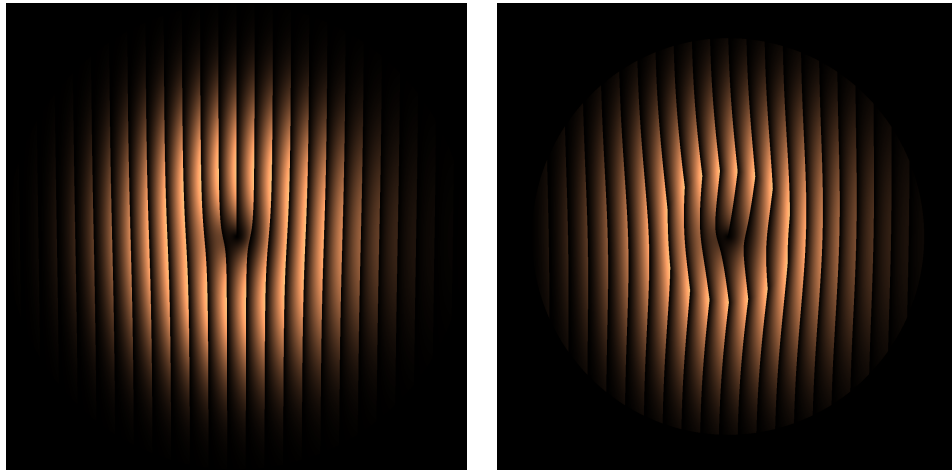
FIGURE 3.4: Blazed uncorrected apodized fork hologram (left) vs. a corrected hologram (right) set to the maximum invertible depth of 71.9 nm. The corrected hologram utilized Equation 3.22 to generate the corrections.
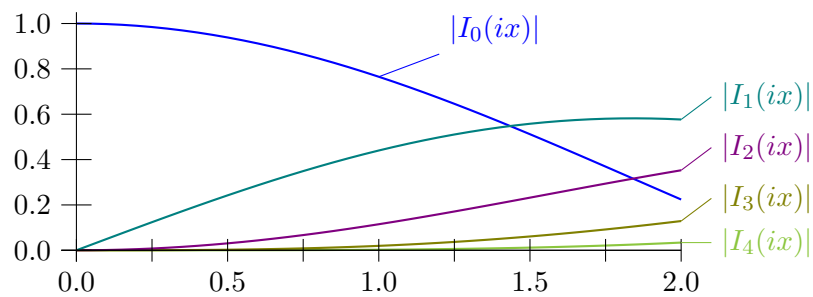
FIGURE 3.5: Plot of the first several modified Bessel functions of the first kind with purely imaginary argument. Note that for small argument (below the first maxima of I_1), the Bessel functions rapidly approach zero as the order increases. Also, within the first maxima of I_1, the Bessel functions are all monotonic. The expansion about $x = 0$ shows that, for small x, $|I_n(ix)| \propto x^{|n|}$ for $n \neq 0$, and $|I_0(ix)| \approx 1$.
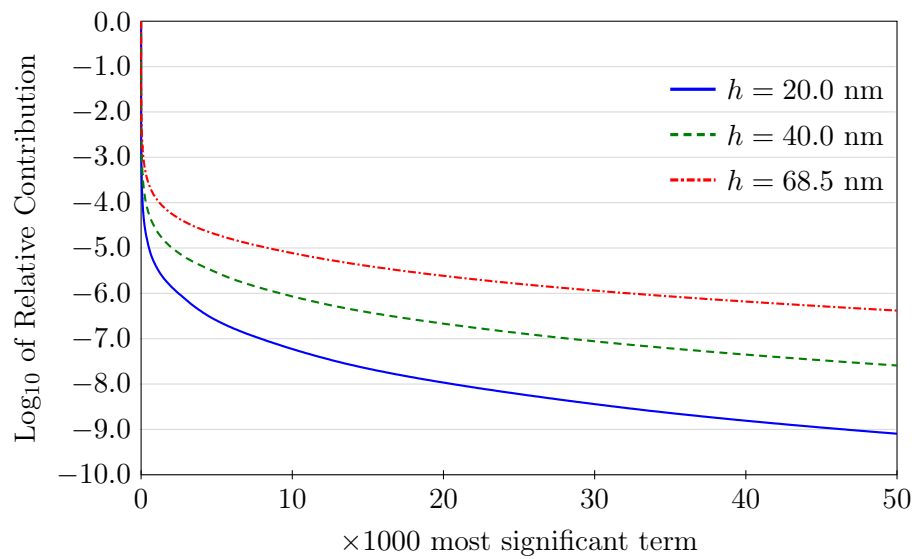
FIGURE 3.6: Most significant 50,000 terms for blazed gratings of various depths. Each term is listed in order of its contribution magnitude relative to the most significant term. Notice the log scale – the tails are very large for this method.

CHAPTER IV

FABRICATION OF ELECTRON DIFFRACTION GRATINGS WITH FOCUSED ION
BEAM MILLING

This chapter covers the grating manufacture methods as they have been developed in our lab. There are a wide range of techniques available, each having certain advantages and disadvantages. The main considerations for each method are the reliability, complexity, and scalability. For gratings created for research purposes, the main consideration is usually what is most easily available. The three methods that have been explored in our group are Focused Ion Beam (FIB) milling, Electron Beam lithography (E-Beam Lithography), and Electron Beam induced deposition (EBID). I was the primary contributor to the development of both FIB milling techniques as well as EBID techniques, while Tyler Harvey was the primary contributor to the E-Beam lithography that our group has done.

The goal of fabricating a diffraction grating is to impart a desired shape into the diffracting medium (discussed in more detail in Section 3). It is impossible for any fabrication method to exactly reproduce a specific desired shape, but fabrication methods usually have higher precision in the position of a feature than the shape of that feature. Because of this, we split the shape of the diffraction grating into two main components: the groove shape and the groove position. For instance, Figure 2.11 shows an example grating design where the groove shape is sinusoidal, and the groove position is such as to create a fork hologram. The degree to which a diffracted beam depends upon these two parameters varies, but generally speaking the position of the grooves plays larger a role in determining the how well a diffracted beam reproduces a desired beam than the groove shape does.

A Focused Ion Beam is a device that is capable of accelerating and focusing one of several ion species to a high voltage of typically 30 keV, with spot sizes as low as tens of nanometers. Our lab has use of a Helios NanoLab DualBeam from ThermoFisher Scientific,

which is capable of accelerating a beam of Gallium ions up to 30 keV with an extremely high lateral positioning capability.

Our group has primarily utilized FIB milling for our diffraction gratings, so the primary emphasis of this chapter will be on FIB milling. The initial techniques and grating designs for the FIB milling were developed by Ben McMorran, and I have expanded upon these and developed an advanced computer program for the generation of special files which are needed for the Helios DualBeam to correctly fabricate diffraction gratings.

4.1   FIB Interaction Zone

The interaction of a focused beam of ions with a sample is a complex process involving the removal of material via sputtering, re-deposition of some of the sputtered material, and implantation of some of the incoming ions. The interaction zone of a focused ion beam tends to be several times larger than the spot size of the beam, and it is this interaction zone that will determine the final shape of a milled structure.

For FIBs utilizing a Gallium source, the extraction and acceleration methods, as well as the large current, limit the energy resolution of the beam and cause various forms of beam broadening. The result is that the focused ion beam typically has an intensity curve somewhere between a Gaussian (close to the optical axis) and a Lorentzian (for the tails). Because of this, the reported resolution / spot size of a given aperture (which is determined for imaging, not milling, purposes) tends to be much lower than the useful minimum feature size millable for said beam.

Within the FIB, there are several current-limiting apertures which have a direct impact on the focused spot size of the beam. These instruments are not diffraction limited, so smaller apertures tend to increase the spatial coherence of the beam, thus allowing for smaller focused probe sizes. With the Helios DualBeam, the relevant apertures are labeled in terms of beam current, with 1.4 pA, 7.6 pA, and 20 pA being the most commonly used

for milling diffraction gratings on the order of 100 nanometer pitch. These are the target current for each aperture – the actual current increases with use as the aperture physically widens from beam exposure. Larger apertures are available, with apertures larger than 5.5 nA common, but these are not typically useful for generating electron diffraction gratings with required feature sizes on the order of 100 to 200 nm.

Electron diffraction gratings are fundamentally a periodic structure of slits or grooves with a desired maximum depth. Because of the long Lorentzian like tails of a FIB, the maximum depth achievable is highly dependent on the spacing of the grooves. For apertures of around 10 pA with a desired depth of 30 nm (for Si_3N_4), the minimum groove spacing is about 100 nm. One of the characteristics of Si_3N_4 that makes it quite ideal for milling diffraction gratings is its exceptional toughness, thus allowing very thin membranes to still be structurally sound enough to hold a grating pattern. However, because of this toughness, Si_3N_4 mills relatively slowly within a FIB, limiting the maximum size a diffraction grating can be made.

4.2   Pattern File Generation

The Helios DualBeam FIB allows users direct control the beam position DAC within the ion column via Stream files. These files contain a list of x- and y-coordinates, as well as dwell time information, necessary to complete the milling process. While these files can be provided to the machine to perform a milling operation, ThermoFisher provides no tools for the generation of Stream files, and a significant portion of my work has been in the development of a rapid and reliable method for creating these files.

The most simple grating to produce is a sinusoidal grating, in which the groove shape closely approximates a sinusoid. This shape is particularly easy because of the fact that the convolution of a Dirac comb $Ш_k(x)$ with a Gaussian of FWHM on the order of k is

approximately a sinusoidal, as given in

$$\text{III}_k(x) \circledast e^{-\frac{x^2}{2\sigma^2}} \approx A(\sigma/k)\sin\left(\frac{2\pi}{k}x\right) + h \qquad (4.1)$$

where k is the spacing of the Dirac comb, h is a constant, and A is the amplitude of the sinusoid. This means that as long as the groove spacing is narrow enough, a sinusoidal groove pattern can be milled with a FIB simply by having the machine mill only the peaks of the desired function. This correlates to the image shown in Figure 4.1, where only the peaks from Figure 2.11 are utilized for milling, and the interaction zone of the FIB will widen this out to create an approximate sinusoidal shape. The process of converting a desired hologram such as that in Figure 2.11 to that shown in Figure 4.1 is called single-pixelizing.
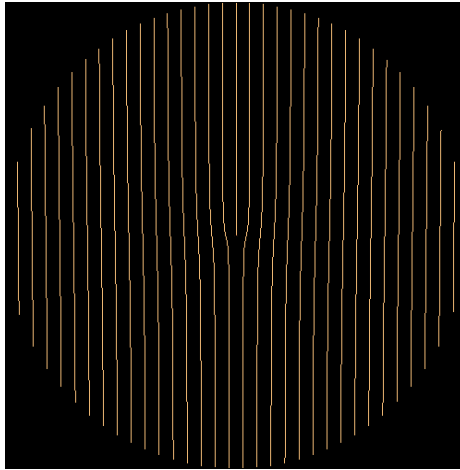
FIGURE 4.1: A single-pixelized version of the grating pattern shown in Figure 2.11, which is used to generate the Stream file necessary for fabrication of the grating. This pattern must be supplied to the FIB in such a way as to most accurately mill the desired pattern.

The goal of the pattern file generation software is to convert the data in Figure 4.1 into a list of coordinates and dwell times. There are a number a ways in which this can be done which can have an effect on the fabricated grating. For instance, one can search vertically through the data, retrieving all of the non-zero entries in each column and simply chaining these together. However, the intuitive approach is to have the ion beam follow each groove

48

from top to bottom, then move to the next groove.

Seeing as that most off-axis holograms can be decomposed into a collection of grooves, the method which I have developed involves collecting each of the grooves in a single line representation, so that each groove can be completely milled before the beam moves to another groove. The sequence in which the grooves are milled can either be sequential, say from left to right, or in a more complicated manner. I have tested various methods for ordering the sequence in which the grooves are milled, including left-to-right, outer-to-inner, and inner-to-outer. However, no method was significantly superior to a standard left-to-right sequence, with many of the tested methods giving consistently worse results. Thus, all gratings developed are milled in a sequential manner from left to right.

4.3 Helios DualBeam Procedure

The Helios DualBeam is a fantastic piece of hardware capable of a huge range of applications with its electron beam and ion beam. Utilizing a FIB such as the DualBeam for creating electron diffraction gratings is a rather niche and new use-case, and much work has gone into the generation and optimization of procedures for creating high quality diffraction gratings. In particular, the methods for substrate preparation, machine preparation, focusing procedures, and milling techniques have been primarily developed by myself.

The ion beam used to mill the diffraction gratings is not neutralized before interaction with the sample, and thus charge implantation can be an issue, especially because Si_3N_4 is a good insulator. For this reason, the surface of the Si_3N_4 must be coated with a conducting layer. This has the added benefit of also allaying any charging issues the grating may face within an electron beam.

To ensure good adhesion of the charge alleviation layer the Si_3N_4 membranes should first be plasma cleaned. We use an Oxygen-Argon plasma at 25 watts power for 5 minutes to ensure good surface cleaning. The Si_3N_4 is quite robust against the plasma and we have

not observed any plasma-based damage even at high wattage for extended periods of time.

4.4 Carbon Coating

A quick, cheap, and effective method to coat the membranes with a conducting layer is to coat them with carbon from a thermal source. This can be done quickly using standard carbon-coating machines, and has nanometer thickness resolution. Reliably achieving a specific carbon thickness with this method can be a little difficult, but variations of the carbon thickness play little role in the mill effectiveness. To achieve a good charge alleviation layer, carbon thickness should be on the order of 10 nm, with both the front and back of the membrane coated. This will ensure that any implanted charge from the ion beam will not push the beam around during milling.

Carbon coating has the added benefit of being easily removable, in the case that post processing is necessary. Carbon can be easily removed via plasma cleaning with an oxygen rich plasma. Silicon nitride is quite robust against oxidative plasma, with no damage seen after 20 minutes under a 50 watt oxygen rich plasma.

4.5 Sputter Coating

Sputter coating is an effective method to achieve a reliable charge alleviation layer, with various metals available to be utilized. Mostly notably, we have had success with a gold-palladium source. This method can quickly and reliably create very precise thickness profiles, but the metal coating seems to have low adhesion to the Si_3N_4membranes used. Thick layers will often lose adhesion and peel away.

4.6 E-Beam Evaporation

Our lab has access to an Angstrom E-Beam deposition machine, which allows coating with metals withing a high vacuum environment with a wide range of materials available.

Due to the high vacuum and small evaporation size of the heated material, this allows for a very accurate growth of material layers that have very small grains.

We have found that a layer of 3-5 nm of Titanium followed by 3-5 nm of Platinum is ideal in creating a very robust charge alleviation layer. For best results, both sides of the membrane should be coated, although having only one side coated can produce acceptable results.

4.7   Preparing Membranes for Milling

Once the desired charge alleviation layer has been added to the membrane, there remains one critical final step to ensure proper milling. The membranes must be left in the FIB chamber long enough to ensure thermal equilibrium with the chamber. Milling time can easily exceed an hour, during which time any stage drift will ruin the mill. The membranes, and especially the membrane holder can be tens of degrees cooler than the chamber. The temperature of the grating holder can be raised simply by holding in ones hand for a few moments before placing it in the FIB chamber. Typically, once the vacuum has been established within the chamber, the system should be allowed to equilibrate for one to two hours before milling.

4.8   Focusing the Ion Beam

During the waiting period for the chamber to equilibrate, the focusing procedure for the ion beam can be carried out. This procedure has been developed by myself and is a reliable way to achieve quite consistent results with the ion beam. There are inherent instabilities within the ion beam column that can make the same milling procedure produce different results from one day to the next – namely that the ion beam actively etches the apertures in the system, causing the current to increase and even causing asymmetric wear on the apertures. This has the effect of making the spot size of the ion beam increase during the

life-cycle of the apertures. With a new aperture system, an aperture that is rated to deliver 7.6 pA usually starts very close to the stated current, but toward the end of the life-cycle, this can easily reach double the current. I have had a 7.6 pA aperture deliver almost 20 pA and still be somewhat useful. This must be taken into consideration when focusing the ion beam. The actual current delivered to the specimen is reported in the UI of the instrument, and keeping track of this is useful in developing the diffraction gratings.

The procedure for focusing the ion beam begins by aligning the sample to eucentric height so that the electron beam can be used to image the system during the milling process. For this, select an easily recognizable feature on the edge of the silicon structure, bring the sample to eucentric height, and perform preliminary focusing of the ion beam and the electron beam. After this initial alignment and focusing, move to a section of the TEM holder that is near the membrane and mill a line (or series of lines). As the FIB is milling the lines, adjust the focus and stigmators on the FIB until the cut is as sharp as possible. To achieve the highest level of consistent focus, perform the same focusing procedure on a corner of the membrane with the milling time per pixel just high enough to cut through the membrane. Under this condition, there should be a range of defocus available that will still cut through the membrane – for instance, it might be possible to turn the fine focus knob a full three rotations until the FIB stops cutting through the membrane, in which case the knob should be set in the center (so one an a half turns in either direction will cause the beam to stop cutting through the membrane). Do this for the focus and stigmator, then decrease the dwell time on the lines by a small amount and go through the procedure again. This is the method that generates the most consistent focus between milling sessions.

CHAPTER V

APPLICATION OF ELECTRON DIFFRACTION GRATINGS

In this chapter we discuss several uses of diffraction gratings that have been studied by our group. Electron diffraction gratings have been used to correct the spherical aberration within a TEM [22, 60], to study chiral plasmons in nanoparticle clusters [20], advanced phase imaging within a TEM [27], and create Mach-Zehnder type interferometers within a TEM [38], to name a few. All of these applications require high quality diffraction gratings made to exacting specifications. The work I have done has allowed me to contribute in both the analysis and discussion of these topics, as well as design and create advanced diffraction gratings for each of the references above. For the work with aberration correction, Martin Linck came up with the idea for aberration correction utilizing diffraction gratings, Benjamin McMorran and I worked to design the grating, and I made the final design decisions and fabricated the grating. For the work on vortex beams, Benjamin McMorran developed the idea and computer code for generating the holograms, as well as initial fabrication, Tyler Harvey developed several applications and worked some with fabricating the gratings, while I developed the theory of how to best design and fabricate vortex beams – I also optimized the fabrication process. For the work on enhanced phase contrast imaging Colin Ophus developed the idea and Tyler Harvey helped with the theory of image formation, while I helped with the design and provided the expertise to manufacture the gratings. For the work on counter-rotating beams, I developed the idea, manufactured the gratings, and performed the analysis. For the work on highly twisted beams, Andrew Forbes and Jason Webster came up with the idea of angularly accelerating electron beams, while Benjamin McMorran and I provided the connection with continuously rotating electron beams; I made the gratings, took the data, and performed the analysis of the electron energy loss, while Jason Webster performed the rotation acceleration analysis and provided the theory.

53

5.1 Aberration Correction

This section is an overview of the paper by Linck *et al.*, *Ultramicroscopy* 182:36-43 (2017) [22]. Martin Linck came up with the idea of an aberration correcting diffraction grating. Benjamin McMorran and myself helped with the design of the grating, while I made the final design and the fabrication of the grating.

The focusing lenses within an electron microscope are rotationally symmetric dipole lenses. According to Scherzer's lemma [61], electromagnetic lenses that are rotationally symmetric cannot be designed to focus an electron beam without spherical aberration. Non rotationally symmetric lenses such as quadrupoles, hexapoles, and octopoles can be utilized to remove spherical aberration within an electron microscope [62], however these multipole solutions are expensive to implement and have complicated alignment procedures. Also, other aberrations besides spherical can be corrected or mitigated with complex multipole lenses, allowing aberration corrected STEM's to reliably achieve sub Ångstrom resolution.

Aberration correction within a TEM comes in two forms: pre-specimen or post-specimen. Post-specimen correction can be used to improve image resolution and contrast [63], while pre-specimen correction produces a more tightly focused probe for STEM [64]. There are many STEM's that are not aberration corrected that can be fitted with diffraction gratings. Diffraction gratings allow for a low cost alternative to installing expensive aberration correction equipment.

The primary source for probe aberrations within a TEM is the objective lens. The aberrations are modeled using a spherical coordinate system. As ideally the lens will focus all rays to a point, the rays converge to that point with angle θ relative to the optical axis, and ϕ azimuth. The magnitude r of the rays can be ignored. For spherical aberration, the wavefronts become distorted according to

$$\chi_{\mathrm{OL}} = \frac{2\pi}{\lambda} \frac{C_3}{4} \theta^4,$$

(5.1)

where χ_{OL} is the spherical aberration of the objective lens, λ is the electron wavelength (1.97 pm for 300 keV electrons) and C_3 is the spherical aberration coefficient.

We wish to design a grating that can mitigate this aberration. Because of the action of the focusing lens, χ_{OL} can be correlated to a grating that has a phase term proportional to $|\vec{r}|^4$, where $\vec{r}$ is the distance from the center of the grating ($\vec{r}$ is constrained to the plain of the grating). Thus, for a probe-forming lens of a given focal length f and aperture magnification M,

$$\chi_{\mathrm{G}} = C_{\mathrm{G}} |\vec{r}|^4 = \frac{2\pi}{\lambda} \frac{C_3}{4} \left(\frac{M|\vec{r}|}{f} \right)^4. \tag{5.2}$$

Note that if the optical setup is changed to achieve a different probe convergence angle with the same aperture, the magnification M will alter, requiring a new diffraction grating. Thus, a grating can only correct spherical aberration for exactly one optical setup.

As a demonstration of spherical aberration correction utilizing an electron diffraction grating, we designed a 70 μm diameter grating with $C_{\mathrm{G}} = 6.23 \times 10^{-5}$ $\mu\mathrm{m}^{-4}$. This gives a probe illumination semi-angle of $\theta_{\mathrm{max}} = 17.5$ mrad ($f/M = 2$ mm). The grating was a very large grating compared to what is normally made with the FIB. The pitch was set close to the minimum limit of what we could achieve on the FIB at 80 nm, giving 875 bars for the grating. This grating was milled with a nominal 7.6 nA aperture and a nominal depth of $\tilde{1}0$ nm. A detailed overview of the diffraction grating is shown in Figure 5.1.

Since spherical aberration is proportional to θ^4, the larger the diameter of the probe-forming aperture the more the effects of spherical aberration will be apparent. In order to emphasize the effectiveness of the grating at correcting spherical aberrations, we needed the microscope to be in a regime with more spherical aberration that would be normal, thus we chose a larger probe-forming aperture of 70 microns, where 50 microns is typical within our microscope.

The manufacturing difficulty of a grating is proportional to the pitch and the size of the grating. The pitch of the grating determines the maximum current that can be used
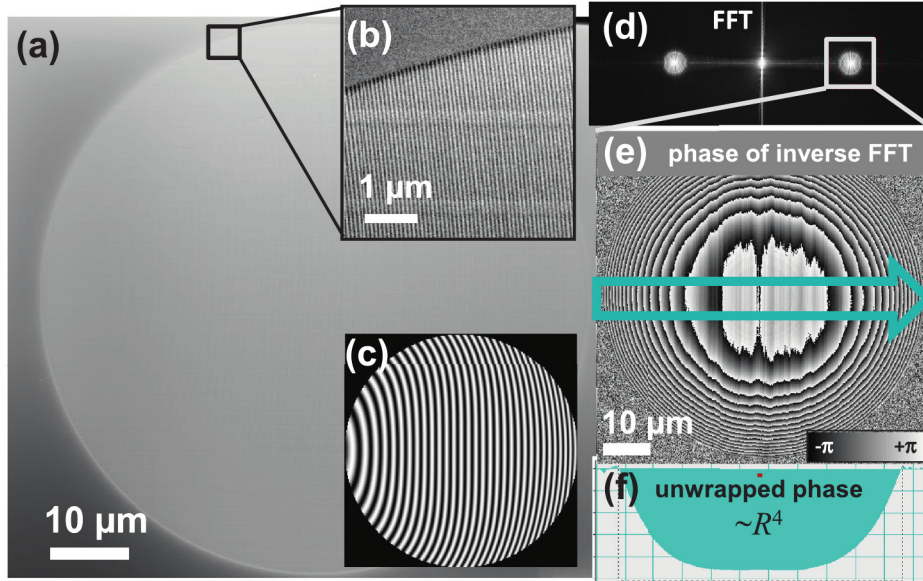
FIGURE 5.1: High resolution scanning electron microscope (SEM) image (a) of the entire diffraction grating for spherical aberration correction. The inset (b) shows the curvature of the grating bars similar to the idealized exaggerated model shown in (c). By taking the Fourier transform of the SEM image, the geometric phase (mod 2π) of the grating can be recovered (e). Unwrapping the phase (f) demonstrates the R^4 dependence, where $R = |\vec{r}|$. Reprinted with permission from [22].

to mill, in this case, a current of about 8 pA was used, which is a very small current with slow mill times. For a given pitch, the larger the grating the longer it will take to mill. To get optimal diffraction efficiency, a sinusoidal grating should be on the order of 35 nm deep in Si_3N_4, which correlates to well over 10 hours of mill time for a 70 micron grating at 8 pA. The FIB we used is not stable over this time period, so a trade-off of less mill time (lower efficiency) for a more accurate phase reconstruction was necessary. We needed the beam intensity to be large enough so as to have an acceptable signal to noise ratio, thus we made many attempts to fabricate this grating until we could determine the optimal milling conditions. For future work in spherical correction, an alternative fabrication method such as E-Beam lithography might be more suitable.

The spherical aberration correcting grating was able to produce a beam of higher res-

olution than the uncorrected probe. To test this, under the appropriate optical setup, the each of the $+1$, 0, and -1 diffraction orders were selected using a selected-area aperture and focused on an amorphous sample to produce a Ronchigram. The Ronchigram can be used to determine the aberrations in a system using the principle that an infinitely focused probe on an amorphous sample will produce an outgoing spherical wave. Thus the diffraction plane image of the focused probe on an amorphous sample will contain information about how tightly focused the probe was – specifically the area which is 'flat' in the diffraction plane image represents the area (the solid angle) for which the aberrations in the probe are minimal. For our spherical aberration correction grating, the corrected probe has minimal aberrations for 17.5 mrad convergence semi-angle, whereas the uncorrected zeroth order has minimal aberrations only over 8.2 mrad convergence semi-angle, as shown in Figure 5.2.

5.2   Vortex Beams

Another important application for electron diffraction gratings is to create vortex beams typically of the form LG_0^m for nonzero m (see Equation 2.14). These beams have the property that the electrons have an extrinsic orbital angular momentum (OAM) about the propagation axis of the beam. This OAM is also referred to as topological charge or a phase singularity – both of which refer to the $e^{im\phi}$ component of the beam.

Vortex beams were first observed and studied by Nye and Berry [65], where they used ultrasound reflecting off rough surfaces to better understand radar echoes from surfaces. These vortex beams have been studied in optics since the 1990 [66] and have been employed in countless applications from enhanced imaging [67] to sample manipulation [5].

There are many potential applications of vortex beams within an electron microscope. Of particular interest initially was the potential of utilizing the non-zero magnetic moment of an electron vortex beam to probe nanoscale magnetic fields within a sample. While this measurement has not yet been realized, there have been other useful applications. One such
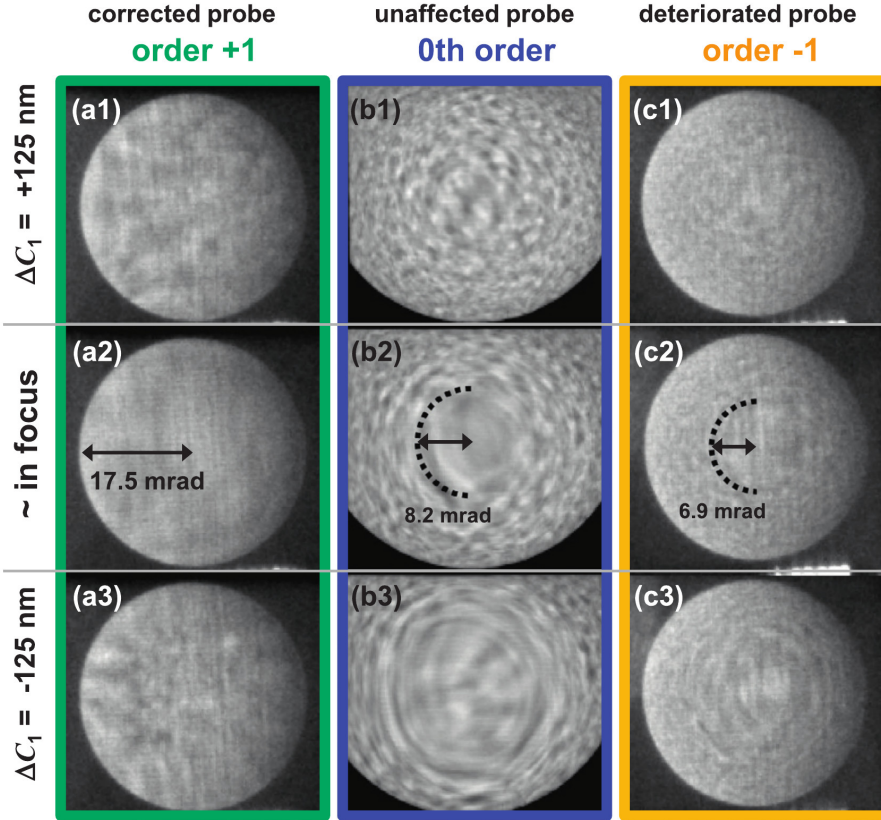
FIGURE 5.2: The Ronchigrams of the spherical aberration corrected +1 order beam (a), the unaffected zeroth order beam (b), and the −1 order beam (c) which has twice the spherical aberration of the zeroth order beam. For each beam, a Ronchigram was taken for three different focal planes: at focus, and symmetrically defocused by ± 125 nm. For the focused probes, the Ronchigram is quite flat over 17.5 mrad convergence semi-angle (a2), whereas the Ronchigrams for the uncorrected probe has a considerably smaller flat zone of 8.2 mrad (b2). Reprinted with permission from [22].

application is the demonstration of electron helical dichroism [20].

Electron helical dichroism looks at the differing signals produced as a right-handed vortex beam vs. a left-handed vortex beam interacts with a sample. While the causes of various differences are from a variety of sources, the interaction of an electron beam with a sample can be broadly placed into two modes: electron interactions and bulk / lattice interactions.

Electron interactions occur when an electron in the sample is excited to a different state by the incident beam. The cross-section for any particular transition depends on the initial state, the final state, and the state of the incident probe. Dichroism occurs when the cross-section for a particular transition is highly dependent on the OAM state of the incident beam.

Bulk interactions are those for which the plasmons or phonons within the sample are activated by the incident beam. These modes can have a high dependence on the geometry of the sample – especially for nanoparticles. For example, Tyler Harvey demonstrated a dichroic signal with a chiral arrangement of nanoparticles [20]. For this experiment, a high quality diffraction grating capable of generating accurate and bright $+1$ and -1 diffraction orders was necessary. The pitch of the grating needed to be minimized in order to have well separated beams, and the size of the grating needed to be as large as possible to acquire more brightness into the diffracted probes. An overview of the optical setup and the probes formed with this grating is shown in Figure 5.3. Using these vortex beams, Tyler Harvey was able to demonstrate a dichroic signal consistent with surface plasmon resonances.

This method provides microscopists with an additional tool to analyze and characterize specimens.

5.3 Enhanced Phase Contrast Imaging

This section is an overview of the paper by Ophus *et al. Nature Communications* 7:10719 (2016) [27]. Colin Ophus developed the idea for the experiment. I helped with the design of the diffraction grating and I provided the expertise and knowledge to manufacture the diffraction grating used for this experiment. I also assisted in the development of the theory for the experiment.

The ability to effectively engineer specific beam profiles opens the door on many advanced imaging techniques – specifically, enhanced phase contrast imaging. As opposed to
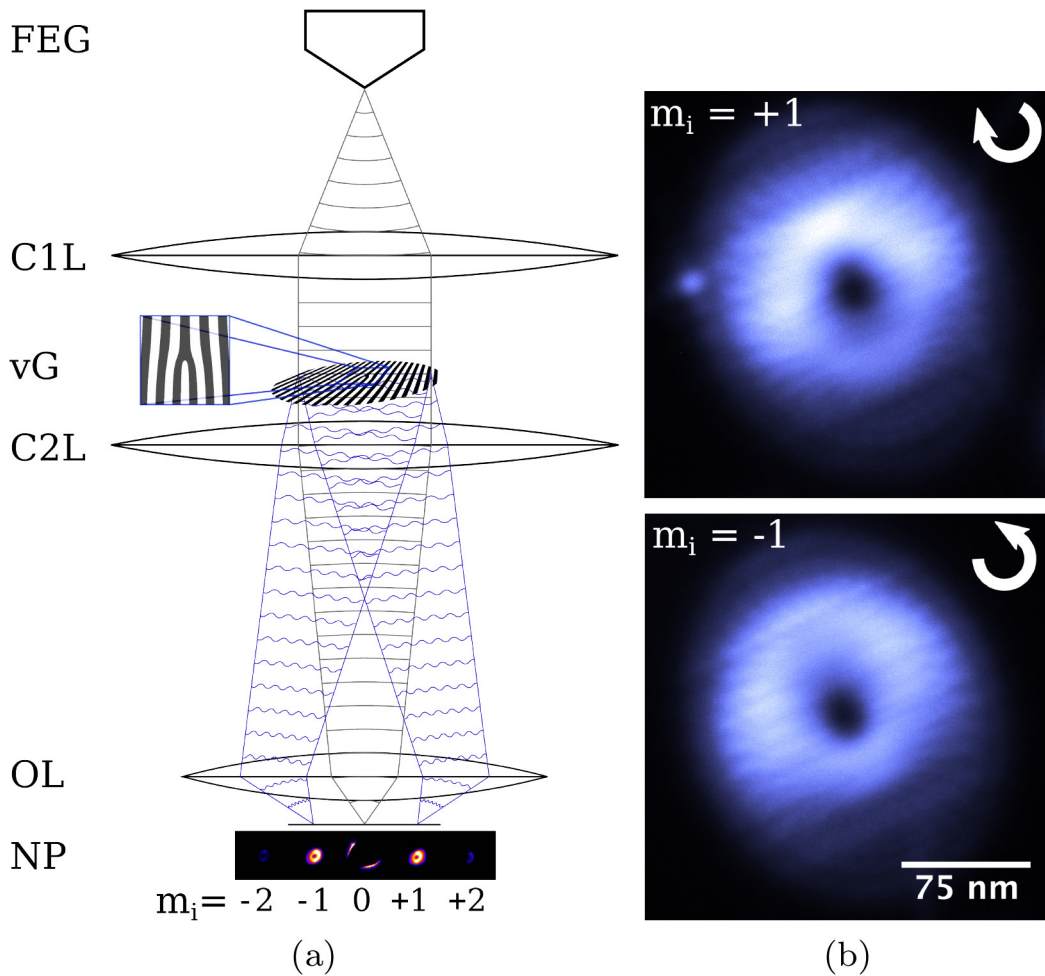
FIGURE 5.3: Optical setup for electron helical dichroism. (a) The vortex grating (vG) is placed in the second condenser aperture plane, producing separated probes in the sample plane where the nanoparticles are located. (b) Transmission electron micrograph of the first diffraction orders for the vortex beam used. Image source: [20]; reprinted with permission from the authors.

STEM, TEM is highly preferred by the biological community due to enhanced weak-phase imaging at low dose. However, the resolution of TEM is limited to the signal-to-noise ratio, which is a function of dose. Thus, biological samples have to be imaged with low dose TEM to achieve acceptable resolution while having good phase contrast [68, 69]. To image dose-

sensitive samples, the typical method is single-particle reconstruction utilizing cryo-electron microscopy. This requires many identically prepared particles that are well isolated, and is highly sensitive to the focal settings and requires complex reconstruction methods to produce usable results.

Within an STEM, image reconstruction is comparatively simpler, with the detectors typically integrating over a particular subregion of solid angle in reciprocal space. Most commonly, this includes annular dark field (ADF) imaging that gives incoherent contrast proportional to the projected thickness (and atomic mass) of the sample and bright field (BF) imaging, which is more sensitive to coherent image contrast and compares more to standard TEM [70]. Because the cross-section of scattering from a nucleus is small and proportional to the atomic number of the nucleus, ADF-STEM is relatively inefficient at producing atomic resolution images via high angle scattering. This is even more exacerbated with the light atoms common for biological samples, thus STEM is much more prevalent with inorganic hard materials and uncommon for imaging biological specimens.

There have been several proposed methods which circumvent this limitation with STEM. These all involve either segmented or pixelated detectors – instead of measuring the total intensity over some solid angle in reciprocal space, either a coarse image with up to dozens of segments or even a full-blown high pixel image is taken of the reciprocal space image. For instance, Dekkers and de Lang proposed utilizing a segmented detector and a probe corrector to enhance coherent phase-contrast imaging in STEM [71].

For this experiment, we utilize a pixelated detector to create a virtual detector – that is, we post-integrate over specific regions of the reciprocal plane to generate linear phase contrast. For the probe-forming aperture, we create a binary on-axis diffraction grating with no phase structure – that is, the grating will produce multiple copies of the incident beam separated in z, or focal value. This produces the illumination of the sample, and we match the pattern of illumination as the virtual detector. Thus we call this method

matched illumination and detector interferometry STEM, or MIDI-STEM. The overview of the experimental setup is shown in Figure 5.4.

This method works as follows: the grating is focused onto a sample, where much of the beam passes through without interacting, but some of the beam will interact with the phase structure of the sample. The primary measurable effect of this interaction is due to the linear phase of the sample local to the probe. This linear phase imparts a momentum on the beam proportional to the magnitude of the phase gradient. With this, in the reciprocal plane, there will ideally be two beams – a reduced intensity center beam with the phase structure given by the grating geometry, and a shifted copy of this beam. These two beams will interact, producing a series of interference patterns that allow for the precise determination of the local linear phase at the focal point of the beam. The grating is designed to be an on-axis diffraction grating with phase proportional to $|\vec{r}|^2$, creating multiple copies of the incident beam separated by their respective focal points. The shifted beam that interacts with the unshifted image of the grating will be a shifted copy of the zeroth order only. By designing the grating such that the phase difference between the unmilled area and the milled area (this is a binary grating) is precisely $\pi/4$ radians, the overlapping interference of the resulting beams will have maximum contrast. This phase depth correlates to about 10-12 nm in Si_3N_4 for 300 keV electrons.

Fabricating these gratings are challenging in that the effective pitch varies widely across the beam. Because these gratings are not off-axis gratings, there is no carrier vector $\vec{k}$ describing a reference wave. The pitch comes from binarizing the $|\vec{r}|^2$ phase term. This produces a pattern of concentric rings of various thicknesses such that the area of each ring is constant. Thus, as $\vec{r}$ increases, the thickness of the rings decreases. This means that the milling will require a wide range of feature sizes, and the grating should be as binary as possible. An SEM image of the grating produced for this experiment is shown in Figure 5.5, along with the theoretical charge transfer function.
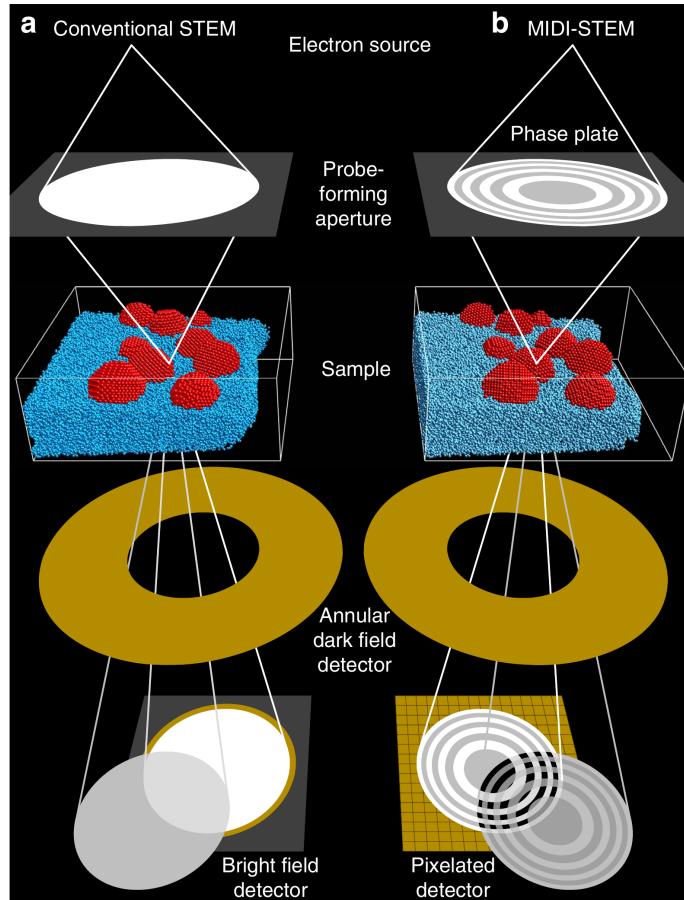
FIGURE 5.4: Comparison of conventional STEM and MIDI-STEM. Conventional STEM (a) consists of single pixel (single valued) ADF and BF detectors, whereas MIDI-STEM (b) utilizes a pixelated BF detector. Image source: [27], reprinted under Creative Commons Attribution 4.0 International License.

This experiment was successful at producing strong phase-contrast images at reduced dose. To see the full results, see Ophus *et al.* [27]. This use of STEM to generate phase contrast at low dose is highly dependent on the production quality of the diffraction grating. Much work was put into developing the technique to generate optimal gratings. In the end, the most effective method is to utilize the built-in shape tools of the FIB – using a series of circles with outer edges matching the edges of the grating rings, and alternate each circle between a regular mill and an exclusion zone. The advantage of this method is that the
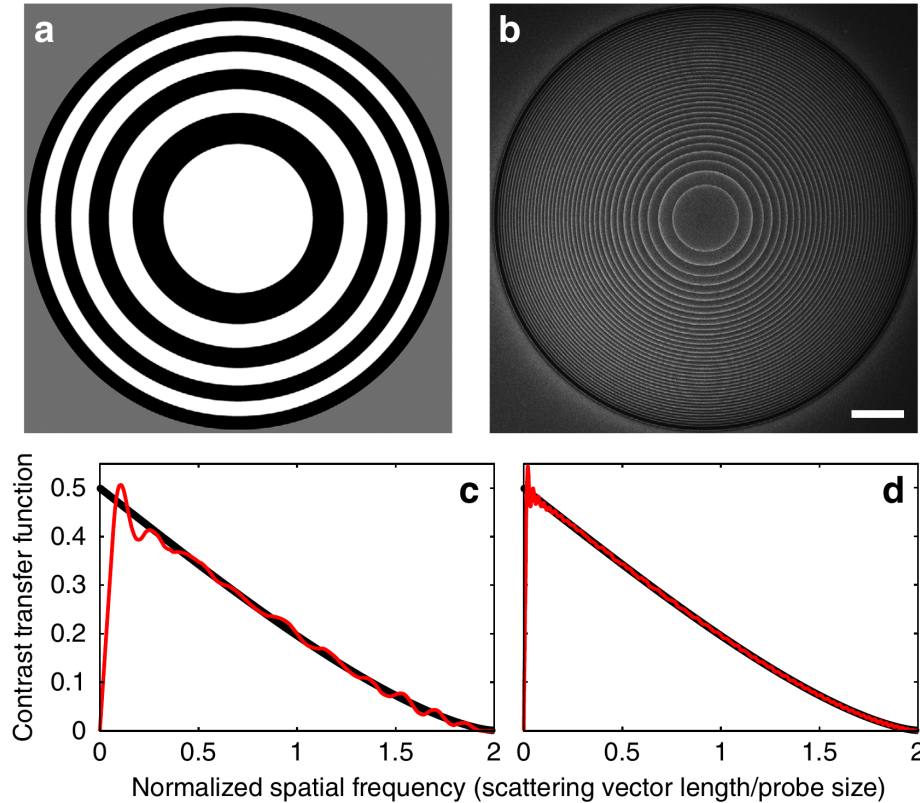
FIGURE 5.5: MIDI-STEM phase plates can be made with a varying number of rings, with more rings producing a more ideal contrast transfer function. A MIDI-STEM phase plate with only four rings (a) can produce a decent CTF (c), whereas in our experiment, we generated a MIDI-STEM plate with 20 rings (b), producing a highly ideal CTF (d). The black lines in (c-d) represent the CTF for an ideal phase-contrast STEM experiment. The scale bar is 5 μm. Image source: [27], reprinted under Creative Commons Attribution 4.0 International License.

milling pattern for the built-in circular tool function is azimuthally mill starting from the extreme radius and moving toward the center. By having the mill time per pixel be on the order of 100 μs and having many thousands of passes at 7.6 pA, the resulting fabrication should have smooth side walls and be milled mostly flat.

5.4 Counter-Rotating Beam

One often used method to measure the phase profile of a beam is to coherently interfere the beam with a reference wave, typically a plane or spherical wave. This produces an interference pattern that can be utilized to recover phase information. This is the basis for holography, and the reference wave can either be off-axis or coaxial. When the reference wave is coaxial to a vortex beam of topological charge m, the resulting interference pattern will contain m lobes. The position and shape of these lobes will change during propagation, but they will in general rotate by 180 degrees from one extreme of focus to the other – this is a result of the Gouy phase of the beam. The total phase shift due to the Gouy phase from $z = -\infty$ to $z = \infty$ is given by (see Equation 2.15)

$$\Phi_{\mathrm{G}} = \pi(|m| + 2p + 1). \tag{5.3}$$

Note that a plane wave is well approximated as a spread out Laguerre Gaussian beam with $m = 0$ and $p = 0$. Thus, the difference in Gouy phase accumulated between a vortex beam of charge m and a coaxial plane wave is $\Delta\Phi_{\mathrm{G}} = |m|\pi$. The total phase accumulated about the azimuth of a vortex beam of charge m is $2\pi m$. Clearly the Gouy phase difference amounts to half of the rotational phase of the vortex beam. The result is that as the vortex beam and the coaxial reference wave go through focus, the resulting interference pattern will rotate by 180 degrees, regardless of the value of m.

Because of this, some interesting beam profiles can be developed. One such profile I developed is a specific combination of fourteen LG modes, specifically,

$$\begin{aligned} \Psi_A = {}& 11(LG_0^6 + LG_0^9 + LG_0^{12} + LG_0^{15} + LG_0^{18} + LG_0^{21}) \\ & + 10(LG_0^{-60} + LG_0^{-63} + LG_0^{-66} + LG_0^{-69} + LG_0^{-72} + LG_0^{-75} + LG_0^{-78} + LG_0^{-81}). \end{aligned} \tag{5.4}$$

This produces a beam that consists of two mostly non-interacting sub-beams. Specifically, the positive m value modes are small enough to not overlap much with the negative m value modes. The result is that the inner positive m modes rotate clockwise through focus,

whereas the negative m modes rotate counter clockwise. A plot of the complex wave-function for this beam is shown in Figure 5.6, along with an image of the grating fabricated with this pattern shown in Figure 5.8. A focal series of the simulated propagation vs. actual data is sown in Figure 5.7, demonstrating the primary quality of this beam – that the inner and outer sections rotate in opposite directions.

FIGURE 5.6: Representation of the complex amplitude for the beam given in Equation 5.4. This beam has an inner and an outer portion that rotate in opposite directions as the beam propagates through focus.

At this point it is unclear what applications might arise from this type of a beam, but it is important to be able to demonstrate and understand the capabilities of electron beams and the gratings utilized in shaping them.
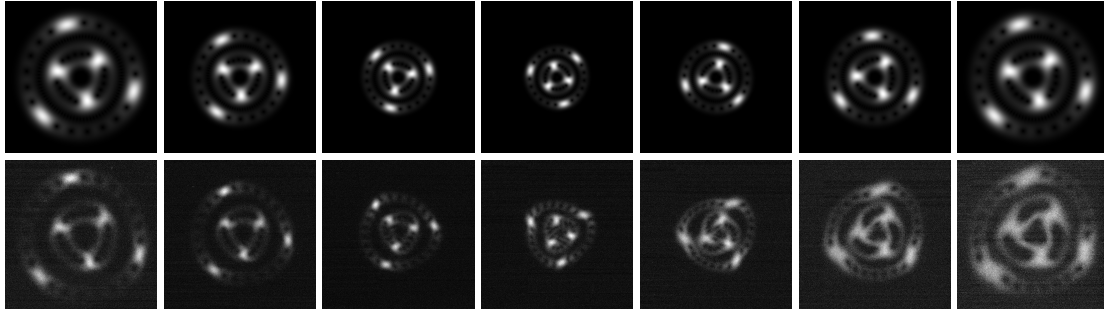
FIGURE 5.7: Simulated (top row) vs. actual data (bottom row) for the beam given in Equation 5.4. Note that there were significant aberrations in the microscope during image acquisition, resulting in a distorted beam, which is more pronounced near focus. Ignoring the distortions due to aberrations (making the beam non-circular), note the qualitative differences in the beam image on either extreme of focus – this is caused because the grating was not corrected according to the earlier sections on making ideal beams. The grating used to take this data is shown in Figure 5.8. The actual defocus values between images is somewhat arbitrary, but the simulation is symmetric about focus, with focus the central image.

5.5   Highly Twisted Electron Beams

This section contains unpublished work performed in collaboration with Andrew Forbes from the University of the Witwatersrand, South Africa. I designed the diffraction gratings and collected the data, as well as performed some of the analysis. Jason Webster analyzed much of the data and developed the theory for the work.

Another class of beams which utilize the Gouy phase in specific ways are those for which the intensity pattern rotates multiple times through focus. This can be broadly achieved in two ways – using Laguerre Gaussian beams or using Bessel beams.

Using Laguerre beams, we utilize the p modes in Equation 2.15 to create added Gouy phase. Because the intensity pattern is changing during propagation (apart from scale), rotating intensity patterns must be a superposition of at least two modes. We want to the intensity pattern to only have an added rotation with no other complicated sources of z dependence. Because of this, we will work with a superposition of only two Laguerre

HV	HFW	mag ⊞	WD	tilt	det	curr	bias		10 μm
2.00 kV	41.4 μm	5 000 x	4.2 mm	52 °	TLD	1.4 nA	0 V		
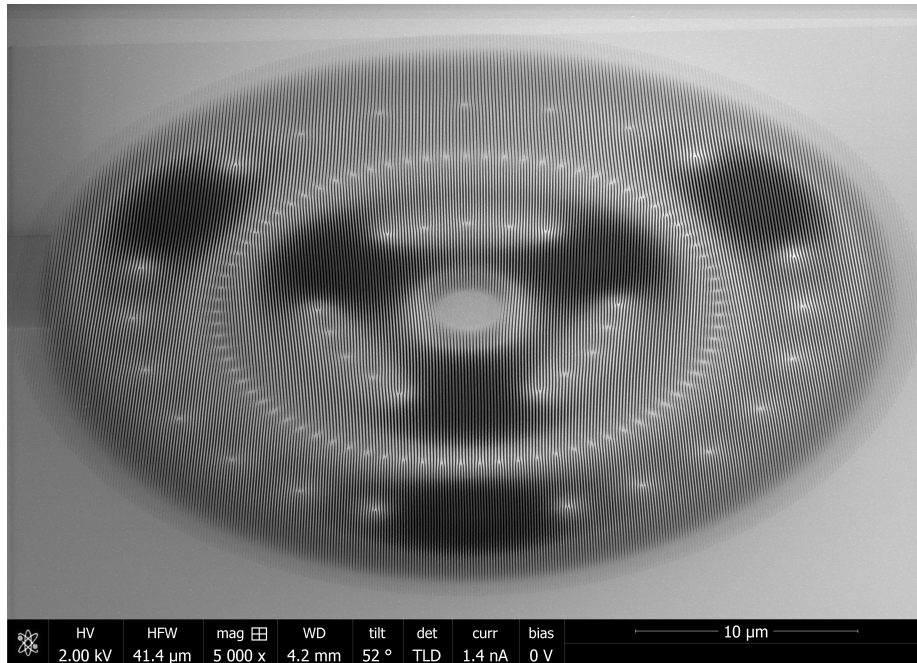
FIGURE 5.8: SEM scan of a 40 micron grating designed to produce Equation 5.4. This scan was taken in the FIB just after milling the grating. The electron source is imaging the sample 52 degrees from normal due to the membrane being aligned for FIB milling.

Gaussian modes. Note that Equation 2.15 is of the form $\psi(z) = G_\psi \tan^{-1}(f(z))$, with $G_\psi = |m| + 2p + 1$ the Gouy prefactor. The difference of the Gouy prefactor of two modes is proportional to the number of times the intensity pattern will rotate for that superposition. For instance, a superposition defined as

$$\Psi_S = LG_0^{-1} + LG_{20}^2 \tag{5.5}$$

will have a total accumulated difference in Gouy phase between each mode of 42π radians through focus. This correlates to the intensity pattern rotating multiple times as the focal value sweeps from $-\infty$ to $+\infty$. The complex amplitude for this beam is shown in Figure 5.9.

In a TEM, we are highly limited in how much the probes from a grating can be defocused due to the limited beam separation. Because of this, we were unable to measure how many times the intensity pattern rotated, but we did observe multiple rotations over the course
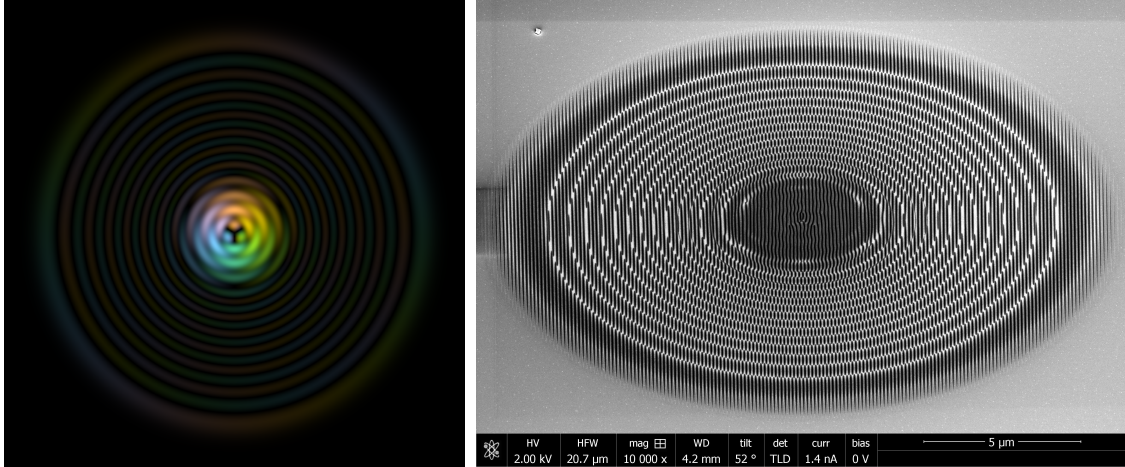
FIGURE 5.9: Complex amplitude of the beam given in Equation 5.5 (left), with the FIB milled hologram (right). This beam rotates multiple times through focus.

of a focal series. As seen in Figure 5.10, the rotation is mostly linear over a large range of defocus values. As with a mode which rotates by only 180 degrees through focus, the rate of rotation should be proportional to $\tan^{-1}(z)$, but in this case the given focal series is over a small enough range as to be well approximated as linear.

Another method that can produce an intensity pattern that rotates linearly during propagation is by utilizing superimposed Bessel beams. This is because the Bessel function is a limiting case of Laguerre polynomials. Specifically,

$$J_m(x) = \lim_{n \to \infty} \left(\frac{x}{2n} \right)^m L_n^m \left(n \left(\frac{x}{2n} \right)^2 \right), \tag{5.6}$$

with $J_m(x)$ the Bessel function of order m, and $L_n^m(x)$ the associated Laguerre polynomial. Note that the wave equation can be solved utilizing Bessel functions in polar coordinates similar to how plane waves are utilized in Cartesian coordinates. Like plane-wave solutions, Bessel function solutions are non-normalizable – they are however solutions to the full wave equation and not the paraxial approximation. Because of this, they are not fully realizable in any real world experiment. However, as with plane-waves, they can be well approximated. Plane waves are generated by an ideal point source infinitely distant – thus the Fourier
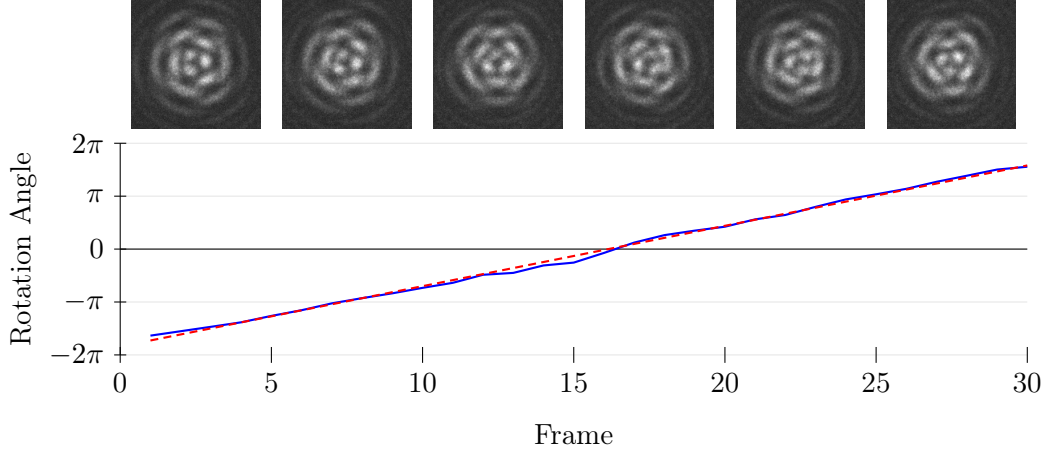
FIGURE 5.10: Rotation angle of the intensity pattern for the beam defined in Equation 5.5. Thirty images were taken of the beam through focus, each with a constant defocus of about 100 nm. The top row shows the central portion of the beam for the first six frames. The bottom graphs shows the measured rotation angle (solid blue) vs. the frame, as well as a linear fit (dashed red). The defocus value between each frame is constant, thus this shows a linear rotation through focus.

transform of a plane-wave is a delta function. To generate a Bessel wave, the source is a delta-ring at infinite distance.

In collaboration with Andrew Forbes and Jason Webster, we ran an experiment to generate a beam that not only rotated multiple times through focus, but had the rate of rotation change in regular intervals. This "angularly accelerating" beam follows closely with the work done by Schulze $et\ al.$ [72], where superpositions of Bessel modes were generated in light fields.

Bessel beams as a solution to the wave equation are given as

$$\psi(r, \phi, z) = \mathcal{J}_l^{k_r}(\vec{r}) = J_l(k_r r)e^{il\phi}e^{ik_z z}, \qquad (5.7)$$

where l is the order of the beam (equivalent to m for vortex beams), and $k^2 = k_r^2 + k_z^2$ with k the wave-number of the beam. For the Bessel beams that we work with, $k_r \ll k_z$, and k_z can be assumed to be constant. By creating a superposition of two modes with differing k_r parameters, such as $\mathcal{J}_1^{k_{r1}} + \mathcal{J}_{-1}^{k_{r2}}$, the resulting intensity pattern will rotate multiple times

during propagation. This can be seen in Figure 5.12a. To produce a beam which accelerates azimuthally during propagation, we use the following superposition

$$\psi(\vec{r}) = \left[\mathcal{J}_1^{k_{r_1}}(\vec{r}) + D\mathcal{J}_{-1}^{k_{r_1}}(\vec{r}) \right] + \left[\mathcal{J}_1^{k_{r_2}}(\vec{r}) + D\mathcal{J}_{-1}^{k_{r_2}}(\vec{r}) \right], \tag{5.8}$$

where the anisotropic parameter D determines the amount of acceleration, with $0 \leq D \leq 1$. Zero acceleration corresponds to $D = 0$, and 'infinite' acceleration corresponds to $D = 1$. For nonzero D, the phase about the azimuth is a non-linear function. This non-linearity is what gives rise to the apparent acceleration of portions of the beam during propagation, as seen in Figure 5.12. To generate the beams, the Fourier transform of the desired beams were encoded into an electron diffraction grating. Note that it is not possible to mill a "delta ring" onto a grating, thus a compromise was made to widen the rings and produce approximate Bessel beams, as seen in Figure 5.11.
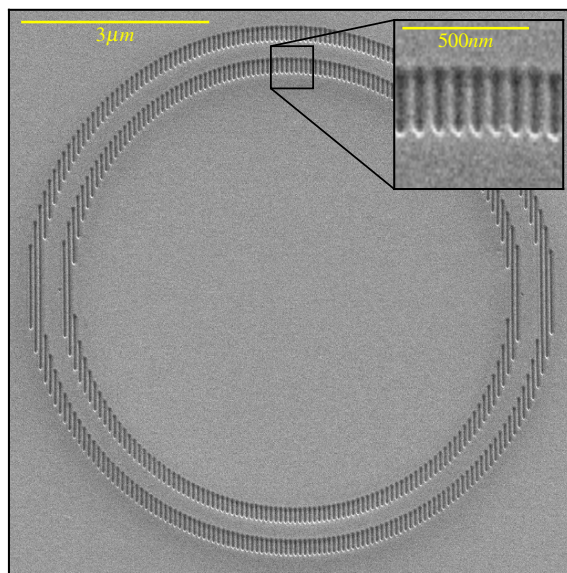
FIGURE 5.11: Electron diffraction grating used to produce Bessel beam superpositions. Each ring encodes a single Bessel function. The width of the ring is a trade-off between intensity in the diffracted beam and purity of the Bessel mode created.

Four separate holograms were fabricated with varying levels of angular acceleration en-

coded, ranging from no acceleration $D = 0$, to $D = 0.1584$, $D = 0.325$, and $D = 0.510$. For each hologram, a focal series of more than 80 images was taken over a propagation distance of more than 10 microns. This allowed us to observe two acceleration cycles during the propagation. The control of the acceleration profile requires precise control of the mill depth of the grating. This level of control is not easily achievable within the FIB used to fabricate the gratings, and thus the measured D parameter from the focal series differs significantly from the value used to generate the holograms. However, the rotation and angular acceleration of the beams is clearly demonstrated. The angular velocity and acceleration for each grating is shown in Figure 5.13.

Because these beams are accelerating in some sense about the azimuth during propagation combined with the mass and charge of the electrons, we wanted to verify that there were no radiation events happening during propagation caused by this acceleration. To do this, we performed an electron energy loss spectrum (EELS) on the beam, looking for signals near 1 eV. Also, to maximize the potential for radiation events to occur, we generated a hologram with $D = 1$ to have 'infinite' acceleration. The EELS data is shown in Figure 5.14. The imaging conditions during the EELS acquisition were identical to the conditions used to collect the rest of the data. The EELS instrument was spread with a sensitivity of 0.05 eV per pixel, with at 2048 pixel width. The EELS signal for each hologram was analyzed for any signal, with all being consistent for no energy loss.
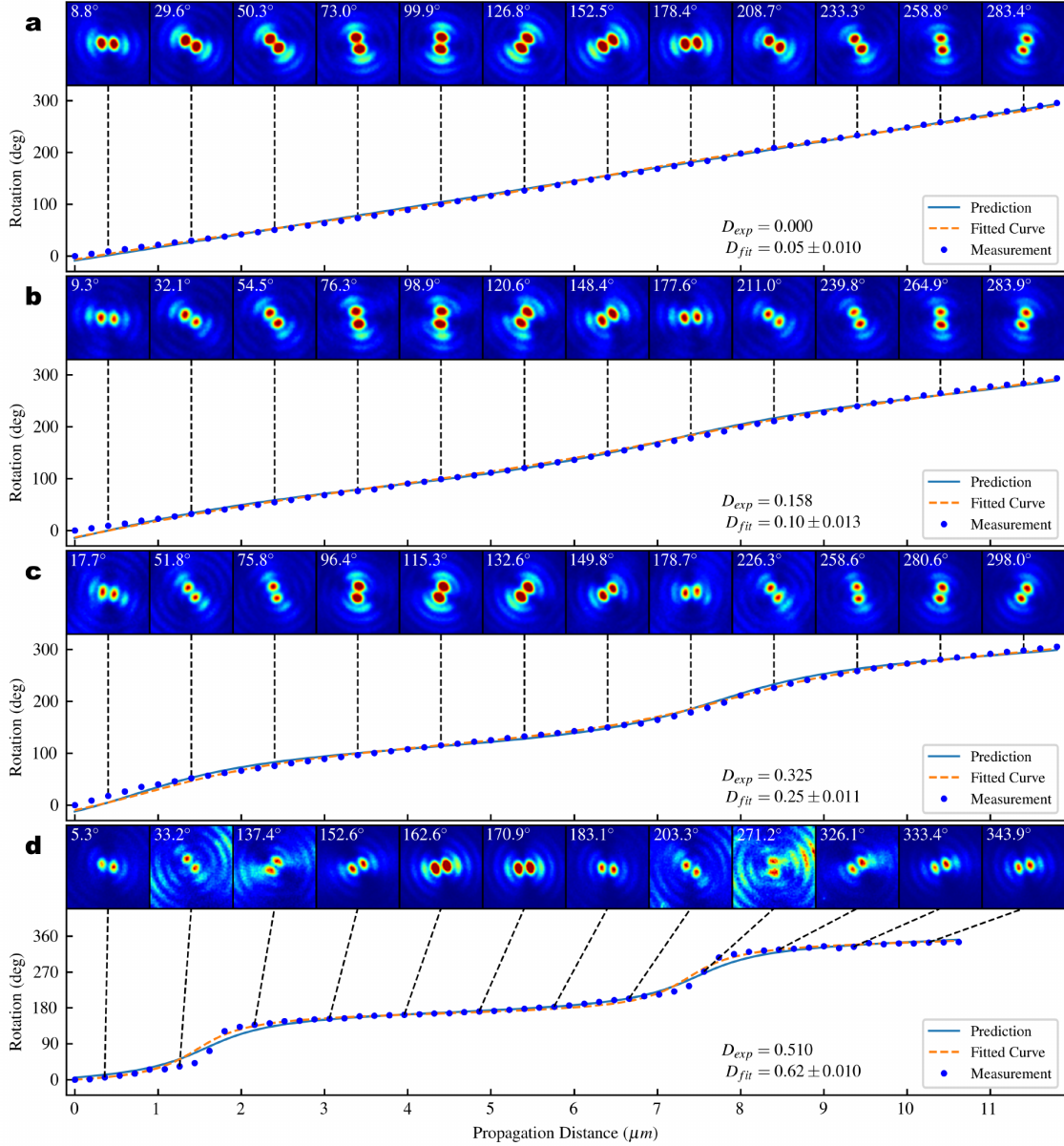
FIGURE 5.12: Rotation and angular acceleration associated with Bessel beam superpositions. Four different holograms were generated, with $D_{\exp}$ the value of the anisotropic parameter used to generate the hologram, while D_{fit} was calculated from the data. The theoretical (solid teal), fitted (dashed orange) and measured rotation (blue dots) are plotted together for comparison for each of the four gratings of (a) $D_{\exp} = 0$, (b) $D_{\exp} = 0.158$, (c) $D_{\exp} = 0.325$, (d) $D_{\exp} = 0.510$. The insets show the electron beam intensity pattern for various focal distances.
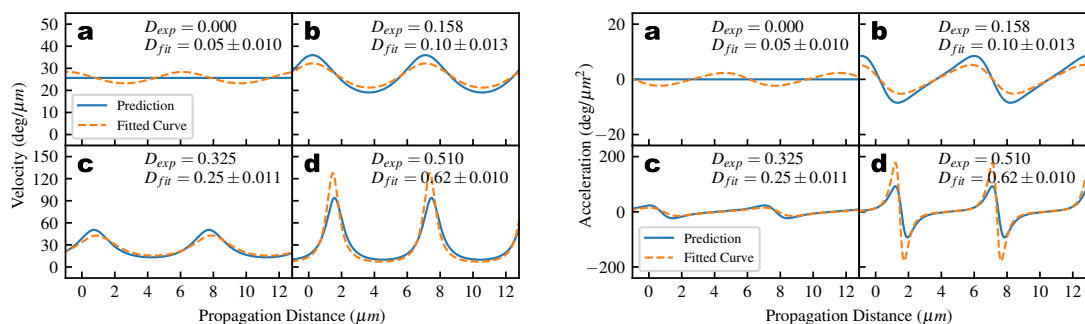
FIGURE 5.13: For the beams shown in Figure 5.12, the measured velocity (left) and acceleration (top) during propagation. The anisotropic parameter for each is (a) $D_{\text{exp}} = 0$, (b) $D_{\text{exp}} = 0.158$, (c) $D_{\text{exp}} = 0.325$, and (d) $D_{\text{exp}} = 0.510$. The solid curve is the theoretical result based on the value of D encoded onto the diffraction grating (D_{exp}), while the dashed orange curve is from the fit to the focal series (D_{fit}).
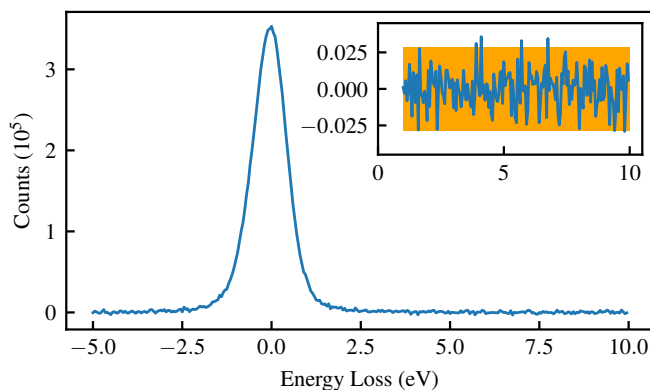
FIGURE 5.14: The EELS data for a beam generated with $D = 1$ for 'infinite acceleration'. Any energy loss due to radiation should show as a peak at the corresponding energy loss value. The inset shows the data with the zero-loss peak subtracted, with the orange band giving the 95% noise bounds. This data is consistent with zero radiative energy loss during propagation.

CHAPTER VI

SLM ENCODED LASER HOLOGRAMS

6.1 Electromagnetic Diffraction Gratings

The deflection of atoms from a set of standing resonant electromagnetic waves is considered. This is of interest for the purpose of potentially creating atom interferometers or other optical-atom devices. Another application is for atom isotope separation.

Let's begin with an overview of the system that will be analyzed. A beam of atoms, described by the complex function $\Psi_a(\vec{r})$ flows from the negative z-axis toward the origin. It will be assumed initially that the beam has a Gaussian profile. At the origin, a confluence of laser beams interacts to create a standing wave of a particular shape. All of these lasers are in the x-y plane. The atom beam interacts with the EM field in the vicinity of the origin, with interaction time t_i. The arrangement of lasers and the creation of the beam of atoms are beyond the scope of this assessment, and it will be assumed that the lasers and atom beam can be arranged to suit the needs of this model.

For a conceptual overview of the model, the parameters of importance are: t_i – the interaction time of each atom with the EM field, Ω – the rate of absorption and stimulated emission, γ – the rate of spontaneous emission, and ω – the frequency of the EM field. Throughout this model, it will be assumed that the atoms are two-level atoms with a transition frequency ω_{mn}. Also, because the intensity of the laser is sufficiently large, $\Omega \gg \gamma$.

Now consider the case of a single laser that is uniform in intensity over the relevant x and y ranges of the atom field, and is constant magnitude for $|z| < L$ and zero outside of this range. This is essentially a sheet of photons. With only one propagating laser, absorption followed by stimulated emission back into the laser field results in no net transfer of momentum. Only absorption followed by spontaneous emission transfers momentum, and

75

on average spontaneous emission transfers no momentum – thus only the absorption transfers momentum, and each absorption-spontaneous-decay event transfers $\hbar k$ of momentum into the atom.

With two or more applied laser fields however, absorption can be followed by stimulated emission into another laser mode, resulting in net transfer of momentum. If the stimulated emission rate is large compared to the spontaneous emission rate, then the spontaneous emission can be ignored, which will be done throughout this project.

Throughout this analysis the translation and internal states of the atoms are modeled quantum mechanically, while the EM field is treated classically. The internal states of the atom are considered as a two-level system.

The Hamiltonian for an atom interacting with a classical EM field is

$$H = \frac{P^2}{2M} + H_0 - \vec{\mu} \cdot \vec{E}(\vec{r},\, t) \tag{6.1}$$

where P is the momentum of the atom, $\vec{r}$ is the x-y position of the atom, H_0 is the Hamiltonian for internal states of the bare atom, and $\vec{\mu}$ is the dipole moment operator. Initially, the atoms are traveling in the positive z direction, enter the region of the EM field at coordinate $z = -L$, and leaves the EM field at $z = L$.

6.2   Atom Beam

Instead of treating the atom beam as an infinite set of plane-waves, I will assume that the atom beam satisfies the conceptual requirement of a 'beam' – that is, that it has a well defined optical axis and satisfies the paraxial wave equation. With this, the beam has a propagation direction and two quantum numbers representing the modes in the plane perpendicular to the propagation vector. For instance, if we wish to use the Bessel beam modes as the mode expansion for the atom beam, the two quantum numbers are $|k_r\rangle$ and $|l\rangle$, where k_r is a continuous parameter specifying the radial period, and l is an integer parameter specifying the orbital angular momentum value of the beam.

76

These beams have raising and lowering operators for each quantum number, and it is these operators that we desire to recreate in the diffraction grating, so that a particular diffracted order of the grating will have the desired beam mode. For Bessel beams, the raising and lowering operators for the OAM quantum number are $e^{\pm i\theta}$, where θ is the polar angle.

Note that for a mode expansion using something other than plane waves results in extra terms in the defining Hamiltonian that are dependent on the quantum numbers of the beam mode. The energy associated with the beam modes is typically very small and to a good approximation the modes are degenerate, but they are still needed in the definition of the Hamiltonian, which would now have the form

$$H = \frac{p^2}{2M} + H_B + H_0 - \vec{\mu} \cdot \vec{E}(\vec{r}, t), \tag{6.2}$$

where H_B is the Hamiltonian for the beam modes.

6.3 Diffraction Grating

To create the proper diffraction grating, the interference between laser modes must be suitably established as an interaction region for the atom beam. For instance, if we wish to create a Bessel beam of a particular mode from a Gaussian input beam, we can create the interference of a Gaussian laser beam with the appropriate Bessel laser beam, both of frequency ω, and arranged such that the interaction region is well defined and satisfies the simplifications stated earlier in that the interaction region is from $-L < z < L$, and the intensity in the x-y plane is more or less constant.

The interference of the two laser modes can be expressed as

$$E(\vec{r}, t) = \vec{E_0} \cos\left(\vec{k} \cdot \vec{r} + \phi(\vec{r}) + \phi'(\vec{r})\right) \cos(\omega t), \tag{6.3}$$

where $\phi(\vec{r})$ is the phase structure of one of the beams, and $\phi'(\vec{r})$ is the phase structure of the other. Assuming that one of the reference beams will always be well approximated as a

plane-wave, which has $\phi(\vec{r}) = 0$, we can use

$$E(\vec{r}, t) = \vec{E}_0 \cos\left(\vec{k} \cdot \vec{r} + \phi(\vec{r})\right) \cos(\omega t) \tag{6.4}$$

$$= \frac{\vec{E}_0}{2} \left(e^{i\phi(\vec{r})} e^{i\vec{k} \cdot \vec{x}} + e^{-i\phi(\vec{r})} e^{-i\vec{k} \cdot \vec{x}}\right) \cos(\omega t) \tag{6.5}$$

For the Hamiltonian defined earlier, proper application of Schrödinger's equation will allow the determination of the probability density $W(p_{\vec{k}})$ for momentum p in the $\vec{k}$ direction. Momentum density is related to displacement in the $\vec{k}$ direction, for large z, via $P(|\vec{r}|) = \frac{p_z}{z} W(p_z \frac{|\vec{k}|}{z})$.

6.4 Schrödinger's Equation

As I am modeling the atom as a two level system, the states can be conveniently labeled as $\{|+\rangle, |-\rangle\}$. Also, the Hamiltonian from Equation 6.1 can be split into an interaction Hamiltonian H_I and an unperturbed Hamiltonian H', with $H_I = -\vec{\mu} \cdot \vec{E}(\vec{r}, t)$, and $H' = \frac{P^2}{2M} + H_0 + H_B$. The eigenvectors for H' are $|n\rangle |\vec{p}\rangle |c\rangle |l\rangle$, where $|n\rangle$ are the eigenvectors for H_0, $|\vec{p}\rangle$ are the eigenvectors for the momentum operator (the momentum along the optical axis for each beam), and $|c, l\rangle$ are the eigenvectors for the beam mode. The eigenvalues for H' are $\epsilon_n(\vec{p}) = \frac{|\vec{p}|^2}{2M} + E_n$, where E_n is the internal energy of state n and I have neglected the energy associated with the beam modes, which is negligible except for extreme cases.

Before interaction with the EM field, the atoms in the beam (all the atoms are assumed to be in the same state) are of the form

$$|\psi\rangle = \sum_{n,c,l} \int \mathrm{d}\vec{p}\, \phi_{n,c,l}(\vec{p}) \, |n, \vec{p}, c, l\rangle, \tag{6.6}$$

where $\phi_{n,c,l}(\vec{p})$ is the complex amplitude of each mode, and if one or both of the beam quantum numbers c and l are continuous, the sum represents an integral. Applying the

Schrödinger equation,

$$i\hbar\partial_t \left|\psi\right\rangle = H \left|\psi\right\rangle \tag{6.7}$$

$$\left\langle n,\, \vec{p}, c, l \right| i\hbar\partial_t \left|\psi\right\rangle = \left\langle n,\, \vec{p}, c, l \right| i\hbar\partial_t \sum_{m,u,v} \int \mathrm{d}\vec{p}'\, \phi_{m,u,v}(\vec{p}')\left|m,\, \vec{p}', u, v\right\rangle \tag{6.8}$$

$$i\hbar\partial_t \phi_{n,c,l}(\vec{p}) = \sum_{m,u,v} \int \mathrm{d}\vec{p}' \left\langle n,\, \vec{p}, c, l \right| H \left|m,\, \vec{p}', u, v\right\rangle \phi_{m,u,v}(\vec{p}'). \tag{6.9}$$

6.5   Grating Specifics

To evaluate $\left\langle n,\, \vec{p}, c, l \right| H \left|m,\, \vec{p}', u, v\right\rangle$ it becomes necessary to specify the shape of the grating and the beam modal expansion that we will be using. By setting

$$\vec{E}(\vec{r},\, t) = \frac{\vec{E}_0}{2}\left(\Theta^\dagger e^{i\vec{k}\cdot\vec{r}} + \Theta e^{-i\vec{k}\cdot\vec{r}}\right), \tag{6.10}$$

where Θ is the azimuthal mode raising operator for Bessel beam modes, and sticking with Bessel modes (note that $\Theta = e^{i\theta}$), the right hand side of Equation 6.9 becomes

$$\sum_{m,u,v} \int \mathrm{d}\vec{p}\left\langle n,\, \vec{p}, c, l \right| H \left|m,\, \vec{p}', u, v\right\rangle \phi_{m,u,v}(\vec{p}') =$$

$$\sum_{m,u,v} \int \mathrm{d}\vec{p}\left\langle n,\, \vec{p}, c, l \right| H' \left|m,\, \vec{p}', u, v\right\rangle \phi_{m,u,v}(\vec{p}') + \left\langle n,\, \vec{p}, c, l \right| H_I \left|m,\, \vec{p}', u, v\right\rangle \phi_{m,u,v}(\vec{p}')$$

$$\tag{6.11}$$

$$= \epsilon_n(\vec{p})\phi_{n,c,l}(\vec{p}) + \sum_m \cos(\omega t) \left\langle n\right| \vec{\mu}\cdot\frac{\vec{E}_0}{2} \left|m\right\rangle \left(\phi_{n,c,l-1}(\vec{p}-\hbar\vec{k}) + \phi_{n,c,l+1}(\vec{p}+\hbar\vec{k})\right). \tag{6.12}$$

By setting $g_{nm} = \left\langle n\right| \vec{\mu}\cdot\vec{E}_0 \left|m\right\rangle/2$, Equation 6.9 becomes

$$i\hbar\partial_t\phi_{n,c,l}(\vec{p}) = \epsilon_n(\vec{p})\phi_{n,c,l}(\vec{p}) - \cos(\omega t)\sum_m g_{nm}\left(\phi_{n,c,l-1}(\vec{p}-\hbar\vec{k}) + \phi_{n,c,l+1}(\vec{p}+\hbar\vec{k})\right). \tag{6.13}$$

This equation shows that a change of the internal state of the atom is associated with the transfer of $\pm\hbar k$ linear momentum and ± 1 unit of orbital angular momentum. Note that $g_{nn} = 0$.

6.6 Interaction Picture Approximations

Going to the interaction picture, set

$$\phi_{n,c,l}(\vec{p}) = C_{n,c,l}(\vec{p})e^{-i\epsilon_n(\vec{p})\frac{t}{\hbar}}, \tag{6.14}$$

where $\epsilon_n(\vec{p})$ are the eigenvalues of H'. Utilizing Equation 6.13 gives the differential equation on the $C_{n,c,l}(\vec{p})$'s as

$$i\hbar\partial_t C_{n,c,l}(\vec{p}) = -\cos(\omega t)\sum_m g_{nm}\left(C_{m,c,l-1}(\vec{p}-\hbar\vec{k})e^{-i\left(-\frac{\hbar\vec{p}\cdot\vec{k}}{M}+\frac{\hbar\omega^2}{2Mc^2}+\omega_{mn}\right)t}+\right.$$
$$\left.C_{m,c,l+1}(\vec{p}+\hbar\vec{k})e^{-i\left(\frac{\hbar\vec{p}\cdot\vec{k}}{M}+\frac{\hbar\omega^2}{2Mc^2}+\omega_{mn}\right)t}\right), \tag{6.15}$$

where $\omega_{mn} = (E_n - E_m)/\hbar$

At this point several approximations must be made – but first, let us take a look at the physical concepts involved in these equations. For the two level atom with resonant frequency ω_{mn}, absorption of a photon will increase the internal energy of the atom by $\hbar\omega_{mn}$ while the momentum transferred is $\hbar\omega/c$. Thus the kinetic energy increase is $(\hbar\omega/c)^2/(2M) = \hbar\delta$, and energy conservation requires that $\hbar\omega = \hbar\omega_{mn} + \hbar\delta$. Thus $\hbar\omega^2/(2Mc^2)$ is the frequency shift from resonance due to the change in kinetic energy of the atom. The therm $\hbar\vec{p}\cdot\vec{k}/M$ is the velocity dependent frequency shift (Doppler shift). Under the assumption of short interaction time, the broadening of the resonant frequency ω_{mn} is large compared to any shift due to kinetic energy or Doppler shifts, and these terms can be ignored. Further, letting $\omega = \omega_{mn}$, Equation 6.15 becomes

$$i\hbar\partial_t C_{n,c,l}(\vec{p}) \approx -\frac{1}{2}\left(e^{i\omega t}+e^{-i\omega t}\right)g_{nm}\left(C_{m,c,l-1}(\vec{p}-\hbar\vec{k})e^{-i\omega t}+C_{m,c,l+1}(\vec{p}+\hbar\vec{k})e^{-i\omega t}\right) \tag{6.16}$$

Finally, by utilizing the rotating wave approximation and neglecting the $e^{-2i\omega t}$ terms, we

are left with

$$\dot{C}_{+,c,l}(\vec{p}) = \frac{i\Omega}{2}\left(C_{-,c,l-1}(\vec{p}-\hbar\vec{k}) + C_{-,c,l+1}(\vec{p}+\hbar\vec{k})\right) \tag{6.17}$$

$$\dot{C}_{-,c,l}(\vec{p}) = \frac{i\Omega}{2}\left(C_{+,c,l-1}(\vec{p}-\hbar\vec{k}) + C_{+,c,l+1}(\vec{p}+\hbar\vec{k})\right) \tag{6.18}$$

where $\Omega = \langle -|\,\vec{\mu}\cdot\vec{E}_0\,|+\rangle\,/\hbar$. By adding and subtracting the above equations, two new equations are formed:

$$\dot{C}_{+,c,l}(\vec{p}) + \dot{C}_{-,c,l}(\vec{p}) = \frac{i\Omega}{2}\left(C_{+,c,l-1}(\vec{p}-\hbar\vec{k})\right.$$
$$\left. + \; C_{-,c,l-1}(\vec{p}-\hbar\vec{k}) + C_{+,c,l+1}(\vec{p}+\hbar\vec{k}) + C_{-,c,l+1}(\vec{p}+\hbar\vec{k})\right) \tag{6.19}$$

$$\dot{C}_{+,c,l}(\vec{p}) - \dot{C}_{-,c,l}(\vec{p}) = \frac{i\Omega}{2}\left(C_{+,c,l-1}(\vec{p}-\hbar\vec{k})\right.$$
$$\left. - \; C_{-,c,l-1}(\vec{p}-\hbar\vec{k}) + C_{+,c,l+1}(\vec{p}+\hbar\vec{k}) - C_{-,c,l+1}(\vec{p}+\hbar\vec{k})\right) \tag{6.20}$$

By setting

$$D_{+,c,l}(\vec{p}) = \frac{1}{\sqrt{2}}\left(C_{+,c,l}(\vec{p}) + C_{-,c,l}(\vec{p})\right) \tag{6.21}$$

$$D_{-,c,l}(\vec{p}) = \frac{1}{\sqrt{2}}\left(C_{+,c,l}(\vec{p}) - C_{-,c,l}(\vec{p})\right), \tag{6.22}$$

the equations uncouple to

$$\dot{D}_{+,c,l}(\vec{p}) = \frac{i\Omega}{2}\left(D_{+,c,l-1}(\vec{p}-\hbar\vec{k}) + D_{+,c,l+1}(\vec{p}+\hbar\vec{k})\right) \tag{6.23}$$

$$\dot{D}_{-,c,l}(\vec{p}) = -\frac{i\Omega}{2}\left(D_{-,c,l-1}(\vec{p}-\hbar\vec{k}) + D_{-,c,l+1}(\vec{p}+\hbar\vec{k})\right) \tag{6.24}$$

Remember that the $C_{\pm}$ are the state coefficients in the interaction picture. At this point, I will start ignoring the c quantum number. I may consider its effects at some later point.

6.7   State Coefficients

Solving these equations using the trial solution

$$D_{\pm,l}(\vec{p}) = \frac{1}{\sqrt{2\pi}}e^{i\vec{r}\cdot\vec{p}\pm i\alpha t\pm il\theta_p} \tag{6.25}$$

gives

$$iae^{\frac{i}{\hbar}\vec{r}\cdot\vec{p}\pm i\alpha t\pm il\theta_p} = \frac{i\Omega}{2}\left(e^{\frac{i}{\hbar}\vec{r}\cdot\vec{p}\pm i\alpha t\pm il\theta_p}e^{-i\vec{r}\cdot\vec{k}\mp i\theta_p} + e^{\frac{i}{\hbar}\vec{r}\cdot\vec{p}\pm i\alpha t\pm il\theta_p}e^{i\vec{r}\cdot\vec{k}\pm i\theta_p}\right) \tag{6.26}$$

$$\alpha(\vec{r}) = \Omega\cos\left(\vec{r}\cdot\vec{k} + \theta_p\right) \tag{6.27}$$

This is a dispersion relation in momentum space. Since any value of $\vec{r}$ gives a solution, the general form is

$$D_{\pm,l}(\vec{p}) = \frac{1}{\sqrt{2\pi}}\int_{-\infty}^{\infty}\mathrm{d}\vec{r}\,a_{\pm}(\vec{r})e^{i\vec{r}\cdot\vec{p}\pm i\alpha(\vec{r})t\pm il\theta_p}. \tag{6.28}$$

Note that l is the azimuthal quantum number of the atom beam before interacting with the electric field, which I will assume is $l = 0$ from here on. At $t = 0$, with $l = 0$, Equation 6.28 gives a simple Fourier transform between $a_{\pm}(\vec{r})$ and $D_{\pm,0}^0(\vec{p}) = D_{\pm,l=0}(\vec{p}, t = 0)$. This Fourier transform can be inverted as

$$a_{\pm}(\vec{r}) = \frac{1}{\sqrt{2\pi}}\int_{-\infty}^{\infty}\mathrm{d}\vec{p}\,D_{\pm,0}^0(\vec{p})e^{-i\vec{r}\cdot\vec{p}} \tag{6.29}$$

Putting this back into Equation 6.28,

$$D_{\pm,l}(\vec{p},t) = \frac{1}{2\pi}\int_{-\infty}^{\infty}\mathrm{d}\vec{r}\int_{-\infty}^{\infty}\mathrm{d}\vec{p}'\,e^{ir(\vec{p}-\vec{p}')\pm i\alpha(\vec{r})t\pm il\theta_p}D_{\pm,0}^0(\vec{p}) \tag{6.30}$$

Defining the propagators

$$G_{\pm}(\vec{p}-\vec{p}',t) = \frac{1}{2\pi}\int_{-\infty}^{\infty}\mathrm{d}\vec{r}\,e^{i\vec{r}\cdot(\vec{p}-\vec{p}')\pm ia(\vec{r})t} \tag{6.31}$$

$$= \frac{1}{2\pi}\int_{-\infty}^{\infty}\mathrm{d}\vec{r}\,e^{i\vec{r}\cdot(\vec{p}-\vec{p}')\pm i\Omega\cos(\vec{r}\cdot\vec{k}+\theta_p)t} \tag{6.32}$$

Utilizing the Jacobi-Anger expansion yet again, this becomes

$$G_{\pm}(\vec{p}-\vec{p}',t) = \frac{1}{2\pi}\int_{-\infty}^{\infty}\mathrm{d}\vec{r}\,e^{i\vec{r}\cdot(\vec{p}-\vec{p}')}\sum_{m=-\infty}^{\infty}e^{im\vec{r}\cdot\vec{k}}e^{im\theta_p}I_m(\pm i\Omega t), \tag{6.33}$$

where I_m is the mth modified Bessel function of the first kind.

At this point, remember that the $G_{\pm}(\vec{p}',t)$ are the propagators that propagate the state coefficients $D_{\pm,0}^0(\vec{p})$ to another momentum $\vec{p}'$ and quantum number $l = \pm 1$ at time t. For a

diffraction grating, this should be a series of delta functions corresponding to the diffraction orders. The above equation becomes

$$G_{\pm}(\vec{p} - \vec{p}', t) = \frac{1}{2\pi} \sum_{m=-\infty}^{\infty} \delta(\vec{p}' - (\vec{p} - m\hbar k)) e^{-im\theta_p} I_m(\pm i\Omega t).$$ (6.34)

Plugging this into Equation 6.30, the final form of the state coefficients $D_{\pm}(p, t)$ is

$$D_{\pm,l}(\vec{p}, t) = \sum_{m=-\infty}^{\infty} (\pm i)^m J_m(\Omega t) D_{\pm,0}^0(\vec{p} - m\hbar\vec{k}) e^{i(l-m)\theta_p}$$ (6.35)

$$= \sum_{m=-\infty}^{\infty} (\pm i)^m J_m(\Omega t) D_{\pm,l-m}^0(\vec{p} - m\hbar\vec{k}).$$ (6.36)

6.8   Diffracted Beams

Taking a step back from the math, consider that this equation gives a relation for the (mixed) state coefficients after interaction time t $D_{\pm,l}(\vec{p}, t)$ to the state coefficients before the interaction $D_{\pm,l}(\vec{p}, t \leq 0)$. If the atom beam initially has atoms in the ground state with $\vec{p} = p_z$ (such that the optical axis is the z-axis), and $\vec{k}$ is some direction in the x-y plane defined by the counterpropagating laser modes, and if the atom is initially in an $l = 0$ state, the state coefficients are

$$C_{+,l}(\vec{p}) = 0$$ (6.37)

$$C_{-,l}(\vec{p}) = (\delta(\vec{p}) \delta_{l,0})^{\frac{1}{2}}$$ (6.38)

gives that $D_{\pm,l}^0(\vec{p}) = \pm \left(\frac{1}{2} \delta(\vec{p}) \delta_{l,0} \right)^{\frac{1}{2}}$. Note that the delta functions are under a square-root so that the probability (which is related to the square of the coefficient) is properly normalized. The momentum probability density $W(\vec{p})$ is now formed by summing over all other quantum

83

numbers as

$$W(\vec{p}) = \sum_l \left(|C_{+,l}(\vec{p})|^2 + |C_{-,l}(\vec{p})|^2 \right) \tag{6.39}$$

$$= \sum_l \left(|D_{+,l}(\vec{p})|^2 + |D_{-,l}(\vec{p})|^2 \right) \tag{6.40}$$

$$= \sum_l \sum_m J_m^2(\Omega t)\delta(\vec{p} - m\hbar\vec{k})\delta_{l,m} \tag{6.41}$$

$$= \sum_m J_m^2(\Omega t)\delta(\vec{p} - m\hbar\vec{k}) \tag{6.42}$$

Note that from Equation 6.36 to Equation 6.41 should involve a double sum over separate indices, but I have neglected this because the delta functions work it out. Note that Equation 6.42 gives that the probability $P_m(t)$ that the beam has had the optical axis shifted by $m\hbar\vec{k}$ is

$$P_m(t) = J_m^2(\Omega t). \tag{6.43}$$

Note that any beam mode will require a certain frequency range to represent it (the width in frequencies in the plane-wave basis), and this spread is related to the dispersion of the beam as it propagates. As long as the diffraction angle is large compared with the dispersion of the beam mode, the diffraction orders will be well separated. The diffraction angle for the first diffraction order is, under the small angle approximation, $\varphi_1 \approx \hbar k/p_z$, where p_z is the initial z-momentum of the atom beam, and $\hbar k$ is the momentum transfer to the first diffracted order, with $\vec{k}$ in the x-y plane.

6.9   Numerics

The approximations introduced in Section 6.6 are $(\hbar p_\perp \cdot \vec{k}/M + \hbar\omega^2/(2Mc^2))t \ll 1$, which is that the Doppler shift and the recoil shift are small. The recoil shift is half the Doppler shift when $p_\perp = \hbar\vec{k}$, corresponding to the first diffraction order. Thus the constraint

becomes

$$t < \frac{2Mc^2}{3\hbar\omega^2} \tag{6.44}$$

This constraint puts a limit on the interaction region from $-L \leq z \leq L$, and the interaction time is related to the intensity of the diffraction orders. Consider a generic atom with mass $M = 1.6 \times 10^{-22}$g and $\omega = 3 \times 10^{15}$s^{-1}, giving $\hbar k = 4.17 \times 10^{-23}kg\frac{m}{s}$, and for a beam with initial z velocity $v_z = 10\frac{m}{s}$, $p_z = 1.6 \times 10^{-21}kg\frac{m}{s}$, giving a diffraction angle of $\varphi_1 = 2.6$ milliradians for the first diffraction order. Due to the tiny wavelength of the atoms ($2.t \times 10^{-13}$m in this case), the atom beam is essentially non-divergent when it is on the order of millimeters. Thus, if the beam is 2mm in diameter initially, and remains 2mm in diameter after propagating beyond the grating by 1 meter, the diffraction orders will be 2.6mm separated. This seems completely reasonable.

Lastly, I wish to determine the conditions for which the laser maximized the diffraction efficiency. To this end, the intensity in the first diffracted order is

$$P_m(t) = J_m^2(\Omega t), \tag{6.45}$$

where $\Omega = \langle -| \vec{\mu} \cdot \vec{E}_0 |+ \rangle / \hbar = (8\pi I/(c\varepsilon_0 \hbar^2))^{\frac{1}{2}} \langle -| \vec{\mu} \cdot \varepsilon |+ \rangle$, where I is the intensity of the laser beam. The Bessel function is maximized for $\Omega t \approx 1.84$, with $J_1^2(1.84) \approx 0.34$. Choosing the interaction region to be 20 microns thick, so that $L = 2 \times 10^{-3}$cm, $\Omega \approx 917.5 kHz$ for an intensity of $22\frac{\mu W}{cm^2}$, which, combined with the time of flight of 2 microseconds, gives $\Omega t \approx 1.84$ and maximizes the first diffraction order. The time constraint above is that the interaction time should be less than 160 microseconds, which is met.

6.10 Discussions

At this point it becomes clear that the intensity required in the laser beam is quite small, and it would behoove me to check that the rate Ω still has the condition $\Omega \gg \gamma$, such that the spontaneous decay rate can be ignored. To get around this issue, the interaction

region can be made smaller and a different peak of the $J_1^2(\Omega t)$ function can be sought, which can increase the rate Ω.

Concerning the simplifications of this model – Bessel beams do not exist, just as plane waves to not exist, and recreating a lowering or raising operator as an interference region of two lasers is not fully possible. At best, the raising and lowering operators will raise or lower the desired quantum number while also leaving the system in an infinite superposition of the other quantum number. The basic result would be the same though and following through with the analysis would be only useful in the engineering aspect of how to set up the laser beams optimally.

To summarize the chapter – resonant standing wave EM gratings can be utilized to imprint complex beam profiles onto a propagating atom beam under the appropriate assumptions, the most limiting of which are that the atom beam is well approximated by a two level system where the spontaneous decay from the excited state can be ignored during interaction with the laser beams.

CHAPTER VII

CONCLUSION

We demonstrate the viability of electron diffraction gratings to produce high quality shaped electron beams. Electron diffraction gratings have the possibility to create almost arbitrary beams that can be quite bright relative to the incident beam. These beams have a wide range of possible uses, and we provide some preliminary work on exploring some of these use cases.

APPENDIX A

CODE FOR ARBITRARY GRATING CORRECTION

This appendix lists the Python code for generating maps $s \in E_p$ for diffraction order p, see Equation 3.21.

Brute Force Search

The first step is to generate a brute force search over a small domain of $1 \leq n \leq 7$, and $-5 \leq s(n) \leq 5$. First I define a class called `memory` that allows the most recent return value of a function to be recalled without running the function again.

```
1   class memory(list):
2       def __init__(self, func):
3           super(memory, self).__init__()
4           self.func = func
5           self.append(None)
6
7       def __call__(self, *args, **kwargs):
8           self[0] = self.func(*args, **kwargs)
9           return self[0]
```

Next I need a function that will give the magnitude of the component. This depends on h, Z, $\widetilde{V}$, and c – the maximum depth, the location on the envelope function, the material parameters, and the Fourier coefficients. I also need a function that gives the diffraction order the component adds to

```
10  @memory
11  def val(sequence, Z, V, c):
12      return numpy.abs(
13          numpy.prod([numpy.sum(component(h * Z, pair[0], pair[1], c, V))
14              for pair in sequence]))
15
16  @memory
17  def order(sequence):
18      return sum([pair[0] * pair[1] for pair in sequence])
```

Here `component` gives the contribution of an individual component within the infinite product that defines each term. Also, `sequence` is a list of lists defining the map, of the form

sequence = [[1, -1], [2, 1], [3, 0], [4, 0], [5, 0]]

With this, the code to generate all sequences of a certain range, say for $1 \leq n \leq 7$ and $-5 \leq s(n) \leq 5$ is

```
19  import itertools
20  max_length_of_sequence = 100
21  nMax = 7
22  mMax = 5
23  tail = [[i, 0] for i in range(nMax + 1, max_length_of_sequence + 1)]
24  brute_search = (list(l) + tail for l in itertools.product(
25      *[[[n, m] for m in range(-mMax, mMax + 1)] for n in range(1, nMax + 1)]))
```

Next to create a `dict` that contains only the terms from `brute_search` that contribute to the first diffraction order,

```
26  matches = {i: {'list': list(sequence),
27                 'order': order[0],
28                 'val': val[0]}
29                 for i, sequence in enumerate(brute_search)
30                 if order(sequence) == 1 and
31                 val(list(sequence), h, Z, V, Fourier_coefficients) > 0}
```

And finally, to sort the results into the largest 5000 (or however many are necessary). This will produce a `dict` containing the 5000 most significant terms listed in order of significance that were in the parameter spaced searched via `brute_search`.

```
32  import heapq
33  matches_sorted = {i: res[1] for i, res in enumerate(heapq.nlargest(
34                       5000, matches.items(), key=lambda item: item[1]['val']))}
```

Pattern Search

The brute force search can only search for relatively small n values. Here I describe a method to extend the search to a much larger range. First I define a function that allows me to stitch together certain sequences.

```
35  def extend(a, b, level):
36      if level > 1:
37          try:
38              a.extend(b[0])
39          except:
40              a.append(b)
41      else:
42          a.append(b)
43      return a
```

89

Next, I define the `Search` function that will be used to generate patterns

```
44  def Search(N, val, level, start_level, minimum, r):
45      n = N
46      forward = False
47      sig = N
48      s = 1
49      if level == 1:
50          if not abs(r) == 0:
51              s = abs(r)
52          while n > 0:
53              for i in range(-s, s + 1):
54                  if i == 0:
55                      continue
56                  if val + i * n == 1:
57                      forward = True
58                      yield [[n, i], ['end']]
59              n -= 1
60      else:
61          while n > 0:
62              if level == start_level:
63                  if n < minimum:
64                      break
65              sig = 0.5 * (1 + (level)) * (2 * (n - 1) - (level)) + 2
66              if sig < abs(val - 2 * n) <= 2 * sig:
67                  forward = True
68                  yield extend([[n, -2]],
69          Search(n - 1, val - 2 * n, level - 1, start_level, minimum, r), level - 1)
70              if abs(val - n) <= sig:
71                  forward = True
72                  yield extend([[n, -1]],
73          Search(n - 1, val - n, level - 1, start_level, minimum, r), level - 1)
74              if abs(val + n) <= sig:
75                  forward = True
76                  yield extend([[n,  1]],
77          Search(n - 1, val + n, level - 1, start_level, minimum, r), level - 1)
78              if sig < abs(val + 2 * n) <= 2 * sig:
79                  forward = True
80                  yield extend([[n,  2]],
81          Search(n - 1, val + 2 * n, level - 1, start_level, minimum, r), level - 1)
82              n -= 1
83
84      if forward is False:
85          yield [[n,  sign(val), level, val + sign(val) * n, n, sig, 'ended', r]]
```

Finally, two more function to make this useful

```
86  def retreive(t, cur, tree):
87      try:
88          for item in list(tree):
89              val = copy.copy(cur)
90              if len(item) > 1 and str(item[1].__class__) == "<class 'generator'>":
91                  val.append(item[0])
92                  retreive(t, val, list(item[1]))
93              else:
94                  val.append(item[0])
95                  t.append(val)
96      except:
97          pass
98
99  def search(N, level, extend, begin, r=0):
```

```python
100            """
101            This is used to find contributors with 'level' entries non zero.
102            The search ensures the maximum has n value of at least 'begin',
103            and will search to a maximum n value of 'N'.
104            The returned sequences are extended to 'extend'
105            """
106            if extend < N:
107                raise AttributeError("'extend' must be greater than 'N'")
108            b = list(Search(N, 0, level, level, begin, r))
109            t = []
110            retreive(t, [], b)
111
112            tmp = [item for item in t if len(item) == level and
113                   order(item) == 1 and len(item[-1]) == 2]
114            ret = []
115            for item in tmp:
116                ar = numpy.array(item)
117                temp = [[i, item[list(ar[:,0]).index(i)][1] if i in ar[:,0] else 0]
118                        for i in range(1, extend + 1)]
119                ret.append(temp)
120            return ret
```

With this, I can generate maps that contribute to the first diffraction order that contain specified number of terms. For maps with two terms which will not be found via the brute-force method, I have

```python
121  b = search(100, 2, 100, 7, 9)
122  b = b[::-1]
123  num = 15
124  form = "{0}|" + "".join(("{"+str(n)+ "}" for n in range(1,15+1)))
125  print(form.format("n".rjust(3), *[str(i + 1).rjust(3) for i in range(num)], ""))
126  print("   |" + "-" * 3 * num)
127  for i in range(30):
128      print(form.format(str(i + 1).rjust(3), *[str(m).rjust(3) for n, m in b[i][0:num]]))
```

Producing the following output

```
  n|   1   2   3   4   5   6   7   8   9  10  11  12  13  14  15
   |------------------------------------------------------------
  1|  -6   0   0   0   0   0   1   0   0   0   0   0   0   0   0
  2|   0  -3   0   0   0   0   1   0   0   0   0   0   0   0   0
  3|   0   0  -2   0   0   0   1   0   0   0   0   0   0   0   0
  4|   0   0   0   0   0  -1   1   0   0   0   0   0   0   0   0
  5|   8   0   0   0   0   0  -1   0   0   0   0   0   0   0   0
  6|   0   4   0   0   0   0  -1   0   0   0   0   0   0   0   0
  7|   0   0   0   2   0   0  -1   0   0   0   0   0   0   0   0
  8|  -7   0   0   0   0   0   0   1   0   0   0   0   0   0   0
  9|   0   0   0   0   0   0  -1   1   0   0   0   0   0   0   0
 10|   9   0   0   0   0   0   0  -1   0   0   0   0   0   0   0
 11|   0   0   3   0   0   0   0  -1   0   0   0   0   0   0   0
 12|  -8   0   0   0   0   0   0   0   1   0   0   0   0   0   0
 13|   0  -4   0   0   0   0   0   0   1   0   0   0   0   0   0
 14|   0   0   0  -2   0   0   0   0   1   0   0   0   0   0   0
```

```
15|   0   0   0   0   0   0   0  -1   1   0   0   0   0   0   0
16|   0   5   0   0   0   0   0   0  -1   0   0   0   0   0   0
17|   0   0   0   0   2   0   0   0  -1   0   0   0   0   0   0
18|  -9   0   0   0   0   0   0   0   0   1   0   0   0   0   0
19|   0   0  -3   0   0   0   0   0   0   1   0   0   0   0   0
20|   0   0   0   0   0   0   0   0  -1   1   0   0   0   0   0
21|   0  -5   0   0   0   0   0   0   0   0   1   0   0   0   0
22|   0   0   0   0  -2   0   0   0   0   0   1   0   0   0   0
23|   0   0   0   0   0   0   0   0   0  -1   1   0   0   0   0
24|   0   6   0   0   0   0   0   0   0   0  -1   0   0   0   0
25|   0   0   4   0   0   0   0   0   0   0  -1   0   0   0   0
26|   0   0   0   3   0   0   0   0   0   0  -1   0   0   0   0
27|   0   0   0   0   0   2   0   0   0   0  -1   0   0   0   0
28|   0   0   0   0   0   0   0   0   0   0  -1   1   0   0   0
29|   0  -6   0   0   0   0   0   0   0   0   0   0   1   0   0
30|   0   0  -4   0   0   0   0   0   0   0   0   0   1   0   0
```

APPENDIX B

CODE FOR PERCEPTUALLY UNIFORM COLOR MAP

This code will generate red, green, and blue (rgb) values that correspond to perceptually uniform color map from a complex valued array to a color image. That is, for complex numbers of equal magnitude, the corresponding rgb values will have a perceptually uniform intensity despite having different colors. In the code below, `data` is a 2-dimensional complex valued `numpy` which we wish to represent as an image. We assume that `data` is normalized.

```python
def cielab_image(data):
    import numpy
    split_view = numpy.dtype((numpy.uint32, {'b': (numpy.uint8, 0),
                                             'g': (numpy.uint8, 1),
                                             'r': (numpy.uint8, 2),
                                             'a': (numpy.uint8, 3)}))
    rgb_image = numpy.zeros_like(data, dtype=numpy.uint32)
    rgb_image_components = rgb_image.view(split_view)

    rgb_image_components['a'] = numpy.full(data.shape, fill_value=255, dtype=numpy.uint8)

    value = numpy.absolute(data) * 255
    hue = (numpy.angle(data) + numpy.pi) / 2
    pi6 = numpy.pi / 6

    def sin2(array, offset):
        return numpy.sin(array - offset) ** 2

    g = 0.6 * sin2(hue, 2 * pi6)
    r = sin2(hue, 0.15 * pi6)
    r += 0.35 * sin2(hue, 3.15 * pi6)
    g += 0.065 * sin2(hue, 5.05 * pi6)
    b = sin2(hue, 4.25 * pi6)

    g += 0.445 * b
    g += 0.33 * r

    rgb_image_components['r'] = (r * vlaue).astype(numpy.uint8)
    rgb_image_components['g'] = (g * vlaue).astype(numpy.uint8)
    rgb_image_components['b'] = (b * vlaue).astype(numpy.uint8)

    return rgb_image
```

REFERENCES CITED

[1] L. Allen, M. W. Beijersbergen, R. J. C. Spreeuw, and J. P. Woerdman. Orbital angular momentum of light and the transformation of Laguerre-Gaussian laser modes. *Physical Review A*, 45(11):8185, June 1992.

[2] Jian Wang, Jeng-Yuan Yang, Irfan M. Fazal, Nisar Ahmed, Yan Yan, Hao Huang, Yongxiong Ren, Yang Yue, Samuel Dolinar, Moshe Tur, and Alan E. Willner. Terabit free-space data transmission employing orbital angular momentum multiplexing. *Nature Photonics*, 6(7):488–496, July 2012. 00475.

[3] Nenad Bozinovic, Yang Yue, Yongxiong Ren, Moshe Tur, Poul Kristensen, Hao Huang, Alan E. Willner, and Siddharth Ramachandran. Terabit-Scale Orbital Angular Momentum Mode Division Multiplexing in Fibers. *Science*, 340(6140):1545–1548, June 2013. 00305.

[4] Gregory Foo, David M. Palacios, and Jr. Swartzlander. Optical vortex coronagraph. *Optics Letters*, 30(24):3308, December 2005.

[5] H. He, M. E. J. Friese, N. R. Heckenberg, and H. Rubinsztein-Dunlop. Direct Observation of Transfer of Angular Momentum to Absorptive Particles from a Laser Beam with a Phase Singularity. *Physical Review Letters*, 75(5):826, July 1995. 00958.

[6] K. T. Gahagan and Jr. Swartzlander. Optical vortex trapping of particles. *Optics Letters*, 21(11):827–829, June 1996. 00545.

[7] Masaya Uchida and Akira Tonomura. Generation of electron beams carrying orbital angular momentum. *Nature*, 464(7289):737, April 2010. 00172 Cited by 0096.

[8] J. Verbeeck, H. Tian, and P. Schattschneider. Production and application of electron vortex beams. *Nature*, 467(7313):301, 2010. 00221 Cited by 0114.

[9] Benjamin McMorran, Amit Agrawal, Henri J. Lezec, Jabez J. McClelland, and John Unguris. Electron Beams with Orbital Angular Momentum and Their Application to Magnetic Imaging. Scottsdale, AZ, November 2011. 00000.

[10] A. Béché, R. Winkler, H. Plank, F. Hofer, and J. Verbeeck. Focused electron beam induced deposition as a tool to create electron vortices. *Micron*, 80:34–38, January 2016. 00002.

[11] A. M. Blackburn and J. C. Loudon. Vortex beam production and contrast enhancement from a magnetic spiral phase plate. *Ultramicroscopy*, 136:127–143, January 2014. 00013.

[12] Armand Béché, Ruben Van Boxem, Gustaaf Van Tendeloo, and Jo Verbeeck. Magnetic monopole field exposed by electrons. *Nature Physics*, 10(1):26–29, January 2014. 00034.

[13] Arthur M. Blackburn. Observation of an Electron Vortex Beam Created from a Self-Charging Rod. *Microscopy and Microanalysis*, 22(S3):1710–1711, July 2016. 00000.

[14] Giulio Pozzi, Peng-Han Lu, Amir H. Tavabi, Martial Duchamp, and Rafal E. Dunin-Borkowski. Generation of electron vortex beams using line charges via the electrostatic Aharonov-Bohm effect. *Ultramicroscopy*, 181:191–196, October 2017.

[15] T. C. Petersen, M. Weyland, D. M. Paganin, T. P. Simula, S. A. Eastwood, and M. J. Morgan. Electron Vortex Production and Control Using Aberration Induced Diffraction Catastrophes. *Physical Review Letters*, 110(3):033901, January 2013.

[16] Jo Verbeeck, Giulio Guzzinati, Laura Clark, Roeland Juchtmans, Ruben Van Boxem, He Tian, Armand Béché, Axel Lubk, and Gustaaf Van Tendeloo. Shaping electron beams for the generation of innovative measurements in the (S)TEM. *Comptes Rendus Physique*, 15(2–3):190–199, February 2014.

[17] Noa Voloch-Bloch, Yossi Lereah, Yigal Lilach, Avraham Gover, and Ady Arie. Generation of electron Airy beams. *Nature*, 494(7437):331–335, February 2013. 00053.

[18] Vincenzo Grillo, Gian Carlo Gazzadi, Ebrahim Karimi, Erfan Mafakheri, Robert W. Boyd, and Stefano Frabboni. Highly efficient electron vortex beams generated by nanofabricated phase holograms. *Applied Physics Letters*, 104(4):043109, January 2014.

[19] Tyler R. Harvey, Jordan S. Pierce, Amit K. Agrawal, Peter Ercius, Martin Linck, and Benjamin J. McMorran. Efficient diffractive phase optics for electrons. *New Journal of Physics*, 16(9):093039, September 2014. 00010.

[20] Tyler R. Harvey, Jordan S. Pierce, Jordan J. Chess, and Benjamin J. McMorran. Demonstration of electron helical dichroism as a local probe of chirality. *arXiv:1507.01810*, July 2015. 00001 arXiv: 1507.01810.

[21] incenzo Grillo, Amir H. Tavabi, Federico Venturi, Hugo Larocque, Roberto Balboni, Gian Carlo Gazzadi, Stefano Frabboni, Peng-Han Lu, Erfan Mafakheri, Frédéric Bouchard, Rafal E. Dunin-Borkowski, Robert W. Boyd, Martin P. J. Lavery, Miles J. Padgett, and Ebrahim Karimi. Measuring an electron beam's orbital angular momentum spectrum. *arXiv:1609.09129 [physics, physics:quant-ph]*, September 2016. 00000 arXiv: 1609.09129.

[22] Martin Linck, Peter A. Ercius, Jordan S. Pierce, and Benjamin J. McMorran. Aberration corrected STEM by means of diffraction gratings. *Ultramicroscopy*, 182:36–43, November 2017. 00001.

[23] Juan C. Idrobo and Stephen J. Pennycook. Vortex beams for atomic resolution dichroism. *Journal of Electron Microscopy*, 60(5):295 –300, October 2011. 00016 Cited by 0004.

[24] Jo Verbeeck, He Tian, and Gustaaf Van Tendeloo. How to Manipulate Nanoparticles with an Electron Beam? *Advanced Materials*, 25(8):1114–1117, 2013.

[25] Ján Rusz and Somnath Bhowmick. Boundaries for Efficient Use of Electron Vortex Beams to Measure Magnetic Properties. *Physical Review Letters*, 111(10):105504, September 2013.

[26] A. Asenjo-Garcia and F. J. García de Abajo. Dichroism in the Interaction between Vortex Electron Beams, Plasmons, and Molecules. *Physical Review Letters*, 113(6):066102, August 2014. 00000.

[27] Colin Ophus, Jim Ciston, Jordan Pierce, Tyler R. Harvey, Jordan Chess, Benjamin J. McMorran, Cory Czarnik, Harald H. Rose, and Peter Ercius. Efficient linear phase contrast in scanning transmission electron microscopy with matched illumination and detector interferometry. *Nature Communications*, 7:10719, February 2016. 00014.

[28] Nobuo Tanaka. Present status and future prospects of spherical aberration corrected TEM/STEM for study of nanomaterials. *Science and Technology of Advanced Materials*, 9(1):014111, January 2008.

[29] S. J. Pennycook, M. F. Chisholm, A. R. Lupini, M. Varela, A. Y. Borisevich, M. P. Oxley, W. D. Luo, K. van Benthem, S.-H. Oh, D. L. Sales, S. I. Molina, J. García-Barriocanal, C. Leon, J. Santamaría, S. N. Rashkeev, and S. T. Pantelides. Aberration-corrected scanning transmission electron microscopy: from atomic imaging and analysis to solving energy problems. *Philosophical Transactions of the Royal Society A: Mathematical, Physical and Engineering Sciences*, 367(1903):3709–3733, September 2009. 00040.

[30] O.L. Krivanek, N. Dellby, and A.R. Lupini. Towards sub-Å electron beams. *Ultramicroscopy*, 78(1–4):1–11, June 1999.

[31] Heiko Müller, Stephan Uhlemann, Peter Hartel, and Maximilian Haider. Advancing the Hexapole Cs-Corrector for the Scanning Transmission Electron Microscope. *Microscopy and Microanalysis*, 12(06):442–455, 2006. 00078.

[32] Benjamin J. McMorran and Tyler R. Harvey. United States Patent: 9960008 - Methods and devices for measuring orbital angular momentum states of electrons, May 2018.

[33] Benjamin McMorran. United States Patent: 8,680,488 - System and method for producing and using multiple electron beams with quantized orbital angular momentum in an electron microscope, March 2014. 00000.

[34] Benjamin J. McMorran, Amit Agrawal, Ian M. Anderson, Andrew A. Herzing, Henri J. Lezec, Jabez J. McClelland, and John Unguris. Electron Vortex Beams with High Quanta of Orbital Angular Momentum. *Science*, 331(6014):192 –195, January 2011.

[35] Robert Collier. *Optical Holography.* Elsevier, June 2013.

[36] Arthur M. Blackburn. Phase plate, August 2013. 00021 U.S. Classification 250/311, 250/396.0ML, 977/832, 250/396.00R; International Classification G21K5/02, H01J37/26, G21K1/08; Cooperative Classification H01J2237/1523, H01J2237/2614, H01J37/147, G21K5/02, G21K1/08, H01J37/26, B82B1/008.

[37] P. Schattschneider, S. Rubino, C. Hébert, J. Rusz, J. Kuneš, P. Novák, E. Carlino, M. Fabrizioli, G. Panaccione, and G. Rossi. Detection of magnetic circular dichroism using a transmission electron microscope. *Nature*, 441(7092):486–488, May 2006. 00174.

[38] Fehmi S. Yasin, Tyler R. Harvey, Jordan J. Chess, Jordan S. Pierce, and Benjamin J. McMorran. Path-separated electron interferometry in a scanning transmission electron microscope. *Journal of Physics D: Applied Physics*, 51(20):205104, 2018.

[39] Koh Saitoh, Yuya Hasegawa, Nobuo Tanaka, and Masaya Uchida. Production of electron vortex beams carrying large orbital angular momentum using spiral zone plates. *Journal of Electron Microscopy*, 61(3):171–177, June 2012.

[40] J. Verbeeck, H. Tian, and A. Béché. A new way of producing electron vortex probes for STEM. *Ultramicroscopy*, 113(0):83–87, February 2012.

[41] J.S. Pierce, T.R. Harvey, T.S. Yahn, and B.J. McMorran. High Efficiency Electron Diffractive Optics. *Microscopy and Microanalysis*, 19(Supplement S2):1188–1189, 2013.

[42] Tyler R. Harvey, Gii Brougher, Kurt Langworthy, and Benjamin J. McMorran. Small-Pitch Electron Diffraction Holograms Patterned on Inorganic Resist with Electron Beam Lithography. In *EIPBN Proceedings*, Nashville, TN, May 2013. 00000.

[43] Edgar Völkl, Lawrence F. Allard, and David C. Joy. *Introduction to Electron Holography.* Springer, January 1999.

[44] H. Kohl and H. Rose. Theory of Image Formation by Inelastically Scattered Electrons in the Electron Microscope. In Peter W. Hawkes, editor, *Advances in Electronics and Electron Physics*, volume 65, pages 173–227. Academic Press, January 1985.

[45] Virendra N. Mahajan. Uniform versus Gaussian beams: a comparison of the effects of diffraction, obscuration, and aberrations. *Journal of the Optical Society of America A*, 3(4):470–485, April 1986.

[46] Roy Shiloh, Yossi Lereah, Yigal Lilach, and Ady Arie. Sculpturing the electron wave function using nanoscale phase masks. *Ultramicroscopy*, 144:26–31, September 2014.

[47] Vincenzo Grillo, Ebrahim Karimi, Roberto Balboni, Gian Carlo Gazzadi, Federico Venturi, Stefano Frabboni, Jordan S Pierce, Benjamin J McMorran, and Robert W Boyd. Electron holograms encoding amplitude and phase for the generation of arbitrary wavefunctions. *Microscopy and Microanalysis*, 21(Supplement S3):503–504, August 2015. 00001.

[48] Vincenzo Grillo, Gian Carlo Gazzadi, Erfan Mafakheri, Stefano Frabboni, Ebrahim Karimi, and Robert W. Boyd. Holographic Generation of Highly Twisted Electron Beams. *Physical Review Letters*, 114(3):034801, January 2015. 00023.

[49] Koh Saitoh, Yuya Hasegawa, Kazuma Hirakawa, Nobuo Tanaka, and Masaya Uchida. Measuring the Orbital Angular Momentum of Electron Vortex Beams Using a Forked Grating. *Physical Review Letters*, 111(7):074801, August 2013.

[50] Konstantin Y. Bliokh, Mark R. Dennis, and Franco Nori. Relativistic Electron Vortex Beams: Angular Momentum and Spin-Orbit Interaction. *Physical Review Letters*, 107(17):174802, October 2011. 00061 Cited by 0032.

[51] Vincenzo Grillo, Ebrahim Karimi, Gian Carlo Gazzadi, Stefano Frabboni, Mark R. Dennis, and Robert W. Boyd. Generation of Nondiffracting Electron Bessel Beams. *Physical Review X*, 4(1):011013, January 2014.

[52] Ronald L. Phillips and Larry C. Andrews. Spot size and divergence for Laguerre Gaussian beams of any order. *Applied Optics*, 22(5):643–644, March 1983.

[53] J. Verbeeck, P. Schattschneider, S. Lazar, M. Stöger-Pollach, S. Löffler, A. Steiger-Thirsfeld, and G. Van Tendeloo. Atomic scale electron vortices for nanoresearch. *Applied Physics Letters*, 99(20):203109, November 2011. 00047.

[54] Anderson M. Amaral, Edilson L. Falcão-Filho, and Cid B. de Araújo. Distinguishing orbital angular momenta and topological charge in optical vortex beams. *arXiv:1402.3226 [physics]*, February 2014.

[55] Chen-Ta Ku, Heh-Nan Lin, and Chen-Bin Huang. Direct observation of surface plasmon vortex and subwavelength focusing with arbitrarily-tailored intensity patterns. *Applied Physics Letters*, 106(5):053112, February 2015. 00001.

[56] R. Vinu and Rakesh Kumar Singh. Determining helicity and topological structure of coherent vortex beam from laser speckle. 109.

[57] Donald I. A. MacLeod and Robert M. Boynton. Chromaticity diagram showing cone excitation by stimuli of equal luminance. *JOSA*, 69(8):1183–1186, August 1979.

[58] C. Connolly and T. Fleiss. A study of efficiency and accuracy in the transformation from RGB to CIELAB color space. *IEEE Transactions on Image Processing*, 6(7):1046–1048, July 1997.

[59] Mohammad Mirhosseini, Omar S. Magaña-Loaiza, Changchen Chen, Brandon Rodenburg, Mehul Malik, and Robert W. Boyd. Rapid generation of light beams carrying orbital angular momentum. *Optics Express*, 21(25):30196–30203, December 2013.

[60] Martin Linck, Benjamin McMorran, Jordan Pierce, and Peter Ercius. Aberration-Corrected STEM by Means of Diffraction Gratings. *Microscopy and Microanalysis*, 20(S3):946–947, August 2014. 00000.

[61] P. W. Hawkes. Aberration Correction Past and Present. *Philosophical Transactions: Mathematical, Physical and Engineering Sciences*, 367(1903):3637–3664, 2009.

[62] Ondrej Krivanek, Nicolas Delby, A. Spence, R. Camps, and L. Brown. Aberration correction in the STEM. *Journal of Physics: Conference Series*, 153, 1997.

[63] Maximilian Haider, Stephan Uhlemann, Eugen Schwan, Harald Rose, Bernd Kabius, and Knut Urban. Electron microscopy image enhanced. *Nature*, 392(6678):768–769, April 1998.

[64] N. Dellby, L. Krivanek, D. Nellist, E. Batson, and R. Lupini. Progress in aberration-corrected scanning transmission electron microscopy. *Journal of Electron Microscopy*, 50(3):177–185, May 2001.

[65] J. F. Nye and M. V. Berry. Dislocations in wave trains. *Proceedings of the Royal Society of London. A. Mathematical and Physical Sciences*, 336(1605):165–190, 1974. 01495 Cited by 1293.

[66] V. Yu. Bazhenov, M. V. Vasnetsov, and M. S. Soskin. Laser beams with screw dislocations in their wavefronts. *Jounal of Experimental and Theoretical Physics Letters*, 52(8):429, October 1990. 00361.

[67] Grover A. Swartzlander Swartzlander. The optical vortex coronagraph. *Journal of Optics A: Pure and Applied Optics*, 11(9):094022, 2009.

[68] Robert M. Glaeser. Limitations to significant information in biological electron microscopy as a result of radiation damage. *Journal of Ultrastructure Research*, 36(3):466–482, August 1971.

[69] M. Isaacson, D. Johnson, and A. V. Crewe. Electron Beam Excitation and Damage of Biological Molecules; Its Implications for Specimen Damage in Electron Microscopy. *Radiation Research*, 55(2):205–224, 1973.

[70] Stephen Pennycook and Peter Nellist. *Scanning Transmission Electron Microscopy: Imaging and Analysis.* Springer Science & Business Media, 2011.

[71] N Dekkers and H de Lang. Differential Phase Contrast in a STEM. *Optik*, 41(4):452–456, 1974.

[72] Christian Schulze, Filippus S. Roux, Angela Dudley, Ronald Rop, Michael Duparré, and Andrew Forbes. Accelerated rotation with orbital angular momentum modes. *Physical Review A*, 91(4):043821, April 2015.